

Time- and Temperature-Dependence of Fracture Energies Attributed to Copper/Epoxy Bonds

Stephen W. Brown

A thesis submitted to the faculty of
Virginia Polytechnic Institute and State University
in partial fulfillment of the requirements for the degree of

Master of Science
in
Engineering Mechanics

Approved by:

David A. Dillard, Chairman

John G. Dillard

Scott W. Case

July 30, 2004
Blacksburg, Virginia

Keywords: Fracture Mechanics, Impact, Loop Peel Test, Falling Wedge Test

Time- and Temperature-Dependence of Fracture Energies Attributed to Copper/Epoxy Bonds

Stephen W. Brown

ABSTRACT

When bonds between copper and printed circuit board laminates are subjected to impulsive forces, the need arises to characterize fracture energies corresponding to related, high-speed failure events. Work (or energy) is required to create new surface area—with associated dissipation events—during fracture, and this energy (for a given material system) is dependent on the speed of crack propagation, the locus of failure, and the temperature of the bond when it is broken. Since the 90° peel test has been widely employed in quasi-static fracture testing of film adhesion for printed circuit board applications, this test was first used as a basis to which other test results could be compared. A test fixture was designed and built for quasi-static peel testing that accommodated peeling at different angles and temperatures. A similar test was then desirable for the direct comparison of dynamic fracture events to those quasi-static results. The “loop peel test” was thus developed to mimic the common 90° peel test and to quantify the time- and temperature-dependent fracture energies of peel specimens during low-velocity impact. This test has been successfully used to determine the apparent critical strain energy release rate of copper/epoxy bonds for low-velocity impact conditions (1-10 m/s), for a case of near-interfacial failure. The falling wedge test has also been adapted to estimate the apparent critical strain energy release rate at similar fracture conditions. Four types of printed circuit boards have been analyzed with the above impact test methods as well as with their corresponding quasi-static tests, and the fracture energies measured with the impact tests have been compared to those obtained using quasi-static tests. Fracture energies of the material systems considered were dependent on time (speed of fracture), temperature, and the amount of moisture migration, as determined via humidity conditioning parameters.

ACKNOWLEDGEMENTS

The Lord is gracious, and from Him flow mercy and love. He is the reason I persevere. I would like to thank my wife, Nikki, for her committed support; my family, for their earnest prayers; and my church, Blacksburg Christian Fellowship, for their passion. I would like to thank my academic advisor, Dr. David A. Dillard; my committee members: Drs. John G. Dillard and Scott Case; Dr. Subhotosh Khan at Dupont; Drs. Kai-tak Wan and Don Ohanehi at Virginia Tech; Sumitra Subrahmanyam and Josh Simon at Virginia Tech; Kim Crews, with Virginia's Center for Innovative Technology; the Center for Adhesive and Sealant Science at Virginia Tech; and the Department of Engineering Science and Mechanics at Virginia Tech.

TABLE OF CONTENTS

<u>Chapter 1.</u>	<u>Introduction</u>	1
1.1	<u>Background</u>	1
1.2	<u>Objectives</u>	3
1.3	<u>Organization of Thesis</u>	4
<u>Chapter 2.</u>	<u>Literature Review</u>	5
2.1	<u>Fracture Testing</u>	5
2.1.1	<u>Development of Fracture Mechanics</u>	5
2.1.2	<u>Test Methods</u>	11
2.1.2.1	<u>Double Cantilever Beam Tests</u>	11
2.1.2.2	<u>Peel Tests</u>	18
2.1.3	<u>Moisture</u>	22
<u>Chapter 3.</u>	<u>Characterizing the Dynamic Fracture Resistance of Copper Foil Bonded to Printed Circuit Boards</u>	23
3.1	<u>Abstract</u>	23
3.2	<u>Introduction</u>	23
3.3	<u>Experimental</u>	26
3.3.1	<u>Specimen Preparation</u>	26
3.3.2	<u>Method</u>	29
3.3.2.1	<u>Quasi-static Peel</u>	29
3.3.2.2	<u>Loop Peel</u>	30
3.4	<u>Results and Discussion</u>	31
3.4.1	<u>Quasi-Static Overview</u>	31
3.4.2	<u>Loop Peel Overview</u>	38
3.4.3	<u>Plastic Deformation</u>	44
3.4.4	<u>Vibrational Analyses</u>	45
3.5	<u>Conclusions</u>	49
<u>Chapter 4.</u>	<u>Use of a Falling Wedge Test to Determine the Fracture Energy of Printed Circuit Boards</u>	52
4.1	<u>Abstract</u>	52
4.2	<u>Introduction</u>	52
4.3	<u>Experimental</u>	53
4.3.1	<u>Specimen Preparation</u>	53
4.3.2	<u>Falling Wedge</u>	57
4.3.3	<u>Quasi-static DCB</u>	62
4.4	<u>Results and Discussion</u>	66
4.5	<u>Conclusions</u>	68
<u>Chapter 5.</u>	<u>Results and Conclusions</u>	70
5.1	<u>Evaluation</u>	73
<u>Chapter 6.</u>	<u>References</u>	75
<u>Appendix A.</u>	<u>Design of Test Fixtures</u>	78
A.1	<u>Quasi-Static Peel Fixture</u>	78
A.2	<u>Climbing Drum</u>	80
<u>Appendix B.</u>	<u>Preliminary Impact Tests</u>	82
B.1	<u>Asymmetric 90° Impact Peel Test</u>	82
B.2	<u>180° Impact Peel Test</u>	85
B.3	<u>Climbing Drum Test</u>	86

<u>Appendix C.</u>	<u>Mechanical Properties of Materials</u>	90
<u>Appendix D.</u>	<u>Mathematica Programs</u>	93
D.1	<u>Analysis of Loop Peel Tests Using Fast Fourier Transformations</u>	93
D.2	<u>DCB Data Processor</u>	117
D.3	<u>Program to Generate Master Curves from DMA Data</u>	125
<u>Appendix E.</u>	<u>Surface Characterization Studies</u>	142
E.1	<u>Report 1</u>	142
E.1.1	<u>Introduction</u>	142
E.1.2	<u>Preparation of Samples for Analysis</u>	144
E.1.3	<u>Presentation and Discussion of the Results</u>	145
E.1.4	<u>Summary</u>	153
E.2	<u>Report 2</u>	153
E.2.1	<u>Introduction</u>	153
E.2.2	<u>Experimental Approach</u>	154
E.2.3	<u>Results and Discussion</u>	155
E.2.3.1	<u>Fiberglass</u>	156
E.2.3.2	<u>Thermount</u>	156
E.2.4	<u>Summary</u>	167
E.3	<u>Report 3</u>	167
E.3.1	<u>Introduction</u>	167
E.3.2	<u>Experimental Approach</u>	168
E.3.3	<u>Results and Discussion</u>	168
E.4	<u>Quasi-Static Peel Test Results</u>	172
E.4.1	<u>Introduction</u>	172
E.4.2	<u>Results and Discussion</u>	173
E.4.2.1	<u>FR4 Samples</u>	173
E.4.2.2	<u>Thermount ST Samples</u>	174
E.4.2.3	<u>Thermount E Samples</u>	175
E.4.3	<u>Summary of XPS results for the analysis of Cu-FR4 composite failure surfaces: Peel testing at 90°C, 30°C, and -15°C</u>	177
E.4.4	<u>Summary of XPS results for the analysis of Cu-Thermount ST composite failure surfaces: Peel testing at 90°C, 30°C, and -15°C</u>	179
E.4.5	<u>Summary of XPS results for the analysis of Cu-Thermount E composite failure surfaces: Peel testing at 90°C, 30°C, and -15°C</u>	180
E.5	<u>Loop Peel Test Results</u>	182
E.5.1	<u>FR4 Samples</u>	183
E.5.2	<u>Thermount N and E Series Samples</u>	183
E.5.3	<u>Summary of XPS results for the analysis of Cu-FR4 composite failure surfaces: Loop testing at 125°C, 25°C, and -30°C.</u>	184
E.5.4	<u>Summary of XPS results for the analysis of Cu-Thermount N composite failure surfaces: Loop testing at 125°C, 25°C, and -85°C.</u>	185
E.5.5	<u>Summary of XPS results for the analysis of Cu-Thermount E composite failure surfaces: Loop testing at 125°C, 25°C, and -85°C.</u>	186
E.5.4	<u>Summary of XPS results for the analysis of Cu-Thermount N composite failure surfaces: Loop testing at 125°C, 25°C, and -85°C.</u>	185
	<u>Author's Vita</u>	187

LIST OF FIGURES

Figure 1:	Inverted 90° peel specimen	24
Figure 2:	Loop Peel Test Configuration	26
Figure 3:	Comparisons of Material Composition	28
Figure 4:	Sample Curing Profile for Epoxy Laminate	28
Figure 5:	Quasi-Static Peel Results	32
Figure 6:	Comparison of Quasi-Static Peel Test Variables via Interpolation	33
Figure 7:	Effect of Moisture on Quasi-Static Peel Energies	35
Figure 8:	Superposition of Non-Humidity Conditioned to Humidity Conditioned Quasi-Static Peel Test Results for Material E	36
Figure 9:	Superposition of Non-Humidity Conditioned to Humidity Conditioned Quasi-Static Peel Test Results for Material N	36
Figure 10:	Superposition of Non-Humidity Conditioned to Humidity Conditioned Quasi-Static Peel Test Results for Material S	37
Figure 11:	Superposition of Non-Humidity Conditioned to Humidity Conditioned Quasi-Static Peel Test Results for Material F	37
Figure 12:	Typical plot of force and displacement as a function of time for a loop peel test	39
Figure 13:	Relationships Used to Determine the SERR of Loop Peel Specimens	39
Figure 14:	Loop Peel Setup with Drop Tower and Oven	40
Figure 15:	Comparison of Peel Energies under Varying Rate of Test and Temperature for Material E	42
Figure 16:	Comparison of Peel Energies under Varying Rate of Test and Temperature for Material N	42
Figure 17:	Comparison of Peel Energies under Varying Rate of Test and Temperature for Material S	43
Figure 18:	Comparison of Peel Energies under Varying Rate of Test and Temperature for Material F	43
Figure 19:	Curvature of Copper Film at Root During 90° Peel Tests	44
Figure 20:	a) Deformed Cu from Quasi-Static Peel Test, b) Deformed Cu from Loop Peel Test	45
Figure 21:	a) Restrained Loop, b) Natural Response in Vibration	46
Figure 22:	a) FFT of Force vs. Time Signal of Figure 12, b) FFT Results for all Loop Peel Tests	48
Figure 23:	Sample Curing Profile for Epoxy Laminate	55
Figure 24:	DCB Specimen with Loading Hinges and Pins	57
Figure 25:	Falling Wedge Test Setup	58
Figure 26:	Falling Wedge Test Image and Digitized Beam Profile	60
Figure 27:	TTSP Master Curves for E-Series Samples w/ and w/o Cu	61
Figure 28:	Quasi-static DCB Setup	63
Figure 29:	Idealized DCB Load Trace and Reference Plot	63
Figure 30:	Typical Quasi-static DCB Data with Evident Plastic Deformation	65
Figure 31:	Estimation of Plastic Deformation in DCB Test	65
Figure 32:	Quasi-static DCB Data After Subtraction of Estimated Plasticity	66
Figure 33:	Falling Wedge and Quasi-static DCB Results	68
Figure 34:	Quasi-Static Peel Fixture	80
Figure 35:	Climbing Drum	81
Figure 36:	90° Impact Peel Setup	82
Figure 37:	Impact Loading Mechanism for 90° Peel Tests	83

Figure 38:	Typical Results of 90° Impact Peel Test	84
Figure 39:	180° Impact Peel Setup	86
Figure 40:	Climbing Drum Setup	87
Figure 41:	Variables of Climbing Drum Test	88
Figure 42:	Master curve of storage modulus versus frequency for Material #1	91
Figure 43:	Master curve of storage modulus versus frequency for Material #3	91
Figure 44:	Master curve of storage modulus versus frequency for Material #4	92
Figure 45:	N710 Polymer Region MeOH Cleaned – Wide Scan	146
Figure 46:	Arlon 2116 Polymer Region MeOH Cleaned – Wide Scan	146
Figure 47:	N710 Cu Region MeOH Cleaned – Wide Scan	147
Figure 48:	Arlon 2116 Cu Region MeOH Cleaned – Wide Scan	147
Figure 49:	N710 Polymer Region As Received – C 1s	149
Figure 50:	N710 Polymer Region MeOH Cleaned – C 1s	149
Figure 51:	Arlon 2116 Polymer Region MeOH Cleaned – C 1s	150
Figure 52:	N710 Cu Region MeOH Cleaned – C 1s	151
Figure 53:	Arlon 2116 Cu Region MeOH Cleaned – C 1s	152
Figure 54:	N710 Cu Region MeOH Cleaned – Cu 2p	152
Figure 55:	Arlon 2116 Cu Region MeOH Cleaned – Cu 2p	153
Figure 56:	Wide Scan of Metal-Side Failure Surface – Fiberglass-Copper	157
Figure 57:	Wide Scan of Polymer-Side Failure Surface – Fiberglass-Copper	158
Figure 58:	Wide Scan of Metal-Side Failure Surface – Thermount-Copper	158
Figure 59:	Wide Scan of Polymer-Side Failure Surface – Thermount-Copper	159
Figure 60:	C 1s Spectrum of Metal-Side Failure Surface – Fiberglass-Copper	159
Figure 61:	C 1s Spectrum of Polymer-Side Failure Surface – Fiberglass-Copper	160
Figure 62:	C 1s Spectrum of Metal-Side Failure Surface – Thermount-Copper	160
Figure 63:	C 1s Spectrum of Polymer-Side Failure Surface – Thermount-Copper	161
Figure 64:	SEM/EDX: Fiberglass-Metal-Side EDX:	163
Figure 65:	SEM/EDX: Fiberglass-Polymer-Side EDX:	164
Figure 66:	SEM/EDX: Thermont-Metal-Side EDX:	165
Figure 67:	SEM/EDX: Thermont-Polymer-Side EDX:	166
Figure 68:	Thermount Cu Region MeOH Cleaned (as received) – Cu 2p	170
Figure 69:	Thermount Cu Region 100RH & 70°C – Cu 2p	171
Figure 70:	Fiberglass Cu Region MeOH Cleaned (as received) – Cu 2p	171
Figure 71:	Fiberglass Cu Region 100RH & 70°C – Cu 2p	172

LIST OF TABLES

Table 1:	PCB Material Types	27
Table 2:	PCB Material Types	54
Table 3:	XPS Surface Analysis Characterization of Circuit Panels (Atomic %)	148
Table 4:	XPS Surface Analysis Characterization of Failure Surfaces (Atomic %)	157
Table 5:	XPS Surface Analysis Characterization of Specimens Surfaces: Following Exposure to 100% RH at 70°C 75 hrs: (first line); and for as received samples: (second line – from 1st quarterly report) results in atomic %	169
Table 6:	XPS results for samples tested at 90°C.	177
Table 7:	XPS results for samples tested at 30°C.	178
Table 8:	XPS results for samples tested at -15°C.	178
Table 9:	XPS results for samples tested at 90°C. Sample #1	179
Table 10:	XPS results for samples tested at 30°C. Sample #1	179
Table 11:	XPS results for samples tested at - 15°C. Sample #1	180
Table 12:	XPS results for samples tested at 90°C. Sample #1	180
Table 13:	XPS results for samples tested at 30°C. Sample #1	181
Table 14:	XPS results for samples tested at -15°C. Sample #1	181
Table 15:	XPS results for non-bonded Cu surface: sample tested at 90°C. Sample #1	182
Table 16:	XPS results for samples tested at 125°C, sample #3.	184
Table 17:	XPS results for samples tested at 25°C, sample no number.	184
Table 18:	XPS results for samples tested at -30°C, sample #4.	184
Table 19:	XPS results for samples tested at 125°C, Sample #4.	185
Table 20:	XPS results for samples tested at 25°C, Sample #1.	185
Table 21:	XPS results for samples tested at - 85°C, Sample #2.	185
Table 22:	XPS results for samples tested at 125°C, Sample #3.	186
Table 23:	XPS results for samples tested at 25°C, Sample #4.	186
Table 24:	XPS results for samples tested at -85°C, Sample #2.	186

Chapter 1. Introduction

1.1 Background

Electronic circuits may be compared to a human body—with transistors as organs and copper lines as arteries. Each part is necessary for the whole to operate successfully. Electronic circuits are usually not designed to continue working like the body, should an “artery,” that is a copper conduit, rupture. Rather, most electronic systems must be either repaired or (more likely) replaced upon such catastrophic failure.

The designer’s task is made more difficult as the sizes of electronics decrease while their expected service lives remain the same or even become longer. Where thick copper wires once served as conductors, thin copper “lines” do now. And the width and thickness of copper foil lines “printed” onto circuit boards today are constantly challenged by rising demands for the real estate on the circuit boards.

Material properties are needed to optimize circuit designs, and these properties are often dependent on the varying environmental conditions present during a product’s service life. Temperature and moisture are sources of environmental attack that are known to degrade some circuitry. However, stresses to a printed circuit board’s (PCB’s) copper lines may be induced by a number of sources, including mechanical shock and vibration.

Mobile telecommunications are one application for which strong consumer demand has motivated the production of smaller devices that have more complexity in their makeup and yet more stringent requirements in their application. Related products like cellular phones and personal digital assistants (PDA’s) must endure the rigors of seasonal change in addition to the

impact of an occasional drop. Descriptive of their design, high density interconnect (HDI) circuits are used in these applications where space and/or weight are limited. Although some people may expect a cell phone to break when it is dropped, similar circuitry is also used in undeniably critical applications that must withstand the loading imposed on them. Consider the Lucas engine management systems that regulate fuel supply to the Rolls Royce engines on Boeing 777 and Airbus 310 airplanes. Should these circuits (that are located outside the engine bodies and subjected to heat and vibrational loading) unexpectedly fail, the cost could be immeasurable.

Printed circuit boards are often made in laminate form, having multiple layers of a fiber-reinforced resin that are bonded together with their resin matrix. During the same curing process (under heat and pressure) in which the multiple layers of the laminate—the prepregs—are bonded together, a layer of copper film is placed outside of the layers of the composite on one or both sides. After cure, the outer layer (or layers) of copper film may be etched, leaving only the lines that will eventually conduct electric currents between the components (which are added to the circuit board later).

Delamination of the copper lines from PCBs is a common mode of failure in electronic circuitry. Visual inspection has shown that these bond failures may be either adhesive/interfacial (such that the copper and epoxy fracture surfaces appear to separate cleanly) or cohesive (for which the locus of failure is clearly within the PCB laminate, having resin and fibers on both failure surfaces).

1.2 Objectives

The objective of this study has been to quantify the fracture energies—the critical strain energy release rates—of the copper/epoxy bonds in four types of printed circuit board laminates. The critical strain energy release rates were expected to depend on time (speed of crack propagation), temperature, and the humidity conditioning. Companies that make and use printed circuit board materials often conduct quasi-static 90° peel tests to determine apparent critical strain energy release rates* of the laminates. These tests, however, have only provided information related to those quasi-static fracture speeds. To investigate the impact behavior of these materials, analysts have conducted simple drop tests in which populated circuit boards are physically dropped onto a hard surface. These impact tests clearly introduce additional variables, in that more is being “tested” than simply the bond in question. Furthermore, they only generate a single data point declaring whether or not the circuit has failed following a specific drop or, with repetition, the number of drops to failure. A testing method was therefore desired that could be used to measure the fracture energy for low-velocity impact (1-10 m/s) conditions of the copper/epoxy bonds. Furthermore, since data from quasi-static 90° peel tests had already been obtained, implementation of an existing impact test or development of a new impact test was desired that would facilitate direct comparisons between quasi-static and impact results. The time temperature superposition principle (TTSP) suggests that fracture energies at relatively high velocities are directly comparable to fracture energies measured at relatively cold temperatures. Since this TTSP is essentially used to extrapolate data obtained at slow test rates to impact velocity regimes based on temperature dependencies, direct measurements are desired to confirm conclusions based on TTSP.

* A significant amount of adherend plasticity has been evident in each of the peel tests conducted. For this reason, the critical strain energy release rates will be denoted as “apparent” or simply as “peel energies” throughout the remainder of this thesis with the understanding that the true critical strain energy release rates must be less than the quantities measured here.

1.3 Organization of Thesis

This thesis has been composed in a modular way. Chapter one, the Introduction, is provided as an overview of the scope of this study. Its purpose is to serve the reader by giving background, motivation, and objectives for the study in a more readable manner. Chapter two is a brief literature review. It is intended to give some history and include recent developments within the fields considered appropriate, so as to provide insights into the current study. Particular attention has been given to the development of the fracture test methods used during this study, since these were the author's primary focus. Chapters three and four are intended to be somewhat independent so that they might serve the dual purpose of being published as journal articles. As a consequence, some material in them parallels that found in other chapters. The concentration of Chapter three is on the loop peel test, whereas that of Chapter four is the falling wedge test. Results and conclusions relevant to the scope of this study are included in Chapter five. Within the appendices is included an overview of each of the testing methods considered, yet not pursued past the initial phases of this study, schematic drawings of fixtures designed and/or used for testing, certain programs written and used to obtain results throughout the chapters, and the results of surface analyses conducted by Dr. John G. Dillard using scanning electron microscopy and x-ray photoelectron spectroscopy. The author's vita is attached at the end.

Chapter 2. Literature Review

2.1 Fracture Testing

2.1.1 Development of Fracture Mechanics

In *A Text-book of Physics on Properties of Matter*, J.H. Poynting and J.J. Thomson¹ documented that Gauss, during his investigations of capillarity, used the principle that potential energy is a minimum for mechanical systems that are in equilibrium. Carl Friedrich Gauss investigated capillarity around 1830 and consequently developed the principle of the conservation of energy². The law of conservation of energy—the first law of thermodynamics—was not widely accepted until Hermann Helmholtz published a paper in 1848 showing its applicability³. Then R.J.E. Clausius introduced the second law of thermodynamics in 1850³. Gauss’ “theorem of minimum energy” applied by A.A. Griffith⁴ and others to fracture mechanics—which will be referred to as the “energy method”—is a specific application of the first and second laws of thermodynamics. It is the underlying principle by which the tests and analyses presented in the following chapters of this thesis were developed.

The energy method is not currently and has not been the only way proposed to explain and predict fracture phenomena. Prior to Griffith’s work in 1920, two commonly accepted hypotheses were that fracture would occur if a certain maximum tensile stress—or alternatively, a maximum extension—were reached⁴. Prompted by discrepancies between theory and experimental findings, Griffith showed that the accepted theories of rupture might have been at fault to the extent of 200 or 300 percent and thus inapplicable to describe the behavior of ductile steel. He then used Gauss’ principle of minimum energy as a basis upon which to develop an entirely new criterion for fracture. The energy method he proposed was not, however, immediately accepted as the sole nor best criterion for predicting fracture. And there remains a

large community of scientists who prefer an approach that uses a stress intensity factor, which is related to the energy method, to predict fracture. The stress intensity factor approach will be described as it appears in the following chronology of selected articles.

In 1947, H.A. Elliott published a paper extending Griffith's earlier work⁵. The condition for fracture described by Griffith defined the energetic state of the material, as calculated from an assumed stress distribution about existing cracks. Elliott noted that, "In the Griffith theory, it is implicitly assumed that once a crack is formed it is incapable of closing again." Recognizing that cracks in crystalline materials should tend to close due to inherent intermolecular attractive forces without the presence of competing forces to balance the former, Elliott extended Griffith's theory to account for the possibility. Because of their amorphous character, the glass materials that Griffith used to test his theory could have maintained small, internal cracks without the presence of an external tension. The broken bonds composing cracks in crystalline materials, however, may reform upon the release of what Elliott described as a critical external tension. Conversely, if the external tensile load exceeds the critical value required to maintain the existing character of the crack, the crack should grow. After developing a model to determine the state of stress and strain at all points with Griffith's—now extended—theory, Elliott finally proposed certain conditions for possible forms of a crack. These included small, weakly-bonded inclusions such as gases.

E. Orowan contributed to Griffith's theory by accounting for plastic energy. In his 1949 paper⁶, Orowan described various mechanisms for brittle and ductile fracture. He noted that both types of fracture might be preceded by plastic deformation at the crack tip. More significantly, however, was his assertion that ductile fracture does not obey a maximum tensile stress

condition. Contrary to Griffith's conclusion that fracture occurred when the local tension normal to the crack front reached a critical value, Orowan found that for ductile fracture, cracks extend by means of plastic deformation. Since plastic deformation "obeys either a maximum shear stress...or Mises-Huber octahedral shear stress condition," Orowan suggested that ductile fracture was instead caused by a local plastic strain condition (which is equivalent to a local shear stress condition).

R.S. Rivlin and A.G. Thomas applied Griffith's criterion to rubber vulcanizates⁷. Whereas Griffith assumed that the glasses he tested remained elastic until fracture, Rivlin and Thomas found that their vulcanizates remained elastic everywhere except very near the crack tips while tearing. Consequently, whereas Griffith's criterion provided a way to determine the surface energy of brittle materials, the corresponding energy term determined using the method proposed by Rivlin and Thomas was defined more generally as the work expended irreversibly per unit length increase of crack and per unit length thickness of test piece. Thus, the energy term using this method differs by a factor of $\frac{1}{2}$ from Griffith's (since the area of only one side of the new surface/crack is considered in Rivlin's model), and it allows for localized plasticity at the crack tip.

For cases of brittle fracture, G.R. Irwin discussed the use of a stress intensity factor to describe the stress field in the vicinity of the crack tip⁸. Irwin's stress intensity factor is proportional to the square root of the tensile force that drives the crack and may be determined via strain measurements taken at distances from the crack tip that are small compared to the length of the crack. He assumed conditions of plane stress or plane strain as well as that the driving tensile force was normal to the direction of propagation.

In 1961, J.P. Berry applied Griffith's criterion to poly(methyl methacrylate)⁹. Comparing a theoretical value for the surface energy based upon molecular structure to those values of "surface energy" determined experimentally using the energy method, Berry showed a difference between 4 and 5 orders of magnitude. He concluded that the experimental data was higher because of a viscous flow process.

J.R. Rice and G.C. Sih published a paper in 1965¹⁰ in which they presented a rigorous mathematical solution to the problem of two dissimilar materials bonded along a straight line. They imposed collinear cracks along the bond line and determined stress intensity factors that may be used in Griffith's (or another) fracture theory. S.G. Sawyer and R.B. Anderson then added to this work in 1972 by attempting to remove some of the ambiguity in the definitions for the stress intensity factors¹¹. They defined a new stress intensity factor of the interface.

E.J. Ripling and S. Mostovoy also described the use of a stress intensity factor, K , as a critical parameter for fracture¹². Recognizing the complex nature of adhesive bonds—often involving relatively thin, and compliant adhesive layers between thicker, and stiffer adherends—they said, "It is convenient to define fracture toughness in terms of energy rather than stresses for heterogeneous systems." The strain energy release rate, \mathcal{G} , was then used in an energy-based approach to determine the fracture toughness. The strain energy release rate described by Ripling and Mostovoy is similar to the energy parameter used earlier by Rivlin and Thomas, here defined simply as "the energy required to extend a pre-existing crack an infinitesimal unit of area." Ripling and Mostovoy provided relationships between K and \mathcal{G} for plane stress and plain strain conditions, supporting what Irwin had previously shown⁸. Then they presented some testing methods that may be used to determine the critical strain energy release rate required for

fracture to occur, G_c . These included a double cantilever beam (DCB) test and a tapered double cantilever beam test (TDCB), where the latter utilized a more complex geometry to alleviate the need to monitor crack length during test. Ripling and Mostovoy finally gave a brief description of the peel test, for which substantial plastic flow occurs in the peeled adherend. Consequently, comparisons between adhesive systems using the peel test require that certain test conditions be alike, including adherend material and thickness. While this may allow relative comparisons between adhesive systems, accurate estimates of fracture parameters remain difficult due to the extensive plastic deformation.

Confronting the problem of a bimaterial interface, A. Piva and E. Viola conducted a detailed analysis of the stress field at the crack tip¹³. Previous work of Rice and Sih, Sawyer and Anderson, and that of other researchers had left several ambiguities in this problem that Piva and Viola attempted to reconcile. Specifically, this includes whether or not the state of the stress field at the crack tip contains oscillating singularities, and the definitions of the stress intensity factors. Piva and Viola noted that previous works had included such things as the logarithms of lengths, which do not give a “meaningful result.” Piva and Viola also noted, “There is always a region, although very small, around the crack tip, where plastic deformation occurs...Therefore, the radial distance at which the crisis conditions” (that is the “critical” conditions for fracture) “must be evaluated should be related to the extension of the plastic zone.” They also noted later that their results seemed to confirm that the debonding was caused by failure in shear rather than tension. This appears consistent with Orowan’s theory discussed previously⁶. Finally, after a discourse focusing mainly on the use and validation of a stress intensity factor approach to the solution, Piva suggested that a formulation based on the strain energy release rate, G , could be used to investigate debonding at the interface. This would “eliminate the problems associated

with the oscillating singularities,” in addition to ambiguities in the definitions of and calculations of stress intensity factors.

By 1984, the question about oscillating stress singularities had been answered. In a brief review of adhesive fracture¹⁴, M.L. Williams said that, “The oscillatory character of the predicted stress singularities...[is] confined very, very closely to the crack tip, well within any local distortion due to, say, plasticity.” In the same review, Williams noted that some aspects of adhesive fracture had essentially come to be used independently by chemists, mechanicians, and physicists. Due to their different perspectives on the science, it was clear to Williams that some kind of collaboration should be made to compare and relate the different terminologies used, etc., and thus promote more rapid development of the science. He, therefore, petitioned the community of scientists who read his paper toward that end.

In a 1987 reference manual on Adhesives and Sealants¹⁵, K.M. Liechti reviewed various topics concerning fracture. He noted that most of the current practice/use of fracture mechanics was limited to the assumptions of linear elasticity. For these cases, he gave relationships to calculate the stress intensity factors for modes I, II, and III fracture. Liechti explained that the stress singularity at the crack tip predicted by the stress intensity factor approach was a mathematical artifact understood to describe a localized region of inelastic deformation, the size (or radius) of which could be determined with use of a yield stress criterion. He also suggested the possibility of “subcritical growth,” during which a crack may slowly grow even though the stress intensity factor is less than the value considered requisite for crack growth (the fracture toughness). Liechti then gave an overview of the energy-based approach that was initiated by Griffith. The strain energy release rate—the energy parameter currently sought to characterize fracture

toughness—is twice the surface energy density given by Griffith only for very brittle materials. More generally, however, the strain energy release rate is understood to account for inelastic effects located near the crack tip. Liechti then described various geometries used to test structural adhesives in various modes of loading and the fractography associated with each of the modes.

2.1.2 Test Methods

The first theories describing fracture mechanics dealt with cracks in infinite plates, which were soon followed by analyses describing cracks in plates of finite dimensions. A natural outgrowth initiated with Ripling and Mostovoy reduced the bounding plates into beams in the form of double cantilever beam test specimens. In the following section, literature pertaining to the use and development of DCB tests will be reviewed. This will then be followed by a review of some of the pertinent literature on peel tests.

2.1.2.1 Double Cantilever Beam Tests

M.F. Kanninen compared the way that various beam models described the behavior of quasi-static and unstable, rapid crack propagation using of the DCB test specimen¹⁶. Kanninen first used a simple beam on elastic foundation model to represent his DCB test specimens. He found that this model described the behavior of his quasi-static tests sufficiently well, but that it was unable to describe the behavior of his dynamic tests. Results from the dynamic (wedge-loaded DCB tests) included a constant steady-state crack velocity. By accounting for shear deformation and both lateral and rotary inertia forces, however, he was able to extend the previous model so that it agreed very well with his experimental findings. While developing his case, Kanninen pointed out that rather than attempting to predict stresses and/or strains at the crack tip with his

beam models, he was instead only using the models to calculate energy quantities “that can be determined much more accurately.” Specific conclusions from his dynamic tests included that “Inertia forces are important...even at speeds that are not large in comparison to the elastic wave speeds,” and that “Kinetic energy provides a very significant contribution to maintaining unstable crack propagation.” He also suggested, “Energy is dissipated at the crack tip at a rate which is primarily a material property.”

In 1978, S.S. Wang, et al. reported their finite element analysis study of the stress field at the crack tip of a DCB test specimen¹⁷. Their model accounted for elastic behavior and utilized “an advanced crack tip super element.” This special element reportedly gave an exact solution for the stress distribution. Ultimately, they concluded that their model provided results similar to those of previous researchers’ very near the crack tip for monolithic systems. Outside of that very limited region, however, their model showed significant differences from the monolithic case. Whereas the stress singularity in the monolithic case extended from the crack tip a distance equivalent to the beam height, Wang, et al. reported that their work predicted that a nearly uniform stress distribution would exist at a distance from the crack tip of less than one “adhesive layer thickness.” Thus, Wang, et al. suggested that the area around the crack tip that was significantly affected by the singularity at the tip was much smaller than the area that previous researchers had estimated for the same.

By 1987, DCB test specimens were being used to study fiber composites. J.G. Williams discussed the benefits of using loading blocks bonded to the ends of these specimens¹⁸. He also provided a correction factor to be applied to the strain energy release rate expression that would

account for the moments induced by the end blocks as well as for the effective shortening of the beam in the case of large displacements.

Williams published another work in 1988 in which he derived, in a relatively simple way, expressions that may be used to calculate the strain energy release rates for DCB and certain other test specimen geometries¹⁹. Williams showed that, for one-dimensional cases, a conventional beam theory approach could be used to give analytical results agreeing well with those from experiment. He gave expressions for both Modes I and II fracture.

In 1989, Hashemi, et al. discussed certain errors in the strain energy release rate calculations for DCB test specimens, and they offered suggestions for their corrections²⁰. They described an “R-curve” effect, for which the critical strain energy release rate appears to increase with increasing crack length. This phenomena, they showed, was an artifact of the method of calculation. Four different methods that could be used to calculate the critical strain energy release rate of a DCB specimen were discussed including: an area method, a compliance method, a load method, and a displacement method. Each of these provided unique results that were due in part to differences in the assumptions made in their development, e.g., the assumption that the beams are built-in cantilevers. Use of an end-correction term was therefore recommended with the load and displacement methods to account for rotation at the crack tip. B. Blackman, et al. published a similar paper in 1991²¹.

As a bit of a summary for the previous work, Williams published another article in 1989 on the fracture mechanics of delamination tests²². He noted that the anisotropies of fiber-reinforced composites could be accurately accounted for by fracture mechanics and that they even lead

toward a more simplified analytical approach, given certain assumptions and applying correction factors to account for large displacements, etc.

Hashemi, et al. published a detailed review on interlaminar fracture in 1990 to resolve problems of consistency and discussions on the accuracy of results that were beginning to riddle the literature²³. Hashemi, et al. based their analyses on linear elastic fracture mechanics, however, certain provisions were made if nonlinearities and/or hysteretic effects were slight. Each of these cases was based on the use of an area method for determining the strain energy release rate, G . Yet, the area method is somewhat imprecise in itself since it deals with average values of G . A better approach is to use beam theory to analyze the results. Referencing previous work, they showed how the use of beam theory enabled G to be partitioned into mode I and II components. They described a correction factor, X , to account for the non-built-in nature of the beams at the crack tip, a correction factor, F , to account for large displacements in the specimens, and a correction factor, N , to correct for stiffening in the beams caused by the presence of the end blocks. The combined effect of these corrections, they suggested, was typically a factor of less than 10% for the material systems that they considered.

In 1994, M.N. Charalambides and J.G. Williams reported on their studies that accounted for permanent deformation in DCB test specimens made of epoxy/glass-fiber laminates²⁴. They approached the analysis in several different ways that included an elastic plastic method, a linear-elastic/perfectly-plastic method, a linear elastic method corrected for large displacements, an uncorrected linear elastic method, and an area method. They considered geometric and material non-linearities. By comparing calculated values of G obtained using the elastic plastic method to those obtained with the area method, and by then comparing predicted crack lengths to

those obtained experimentally, Charalambides and Williams determined that the elastic plastic method provided the “correct fracture toughness.” They noted that the presence of fiber bridging during test would yield values for \mathcal{X} and E that are not true measures for the effect of crack tip rotation and the material modulus, respectively. These parameters will, however, still lead to a more accurate value of the fracture toughness. Charalambides and Williams also discussed the resemblance between results of their uncorrected linear elastic analysis and the “true” fracture toughness, but this was only a coincidence due to multiple counterbalancing dissimilarities.

Lim, et al. discussed a relationship between mode I, mode II, and mode III fracture toughness for wooden DCB specimens²⁵. Using a Japanese birch wood species and various commercial adhesives, they found that the strain energy release rates were dependent on crack length and, for a limited range of crack length, “almost independent of the geometry of adhesive joints.” Nevertheless, they reported the following increasing order of critical strain energy release rates: $\mathcal{G}_{Ic} < \mathcal{G}_{IIIc} < \mathcal{G}_{IIc}$. Lim, et al. added to this work in 1997 a study of the temperature and rate dependencies for the case of pure mode II loading²⁶. A viscoelastic effect was found. Lim, et al. then created a master curve with a shift factor plot, according to the Williams, Landel, and Ferry (WLF) equation²⁷. A break in the shift factor plot led them to believe that different mechanisms of fracture existed over the range of temperatures considered.

In 1995 and 1996, Blackman, et al. published a series of papers reporting the failure of fiber composite and bonded fiber composite fracture under high rates of test²⁸⁻³⁰. They sought to determine the critical strain energy release rates of each material system as a function of crack velocity using a linear elastic fracture mechanics approach. Previous work of other researchers had shown dependencies of \mathcal{G}_c that decreased significantly with increasing velocity, decreased

modestly, and even some reports of increasing dependencies. Blackman, et al., however, reported that the interlaminar fracture of their fiber composites showed either no rate dependence or a moderate decrease in fracture toughness with increasing rate, and the critical strain energy release rates of their adhesively bonded specimens decreased only modestly with increasing rate of test. Note that this apparent contradiction may be due to a material or temperature dependence. Blackman, et al. noted that tougher adhesives showed greater rate dependences. To achieve these results, they noted that at loading rates above about 1 m/s, dynamic effects obscured their test frame's measurements of displacement and load. Therefore, assuming that elastic moduli were not significantly affected by the rate of test, they used high-speed photography to determine the displacement and crack length information necessary to deduce the fracture toughness. Although observed phenomena at high rates of test included a propensity toward "slip-stick" behavior and oscillations in the measured values of G_C , Blackman, et al. noted that in their testing—which included rates of test up to 15 m/s—there was no need to correct for the dynamic, kinetic energy effects that could purportedly help drive a crack.

M.D. Thouless, et al. reported in 1998 that they were able to determine the fracture toughness of plastically deformed, wedge-loaded DCB specimens based on the post-fracture equilibrium state of the specimens³¹. They used a drop tower to accelerate a wedge directly into the bond line of various DCB specimens at rates of about 2 m/s and found that the adherends sustained a nearly constant radius of curvature after test. Thouless, et al. recognized this to be evidence that the fracture occurred under conditions of a constant moment, and assumed that the remaining strain energy in the beams was negligible after crack arrest. Then, knowing the material properties and the radius of curvature of the adherends, beam theory was used to estimate the energy consumed by the plasticity and to ultimately determine the fracture toughness of the specimens. The

fracture toughness was dependent only on the materials involved and not on the geometry of the bonded joint.

In 2001, Blackman and Kinloch published a standard to be used when conducting DCB and/or tapered double cantilever beam (TDCB) tests³². Detail is given describing suitable dimensions, tolerances, and measurements of the test frame and specimens before and during test. Suggestions are made for appropriate pre-conditioning parameters. And theories are presented for the post-test data analysis that include correction factors, where necessary, and notes on statistical recommendations. Sample forms are finally provided to aid collection and reporting of the data and results.

S. Xu, et al. used a novel falling wedge test to drive the fracture of DCB specimens under impact conditions³³. Using a drop tower to accelerate transparent wedges through the loading pins (within the end blocks) of fixed DCB specimens, Xu, et al. recorded the fracture events with a high-speed camera. Linear elastic fracture mechanics was then used to interpret the images during test, determine the displacements and crack lengths as functions of time, and to ultimately estimate the critical strain energy release rate during fracture. Corrections were made for stiffening of the adherends due to the end blocks, large deflections, and shear deformation and deflection at the crack tip. With the falling wedge test, Xu, et al. were able to show and discriminate between the fracture toughnesses of various adhesives during impact for temperatures ranging between -70 and 90 °C.

2.1.2.2 Peel Tests

Peel tests have been used as early as 1934³⁴ to measure adhesive and/or bond properties of thin and flexible adherends to much stiffer adherends. Early analyses of these tests considered elastic adherends bonded to rigid beams. Later researchers (cf. G.J. Spies³⁵) included elastic behavior of the foundations. In 1972, W.T. Chen and T.F. Flavin extended the previously used elastic analyses to include plastic bending of the peeled adherend³⁶. Chen and Flavin wrote a computer program to model the 90° steady state peeling of an elastic-plastic adherend from an elastic (Winkler) foundation. Their program predicted that the peel force would increase when/if the flexible adherend deformed plastically. They also suggested that peel force measurements obtained using different testing methods shouldn't be compared to each other.

K-S. Kim and N. Aravas derived a moment-curvature relation for pure bending of an elastoplastic beam³⁷. They also used a finite element analysis to study the stress and deformation fields at the crack tip. Under conditions of steady state 90° peeling, Kim and Aravas noted that, after unloading, the flexible adherend recoils to a shape of variable curvature. They then described “reverse plastic yielding” in the flexible adherend and the conditions for which it occurs. Finally, they presented an energy balance yielding the critical strain energy release rate for the bond as a function of the plastic dissipation and the residual elastic strain energy in the flexible adherend. Their universal peel diagram suggested energy magnifications of up to 90 fold, depending on the thickness, modulus, and yield stress of the peeled adherend.

Kinloch, et al. also discussed peeling of laminates for various peeling angles. In a 1994 paper³⁸, a geometry-independent fracture energy was sought that would represent the energy required to break the atomic bonds and the energy dissipated locally ahead of the crack tip due to plastic

and/or viscoelastic effects. They first modeled their system as an elastic-plastic beam attached to an elastic foundation. Then they predicted rotation angles at the roots of the crack tips as a means of comparison to experimental results. With specific attention being given to (i) stored strain energy in the peeling arm, (ii) energy dissipation due to tensile yielding of the peeling arm, and in particular (iii) energy dissipation due to bending of the peeling arm, Kinloch, et al. were able to show “excellent agreement” between their predicted and experimental results. They noted that the effects of mixed modes for varying peel angles were small, wherein the range of actual peel angles experienced at the root of the crack tips was smaller than the range of macroscopic loading angles. They also observed that their fracture energies decreased with decreasing crack tip velocities to a value that approached the theoretical thermodynamic work of adhesion.

In 1995 and 1998, A.K. Moidu, et al. published two papers discussing a model to predict the strain energy release rate for peel tests at any angle involving plasticity^{39,40}. In the former paper, their model considered the more flexible adherend as an elastic-plastic beam bonded to an elastic (Winkler) foundation. Compliances of both the adhesive and adherend were considered. The stiffer adherend was modeled as being completely rigid. By obtaining the curvature of the elastic-plastic adherend at its root (the crack tip), the plastic energy could be estimated and thus the strain energy release rate. In their 1998 paper, Moidu, et al. added to their previous model a means to account for the effects of foundation (adhesive) shear stresses and a bilinear stress strain relationship for the peeled adherend.

G. Ryschenkow and H. Arribart studied the stick-slip regime in peel tests using optical and atomic force microscope characterizations⁴¹. They noted that in peel tests, the fracture energy

obtained is proportional to the interfacial adhesion energy, the proportionality factor for which can be scaled using a WLF criterion. As described formerly by Maugis⁴², Ryschenkow and Arribart discussed how the phenomena of a stick-slip regime can be understood “as the result of the existence of two rising branches in the G versus velocity curve separated by a decreasing one.” The consequential saw-tooth shaped curve of the peel force versus time may be directly correlated with zones of adhesive or cohesive failure (although the adhesive zones also appear to be cohesive upon a closer inspection). The cohesive zones correspond to the “stick,” and the adhesive (or “quasi-interfacial”) zones correspond to the “slip.” They noted that at higher temperatures, as the (non-crosslinked) polymer softens, the roughness of the residual adhesive increases in the quasi-interfacial zone. In the macroscopically cohesive zone, there appears to be a transition in topography upon heating. At lower temperatures, the cohesive zone exhibits an apparently random distribution of linearly shaped protrusions. Upon heating, these linear bulges organize parallel to the peeling direction, then transform into a two-dimensional array of spherical cavities. Ryschenkow and Arribart attributed these results to the nucleation and growth of voids before the arrival of the peel front that are activated by a critical state of triaxial tension reached during the “stick” stages of fracture.

M. Barquins and M. Ciccotti studied the peeling behavior of adhesive tapes under a constant applied load, achieved by hanging varying amounts of weight on the free extremity of the tapes⁴³. The peel angles during their testing were approximately 90°. The stability of the debonding was dependent on the rate of test. At very low rates of test the peeling was unstable. Then at slightly higher rates of test, the peeling became stable, and the strain energy release rate increased as a power function with velocity. Furthermore, at very high rates of test, the peeling was also observed to be stable with a fracture energy that again increased with increasing speed

of test. There existed, however, a range between the two stable regions mentioned previously during which the peeling was unstable. Within this “stick-slip” range, the average peel velocity remains approximately constant. The peel force, and hence the strain energy release rate, however, oscillate. Furthermore, the occurrence of both light and acoustic emissions has been described during the stick-slip regime. M. Ciccotti, et al. later revisited stick-slip behavior and described the $G(v)$ curve as having only two regions of increasing slope⁴⁴. The middle region is considered to be experimentally unobtainable and unnecessary to explain the behavior.

In 1998, Y. Wei and J.W. Hutchinson published results on determining the intrinsic work of adhesion with use of the peel test when plastic deformation is significant⁴⁵. They developed a “cohesive zone model” to determine the macroscopic work of fracture as a function of its constitutive parts: the work of adhesion and the energy dissipated plastically ahead of the crack tip. Similar to the previous work of Kinloch, et al.³⁸, Wei and Hutchinson used the opening angle as a measure for the plasticity and ultimately the interface strength. They did emphasize, however, that the peel test remains to be a very difficult means—regardless of its ease to carry out—to obtain the interface adhesion energy whenever plasticity is apparent. They also noted that their model used conventional plasticity theory, and that there was evidence that this “significantly underestimates hardening and stresses when the gradients of plastic strain are large as, for example, at a crack tip.”

M. Ciccotti, et al. published a paper in 2004 discussing the complexity of peel testing⁴⁶. When polymers are tested, both temperature and humidity must be considered. At the onset of the stick-slip regime, the phenomenon is periodic, but it becomes increasingly irregular as the velocity is increased. This behavior has not been satisfactorily accounted for in the mathematical

models to date. Furthermore, if the peel angle is allowed to vary in the models, the results tend toward chaos. This too has not been satisfactorily considered.

2.1.3 Moisture

Much work has been done considering the effects of moisture on adhesively bonded joints. This topic was not, however, a significant part of the present research. Rather, attention was here focused on the mechanics studies, and as such, the following review is abbreviated and not specific to copper.

In 1996, M.R. Bowditch discussed the effects of water on adhesive joints⁴⁷. Water has been considered to be the most common hazard to adhesive joints, because it is abundant and usually adversely effects strength and durability properties of the system. Diffusion through the adhesive via exposed interfaces, diffusion through adherends, wicking and capillary action were all discussed. Noted also was that corresponding temperatures and time scales must accompany assertions on the effects of water. Fundamentally, organic compounds (whether relating to the adhesive, adherends, or both) are plasticized by the presence of water, which is usually accompanied by a decrease in fracture toughness. Bowditch noted that Orman and Kerr found that much of the strength might be regained upon drying⁴⁸. Similar results were found by Q. Ma, et al.⁴⁹. Bowditch also suggested that relief of residual stresses might be responsible for those cases where an increase in fracture strength was observed after exposure to moist environments. Even in these cases, however, excessive exposure has led to a weakening of the joint.

Chapter 3. Characterizing the Dynamic Fracture Resistance of Copper Foil Bonded to Printed Circuit Boards

3.1 Abstract

A novel test method—the loop peel test—is described in this paper and offers a means by which the fracture energy of copper film (or any relatively flexible adherend) bonded to a printed circuit board (or any relatively stiff adherend) may be measured at both quasi-static and impact velocities. It may have some advantage over the standard 90° peel test therefore, because it permits testing at speeds beyond the limits of most universal testing machines. Loop peel tests may be conducted with use of universal testing machines to obtain quasi-static results that relate directly to those obtained via standard quasi-static 90° peel tests, yet they may be conducted at low-velocity (1-10 m/s) impact conditions for little additional cost. Copper/epoxy bonds in four material systems have been tested using the quasi-static 90° peel test and the (dynamic) loop peel test methods. Test variables included time (speed of fracture), temperature (during test), and humidity (pre-test conditioning). The results are presented.

3.2 Introduction

Delamination of copper “lines” from printed circuit boards (PCBs) is a common mode of failure in electronic systems. These “lines” are thin, copper film conduits used to interconnect electronic components on a PCB (commonly made of a fiber-reinforced resin and copper laminated together). Because such bonds may be subjected to impulsive forces when, for example, a cellular telephone is dropped, a method is sought to characterize fracture energies corresponding to high-speed failure events. This data could later be applied to applications including high g-force shaking during vibrations and others.

The 90° peel test has been widely employed in quasi-static fracture testing of film adhesion, but complications resulting from its asymmetry make it difficult to use for high-speed fracture testing. As an example, simply dropping a load on the free end of an inverted 90° peel test specimen (Figure 1) results in uncontrolled swinging. A dynamic test that is relatively easy to conduct is therefore desired that will permit the direct comparison of dynamic fracture data to the quasi-static results obtained with the 90° peel test. The loop peel test has thus been developed to: 1) mimic the common 90° peel test so that direct comparisons between the two may be made, and 2) quantify the time-dependent (and temperature-dependent) fracture energy of peel specimens during high-speed fracture. Also, the effects of specific moisture conditioning were considered briefly. Swinging is avoided in the loop peel test because of its symmetry. The loop peel test has been successfully used to determine the apparent critical strain energy release rates* of four types of copper/epoxy bonds common to the electronics industry for low-velocity impact conditions (5 m/s).

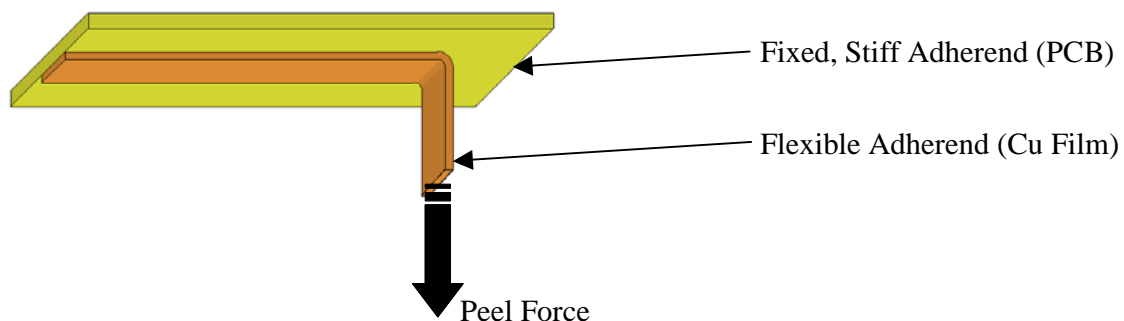


Figure 1: Inverted 90° peel specimen

* A significant amount of adherend plasticity has been evident in each of the peel tests conducted. For this reason, the critical strain energy release rates will be denoted as “apparent” or simply as “peel energies” throughout the remainder of this thesis with the understanding that the true critical strain energy release rates must be less than the quantities measured here.

The concept of the quasi-static 90° peel test is this: By measuring the force required to peel a flexible adherend (copper film) from a rigid substrate (PCB laminate) at a constant rate and while maintaining a 90° peel angle, the apparent critical strain energy release rate (or fracture energy) of that bond can be measured. This may be accomplished at slow (10^{-4} to 10^{-2} m/s) speeds by mounting a peel specimen horizontally in a universal (tension/compression) testing machine on a stage that can also translate horizontally. The flexible adherend may then be pulled vertically while measuring that force and while simultaneously moving the stage horizontally to maintain the 90° peel angle.

For test rates beyond the limits of common testing machines, a falling mass may be used to impart impact loading to the flexible adherend. The inertia of the mass would then resist any motion away from its vertical descent and thus necessitate the use of a stage that translates horizontally, as before, to maintain a 90° peel angle. Since the inertia of the stage would itself resist acceleration, at the moment of impact, the cracklength would increase and the peel angle would decrease—and continue doing so—until the tension in the tether (that connects the falling mass to the free end of the flexible adherend) is sufficient to pull the falling mass out of its vertical descent and back toward a 90° peel angle or until some other mechanism is able to accelerate the stage to a velocity equal to that of the falling mass. Although use of a very long tether may reduce the problem of a varying peel angle, the same introduces other complications and only further motivates the development of a test that doesn't have these encumbrances.

Therefore, to achieve higher test rates—consistent with fracture resulting from impact loading—the loop peel test may be used. The loop peel test may be thought of as the result obtained by forcing constraints of symmetry onto the quasi-static 90° peel test. Similar to the quasi-static

test, the apparent critical strain energy release rate is obtained from measurements of the force, P , which is required to peel each side of the flexible adherend from the relatively stiff adherend. By connecting the free ends of the flexible adherend (accomplished here by the addition of a separate length of copper film that was wider to avoid tearing), a “loop” is formed, by way of which impact loading may be imparted, as shown in Figure 2.

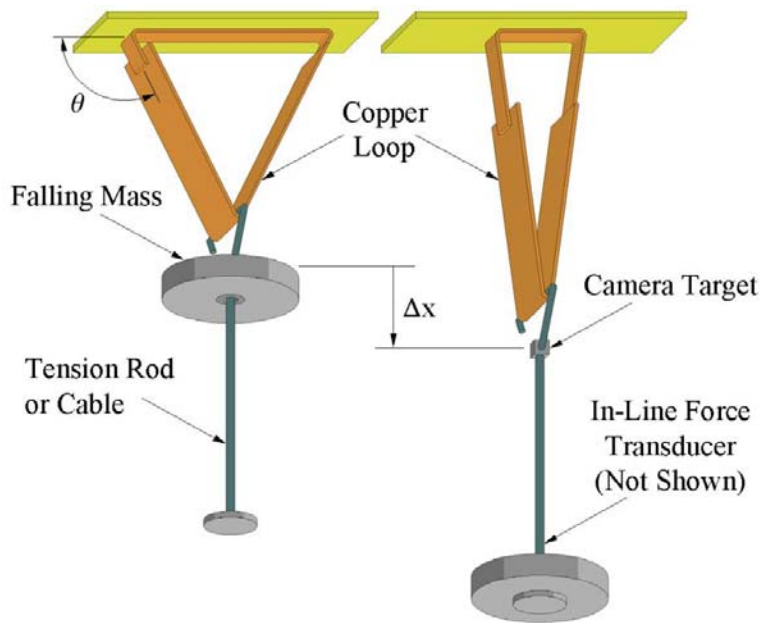


Figure 2: Loop Peel Test Configuration

3.3 Experimental

3.3.1 Specimen Preparation

Test specimens were made using four types of printed circuit board composites having epoxy matrices. These are specified in Table 1 with comparisons relating their composition in Figure 3. The laminated composite panels were each made with 16 prepreg layers and a single layer of ($\frac{1}{2}$ oz. per sq. ft.) copper film on one side. (Since the epoxy in each prepreg layer is only partially cured prior to being laminated, it is described as “B-stage”.) Each sheet of copper film had

furthermore been previously anodized on one side, producing a roughened surface to enhance the mechanical adhesion between the copper and underlying epoxy. Profiles similar to Figure 4 were used for the final cure of each PCB panel. Meanwhile, to support the use of the cure profiles, some of the B-stage epoxy (for materials E,N, and F) was tested using a Differential Scanning Calorimeter by TA Instruments, and the glass transition temperature of the epoxy was 175 °C. Although these PCB panels were originally prepared using a vacuum autoclave in our own facilities, we found that the DuPont Co., the sponsor, was able to produce panels with fewer surface irregularities in the copper film (which thus led to less frequent tearing during test). Consequently, we asked that they make the remaining panels as well as etch the copper on them to form narrow parallel strips in one direction. Finally, the specimens were cut to size. The completed specimens were approximately 25 x 200 x 1.63 mm (1 x 8 x 0.064 in.) with a centered copper foil strip along the entire length. The widths of the copper strips were 6.3, 7.6, or 8.9 mm (0.25, 0.30, or 0.35 in.), and they were approximately 0.017 mm (0.0007 in.) thick. (These various widths were used here to monitor edge effects.) Thus, four batches of test specimens were made, each corresponding to a different PCB laminate. And for each material type, test specimens were made having one of three possible bond widths.

Table 1: PCB Material Types

Manufacturer's Material Name	Designation Within This Article
E-Series THERMOUNT [®]	Material E
N-Series THERMOUNT [®]	Material N
THERMOUNT [®] RT	Material S
Fiberglass (FR4)	Material F

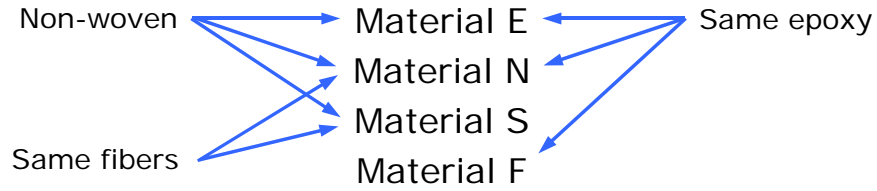


Figure 3: Comparisons of Material Composition

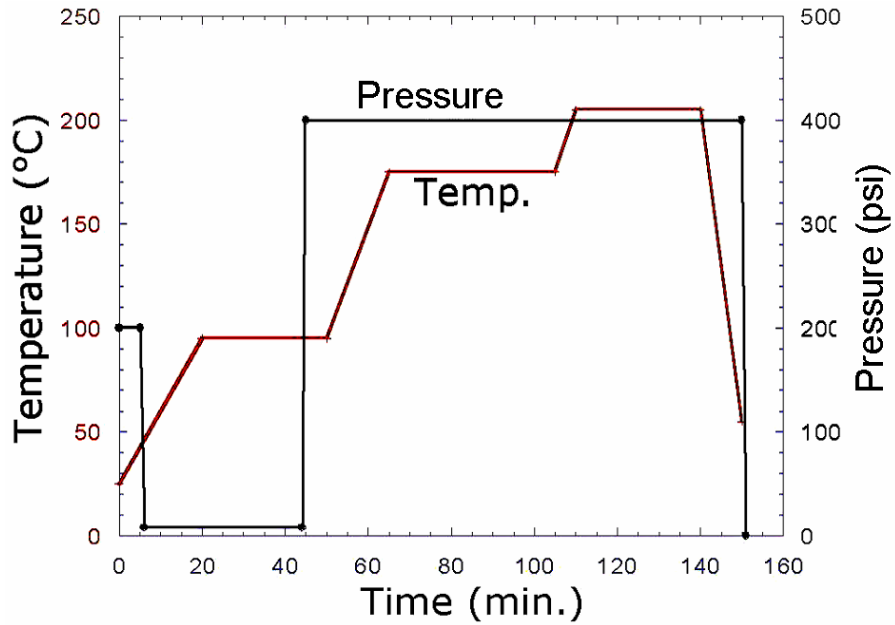


Figure 4: Sample Curing Profile for Epoxy Laminate

To further prepare the above specimens for a peel test, debonds were first initiated at one or both of their ends, depending on whether the specimen was to be tested using the standard quasi-static 90° peel method or the loop peel test method, respectively. Initiating debonds was accomplished by sharply bending the laminate about the side with the copper film until the laminate broke, leaving only the ductile copper film bridging the divided pieces of the underlying laminate.

Then, for the loop peel specimens, a separate strip of 12.7 x 0.05 x 400 mm (0.5 x 0.002 x 16 in.) copper was bonded (either by way of solder or a Kapton tape with a silicone-based pressure sensitive adhesive) to the free ends of the copper film. This completed the loops via which the loading device could symmetrically impart an impact to the copper/epoxy bond.

3.3.2 Method

3.3.2.1 Quasi-static Peel

Quasi-static 90° peel testing was conducted using an Instron testing machine (equipped with a 100 kg load cell) along with a custom fixture designed for quasi-static peel testing. Details on the peel testing fixture are in Appendix A.1. Of particular significance here is that this fixture had a translating stage that automatically maintained the set peel angle during test, assuming that the flexible, peeled adherend was inextensible. The rate of test was varied from 10^{-4} to 10^{-2} m/s. Test temperature (from -30 to 90 °C) was maintained via a heat exchanger that mounted directly to the stage of the peel fixture and which was supplied with either a chilled alcohol solution or a heated ethylene glycol solution. (A flat thermocouple was affixed to the PCB specimen to verify that the set temperature of the heat exchanger was realized within the specimen.) Furthermore, to keep ambient moisture from condensing and freezing on the surface of the specimen during sub-freezing testing, a plastic tent enclosing the entire fixture was made and filled with CO₂ (via dry ice). Finally, effects of humidity conditioning were considered by testing “dry” or “wet” samples that were conditioned for 500 hours prior to test at respective conditions of either 80 °C and near-zero percent relative humidity (maintained using a desiccant), or 80 °C and 80 % RH (maintained using potassium chlorate).

Fracture energy was obtained by dividing the change in energy (peel force multiplied by cracklength) by the change in area (bond width multiplied by cracklength). Thus, the apparent strain energy release rate was estimated as the ratio of peel force to bond width for quasi-static 90° peel tests.

3.3.2.2 Loop Peel

Impact testing was conducted with use of a Kodak EktaPro Motion Analyzer. This high-speed camera system (up to 12,000 frames per second) was used to precisely determine the vertical displacement of the camera target (shown in Figure 2) as it varied with time. The camera target consisted of a black bead of negligible mass with edges that could be easily recognized based upon their contrast with the surroundings. Its diameter was about 0.5 inches (13 mm). Also, contrary to the simplified depiction in Figure 2, a Dynatup drop tower was used to better constrain the motion of a 3.2 kg mass, and a 0.5 mm x 1.75 m (.02 x 67 in.) flexible stainless steel cable was used to transfer the force of the mass to the specimen. A limit switch was used to trigger the camera's recording upon the release of the drop weight. Determining the change in displacement with time was accomplished by first transferring the complete series of still images (initially stored in the camera's integrated computer) of the camera target to a computer via an image acquisition card. Using National Instruments' LabVIEW Vision Builder software, these images were then analyzed using a pattern matching routine to determine the vertical displacement, Δx , of the camera target for each sequentially captured image.

The displacement data is theoretically sufficient to provide the apparent critical strain energy release rate of the system when the initial geometry is known. By determining the acceleration or deceleration of a known mass as it falls, one should be able to compute the energy required to

propagate the debond. In practice, however, the required differentiation of the data produced results too erratic for use. For this reason, a 100 lbf piezoceramic dynamic force transducer (Model 208C02), purchased from PCB Piezotronics Inc., was placed in-line with the tether of Figure 2 (flexible cable), anchored on one side to the mass and having the tether affixed to the opposite side. A LabVIEW program was written to record this force as a function of time when triggered by the same limit switch that initiated the camera’s recording sequence. It was then possible to map force and displacement data together to obtain the change in energy of our system as a function of the vertical displacement. Furthermore, since our interests lay primarily in the limiting case as the debond angles approached 90°, that limiting vertical displacement could be directly interpreted as the displacement of both cracktips, assuming that the loop is inextensible. This furthermore negated the previous-held need to know the initial geometry of the specimen and loop. Therefore, the apparent critical strain energy release rate, G_c , during this fracture event could be obtained by dividing the integral of force over displacement (energy) by the same change in displacement (cracklength) multiplied by bond width, since this denominator in the limiting case also describes the change in area of the fractured surface. This is described by Equation 1, which assumes that stored energy is negligible due to the small load and stiff load train. The peel energy is furthermore described as “apparent,” because the work that is consumed in plastic deformation is not isolated.

$$G_c = \frac{\Delta E}{\Delta A} = \frac{\int F \cdot dx}{2w \cdot \Delta x} \quad \text{Equation 1}$$

3.4 Results and Discussion

3.4.1 Quasi-Static Overview

Three to five test specimens were fractured for each of the testing conditions. Rates of quasi-static peel tests spanned two decades. However, no differences in peel energy were observed

while varying these quasi-static rates. The rate of test within these quasi-static conditions was therefore recognized to be of lesser significance than changes in the temperature or humidity, and the results at varying rates were averaged under a single velocity of 10^{-3} m/s.

The apparent critical strain energy release rates under quasi-static conditions are shown in Figure 5 as they vary with temperature for each of the four printed circuit board materials tested. Error bars indicate one standard deviation above the average and one standard deviation below the average of the samples tested.

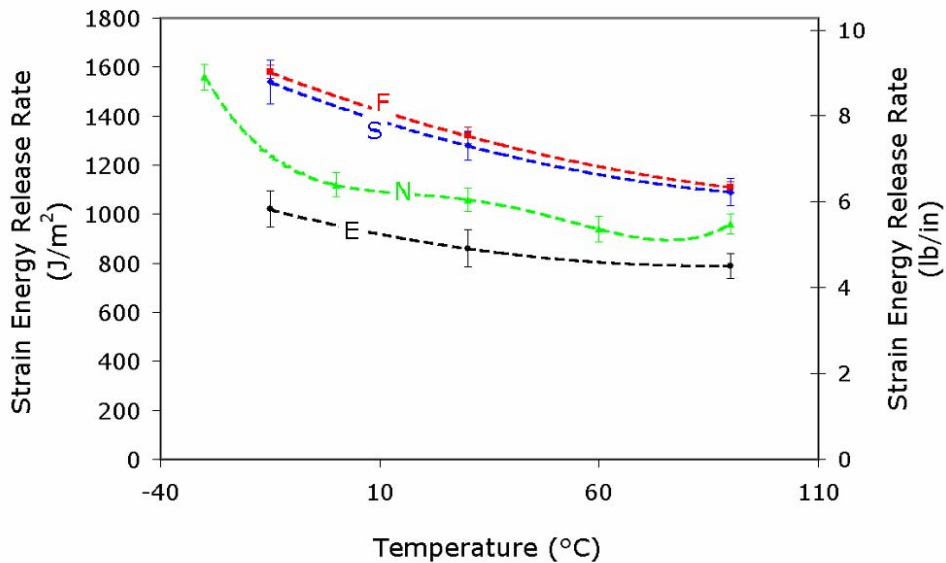


Figure 5: Quasi-Static Peel Results

Testing variables (as evident in Figure 5) for Material N are different because they were the first specimens made and they were tested at a different time than the others. If, however, the data for Material N is interpolated so that the test temperatures match those of the other materials tested,

it may be shown (See Figure 6) that the trend for Material N is very much like those of the other laminates. The peel energy decreases as the temperature increases. Note that the glass transition temperature is around 175 °C, and it is thus considerably higher than the test temperatures.

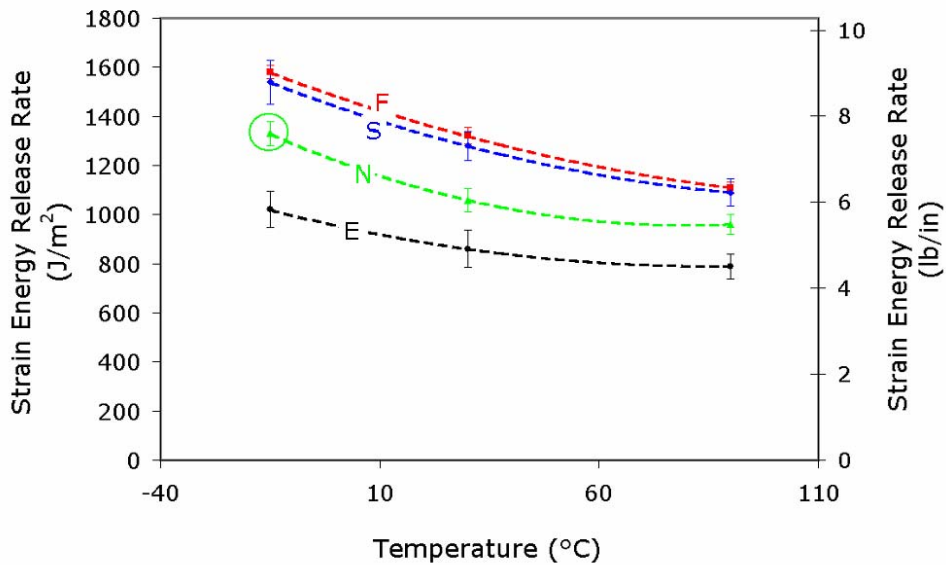
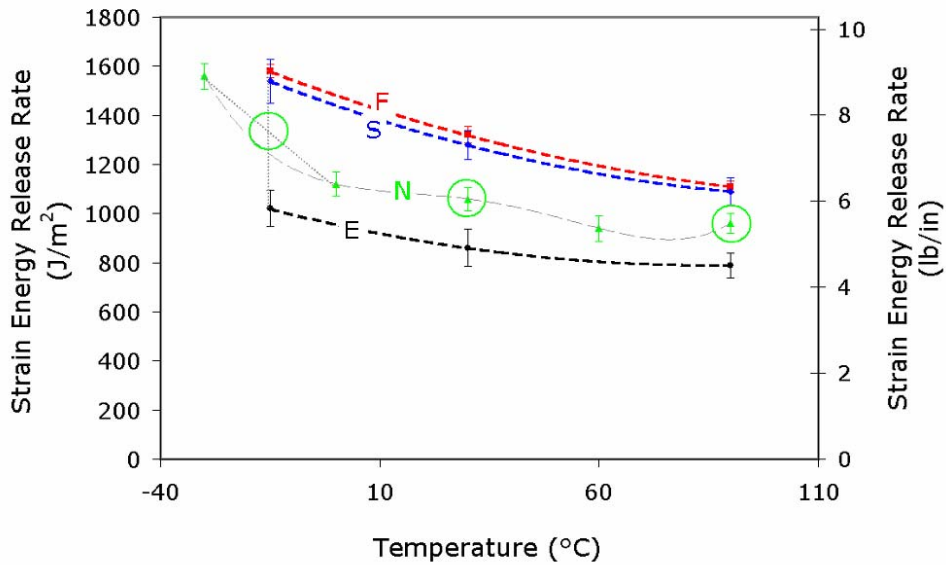


Figure 6: Comparison of Quasi-Static Peel Test Variables via Interpolation

This trend of decreasing peel energy with increasing temperature was unexpected, since results of previous researchers have shown the opposite behavior. Decreasing peel energy might be expected over a temperature range that encompasses the glass transition temperature. However, the T_g of these laminates is almost a decade higher than the results presented. Other variables that may account for these trends include rate-effects of the copper's properties. For example, if the yield stress of the copper were to decrease with increasing temperature, the amount of energy consumed plastically at higher temperatures would increase. Furthermore, if the plasticity increased, the thickness of the copper might vary. And it's possible that the properties of the copper could then change further as a result of the varying geometry⁵⁰.

Results of humidity conditioning on quasi-static peel energies are given in

Figure 7, where error bars again represent one standard deviation above and one standard deviation below the average values. Each material shows a decrease in peel strength with an increase in effective moisture content. The difference in average peel energies between the dry- and wet-conditioned samples decreases as the combined average increases. Thus the difference in "dry" and "wet" strain energy release rates for Material S is greater than the difference for Material F; the difference for Material N is greater than the difference for Material S; and the difference in "wet" and "dry" peel energies for Material E (which material consistently has the lowest peel strength compared to the others) is greatest of all.

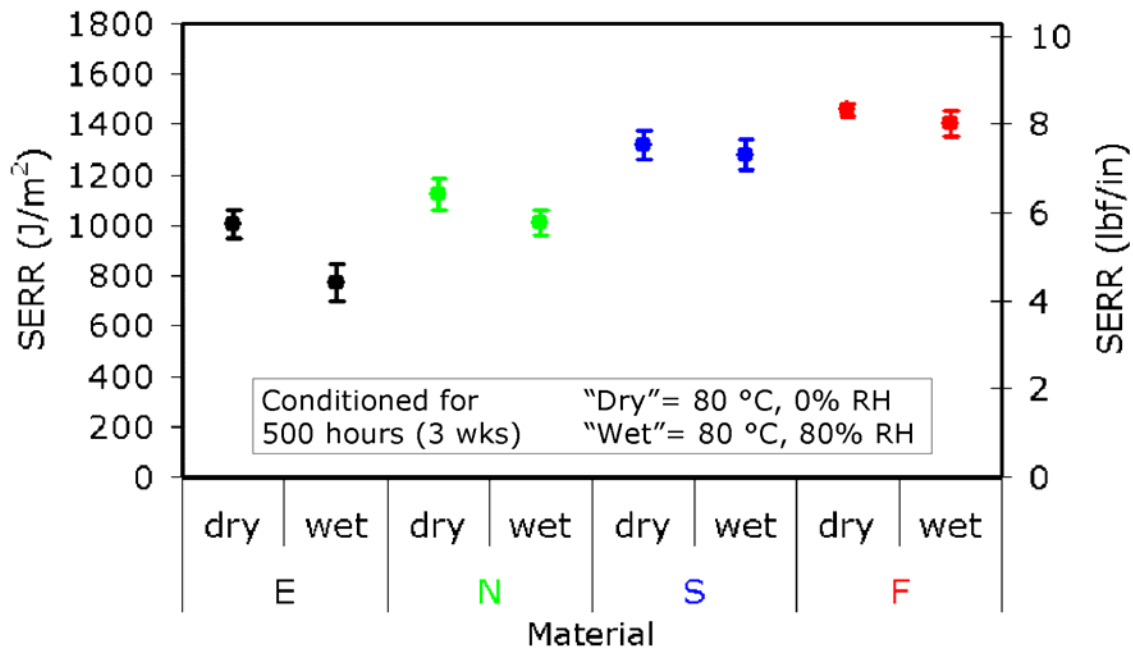


Figure 7: Effect of Moisture on Quasi-Static Peel Energies

The following four figures compare the non-humidity conditioned quasi-static peel test results with the results from humidity conditioning. This is done for each material by first combining the “dry” and “wet” data points into a single bar that encompasses the range between the averages shown in Figure 7, with an error bar extending above the average maximum peel energy value (the “dry” test condition) by one standard deviation and an error bar extending below the average minimum value (the “wet” test condition) by one standard deviation.

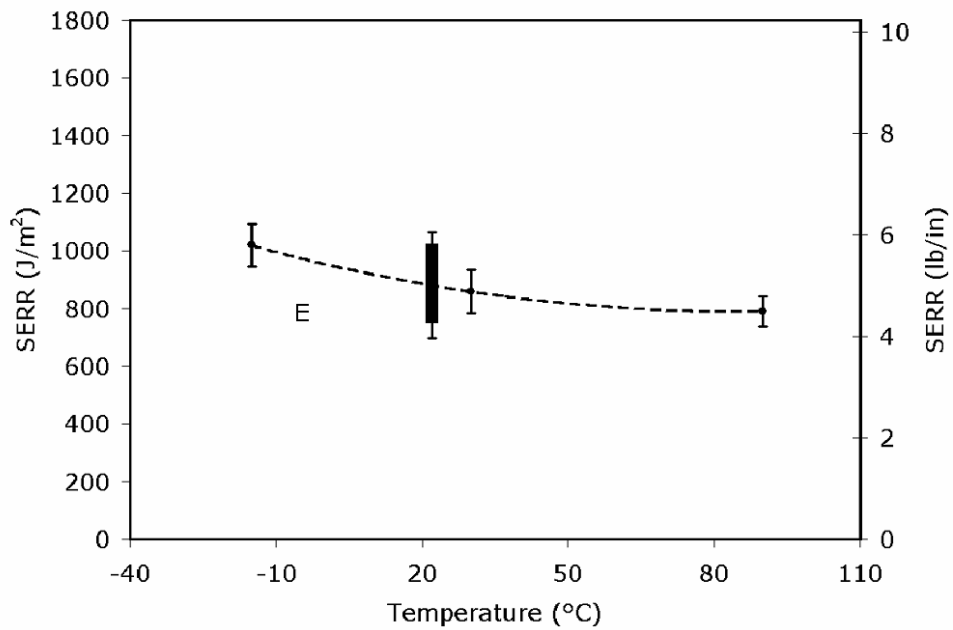


Figure 8: Superposition of Non-Humidity Conditioned to Humidity Conditioned Quasi-Static Peel Test Results for Material E

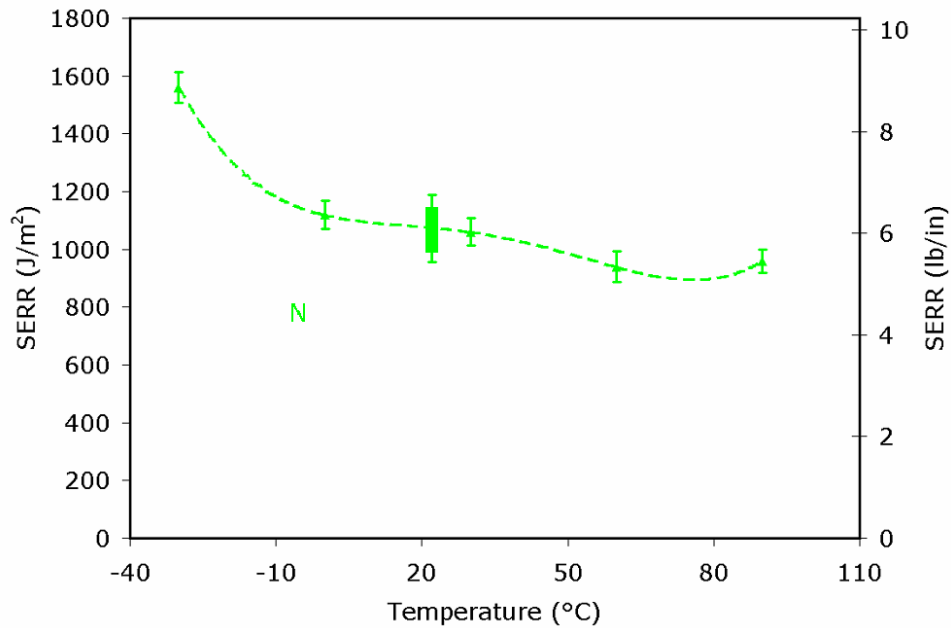


Figure 9: Superposition of Non-Humidity Conditioned to Humidity Conditioned Quasi-Static Peel Test Results for Material N

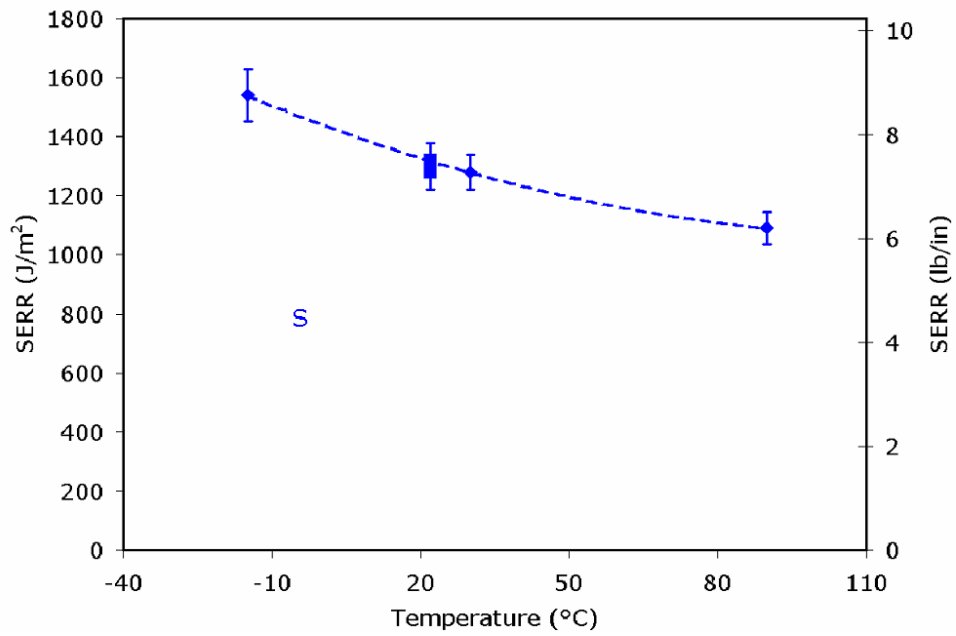


Figure 10: Superposition of Non-Humidity Conditioned to Humidity Conditioned Quasi-Static Peel Test Results for Material S

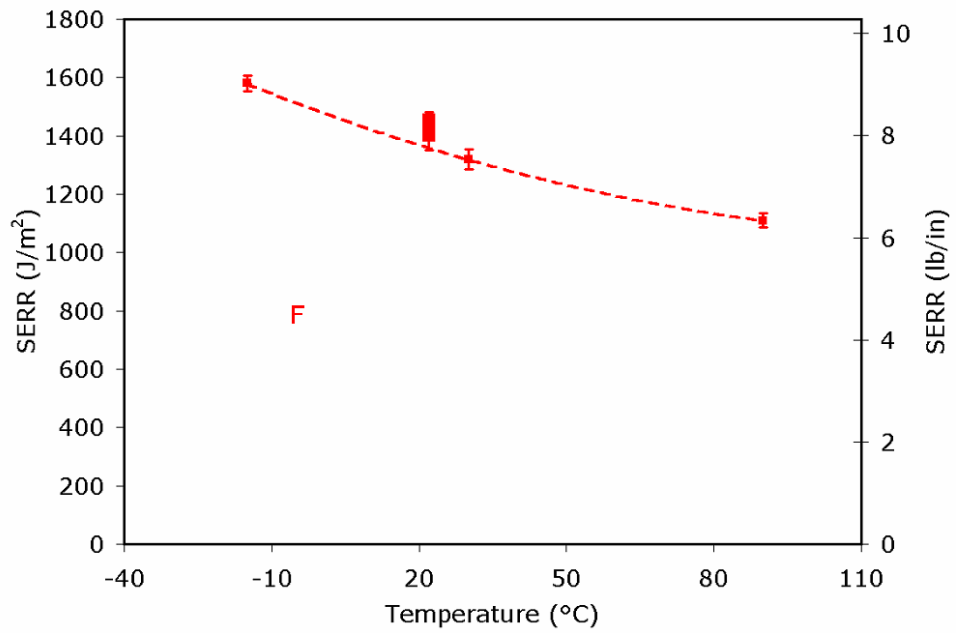


Figure 11: Superposition of Non-Humidity Conditioned to Humidity Conditioned Quasi-Static Peel Test Results for Material F

The trend lines for Materials E and N pass through the middle of the range bars obtained via pre-test humidity conditioning, whereas the trend lines for Materials S and F appear incorrect. Were more data available (as in the case of Material N), these latter trend lines might be shown to follow a different path that would pass through the ranges predicted by the humidity-conditioned testing.

3.4.2 Loop Peel Overview

Data obtained during a typical loop peel test for a copper/epoxy bond is shown in Figure 12. From this plot, the vertical displacement accelerates from zero velocity (zero slope on the displacement versus time plot) to a near-constant velocity of 4.2 m/s within the time encompassed by the first peak of the force signal. The final velocity is actually not constant as it appears from the plot, but it increases similarly to that of a free-falling mass. Since the entire fracture event occurs within 40 ms, this acceleration is not easily perceived.

Unlike the relatively stable action of the displacement during fracture, there is a significant amount of transient behavior evident in the force signal. The region of greatest acceleration in the displacement occurs when the force approaches and summits its highest peak. Furthermore, careful observation will show that when the force signal is at a local minimum, so also is the acceleration. The rising and falling of the force signal progresses much like a damped oscillation with a given steady-state value. This steady-state value to which the force signal appears to converge may be related to the constant force measured in quasi-static 90° peel tests, and the apparent critical strain energy release rate may be calculated directly with it. Another approach is taken here to determine the fracture energy that reduces the estimation that may be involved in determining the steady-state force as just described.

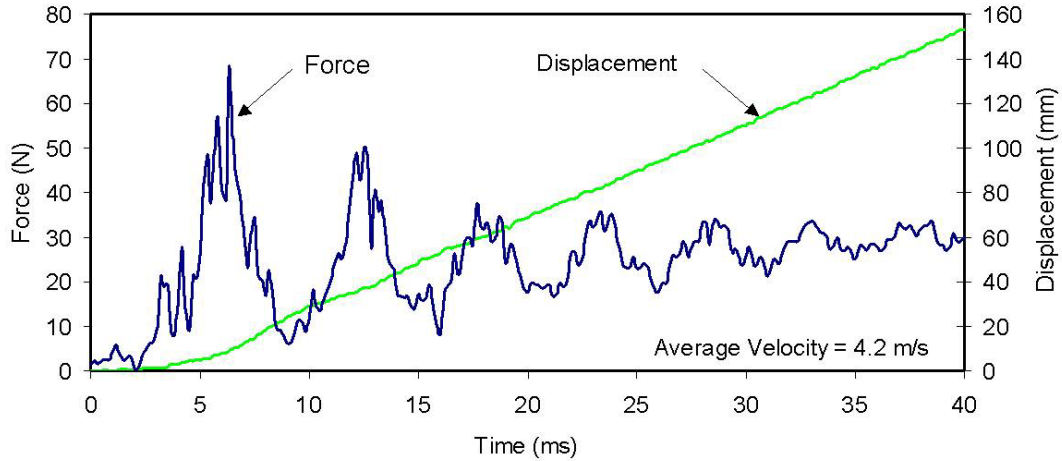


Figure 12: Typical plot of force and displacement as a function of time for a loop peel test

By mapping the above force to its corresponding displacement for each interval of time, the plot of force versus displacement presented in Figure 13 is obtained. This data was then numerically integrated, and the integral of force over displacement is also shown. Finally, by fitting a curve to the numeric integral, this change in energy (See Equation 1) during the fracture event is defined as a function of displacement. The apparent critical strain energy release rate (SERR), denoted by the variable G_c , may then be calculated according to Equation 1, since the critical SERR is equal to the SERR when equilibrium is reached.

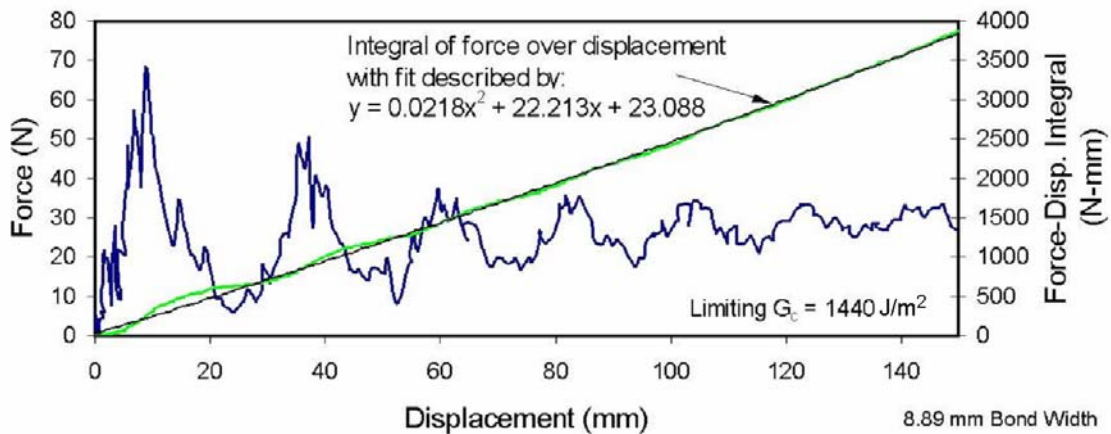


Figure 13: Relationships Used to Determine the SERR of Loop Peel Specimens

Loop peel tests were conducted over a temperature range from -85 to 125 °C with a Thermotron Industries (Holland, MI) oven. Since the oven was manufactured for use in conjunction with universal testing machines, it had a small hole in the top and in the bottom of the cooling/heating chamber. The drop tower could thus be positioned beneath the oven to consistently provide impact loading at given temperatures by fixing the loop peel test specimens in the top of the oven and allowing the loading cable to pass through the hole in the oven's base. This setup is shown schematically in Figure 14 along with a picture of the actual equipment used. The high-speed camera is positioned such that the camera target (small black bead attached to the tether) would just enter the camera's field of view as the tether became taught at impact. Also, two coil springs (not shown) were located above the mass to increase the speed at impact without the need of additional height with the drop tower. Clearly, similar impact velocities could be obtained without the use of a drop tower by employing stiffer springs to project the loading mass over a short distance.

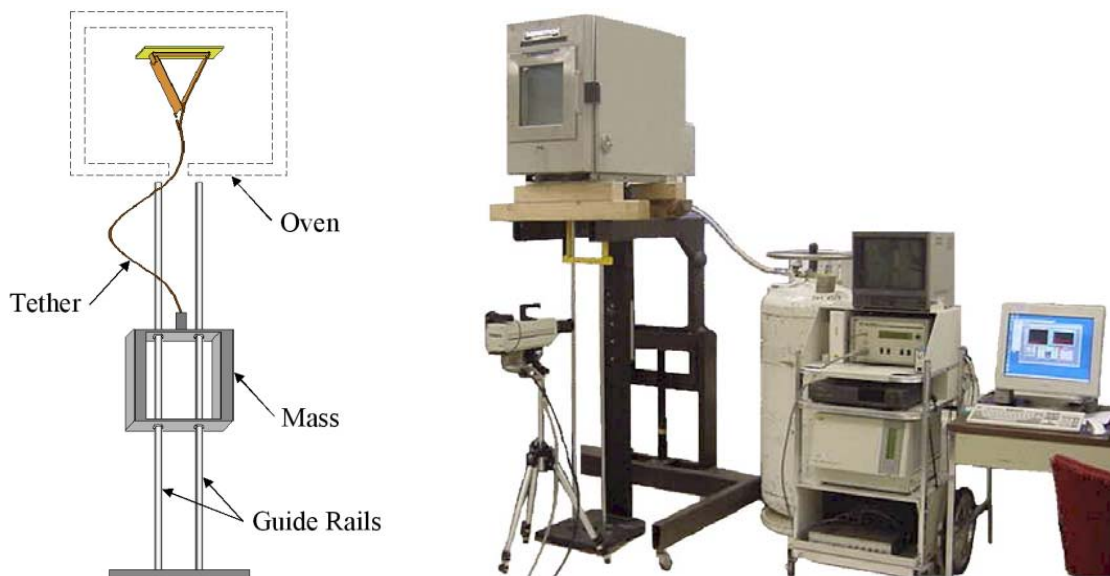


Figure 14: Loop Peel Setup with Drop Tower and Oven

Quasi-static, 90° peel tests were also conducted on each of the four material systems, according to the description in Section 3.2. These tests were carried out using an Instron testing machine at a rate of 60 mm/min (0.001 m/s). Thus the difference in fracture speeds between the averaged quasi-static 90° peel tests and the loop peel tests spans approximately 3 orders of magnitude. The apparent critical strain energy release rates obtained via quasi-static testing and via loop peel testing are plotted versus temperature together in Figure 16, Figure 18, Figure 17, and Figure 18 for the four materials, where error bars again describe ± 1 std. dev. in the data. The polynomial trend lines used in Figure 8, Figure 9, Figure 10, and Figure 11 describing the quasi-static behavior have been replaced by linear fits here. The trend of SERR versus temperature for both the loop peel tests and the quasi-static tests is consistent, in that—in every case—the SERR decreases with increasing temperature. The differences in peel energy values obtained via quasi-static peel testing and via (dynamic) loop peel testing are small for Materials N, S, and F. The difference in peel energies between the “two” test speeds for Material E, however, does appear to be more significant. (Note: A statistical verification of this difference was not made.)

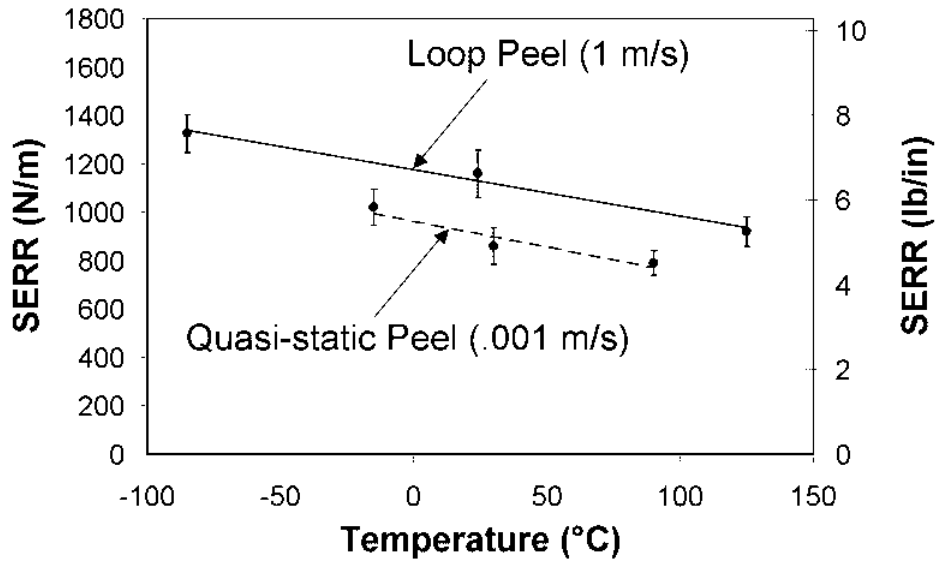


Figure 15: Comparison of Peel Energies under Varying Rate of Test and Temperature for Material E

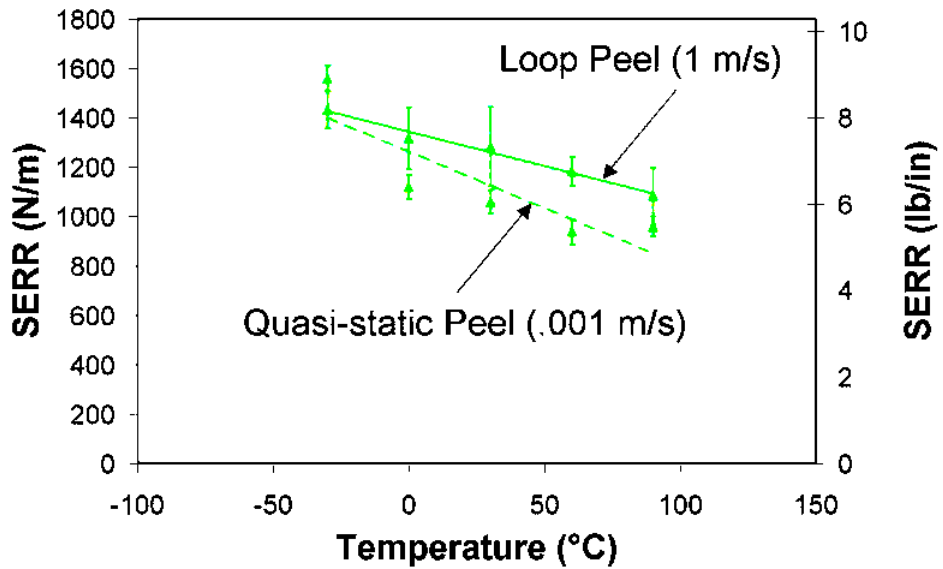


Figure 16: Comparison of Peel Energies under Varying Rate of Test and Temperature for Material N

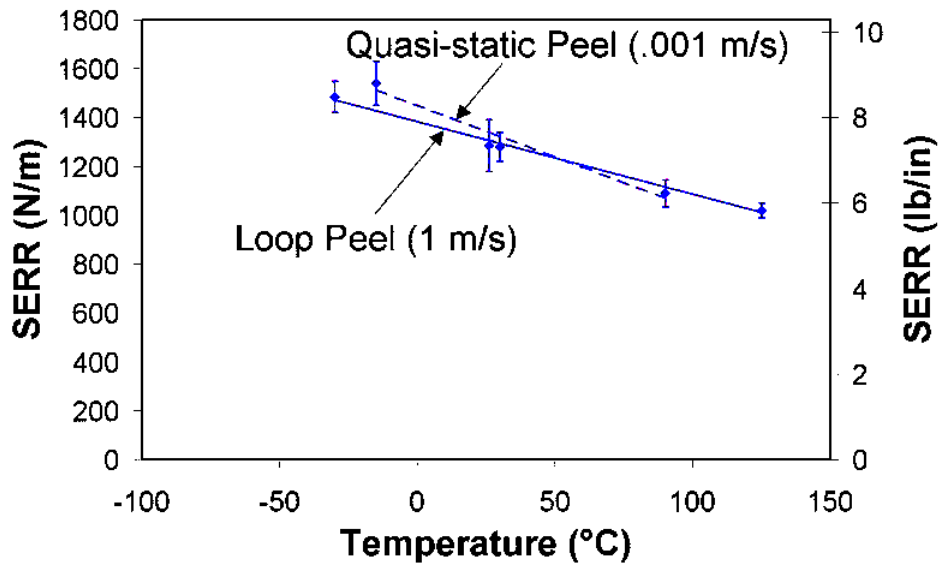


Figure 17: Comparison of Peel Energies under Varying Rate of Test and Temperature for Material S

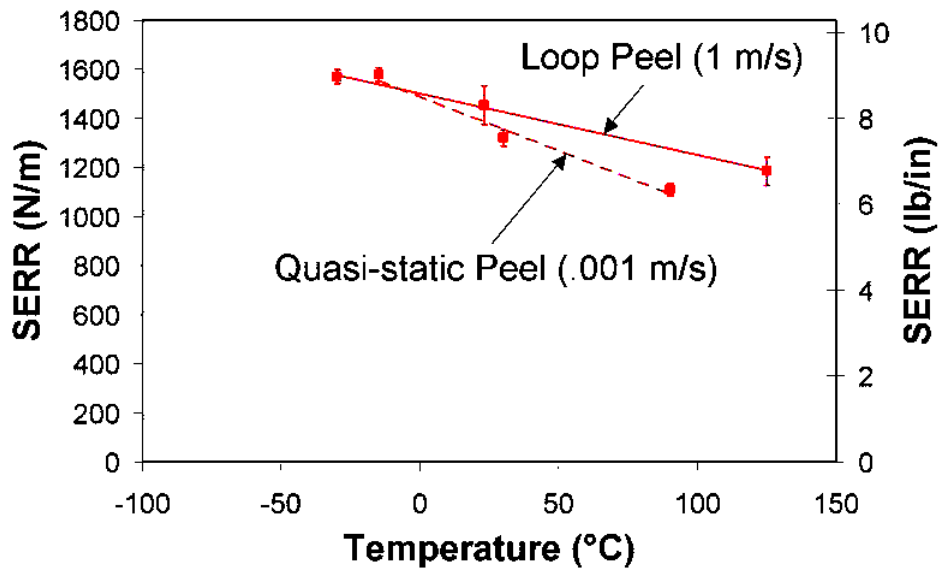


Figure 18: Comparison of Peel Energies under Varying Rate of Test and Temperature for Material F

3.4.3 Plastic Deformation

To approximate the amount of energy that is consumed in plastically deforming the copper, measurements of the radii of curvature were taken at the cracktip during quasi-static 90° peel tests. To accommodate measurements at the cracktip, the copper and PCB were “frozen” in their in situ configuration with a clear two-part epoxy. These “frozen” specimens were then encased again in another clear two-part epoxy that could be cut and polished smooth to reveal a clean cross-section of the cracktip. Figure 19 shows a typical specimen prepared as stated. The first two views clearly show the polished ends of the PCB’s reinforcing fibers in the lower halves of the pictures. The thickness of the copper was measured with a using a Nikon microscope. Then, using the thickness of the copper (.017 mm) as a reference scale, the radius of curvature at the root, that subtends an angle of about 50°, was determined to be approximately 3/2 of the thickness of the copper, or 0.025 mm (.001 in.). The darker, oxidized layer of the copper is assumed to have mechanical properties similar to that of the bulk material.

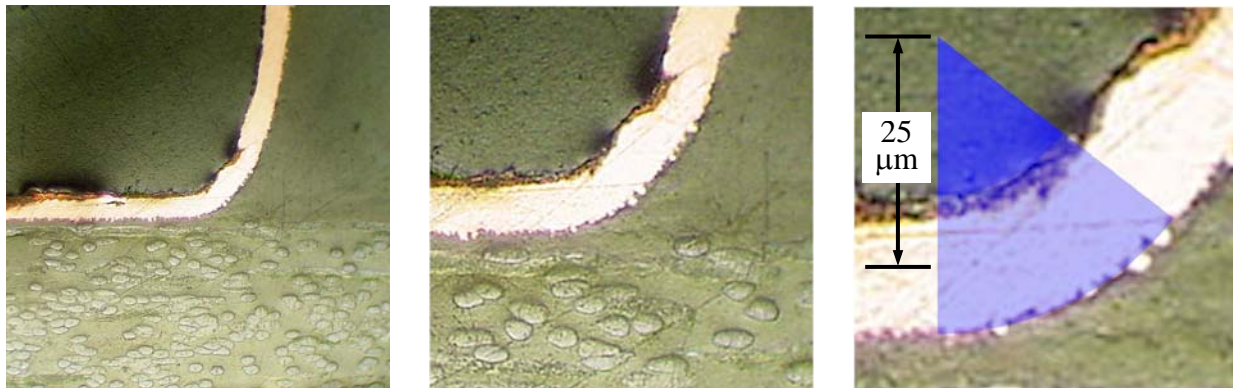


Figure 19: Curvature of Copper Film at Root During 90° Peel Tests

After conducting quasi-static, 90° peel tests and loop peel tests, plastic deformation caused the debonded copper to roll up. The radii of these rolls (as shown in Figure 20) were measured by hand with calipers and found to be approximately 2.25 mm and 1.75 mm, respectively, for all four PCB materials. In addition to observing no dependence on substrate materials, no

temperature dependence was observed in the apparent amount of plastic deformation sustained by the copper during test.

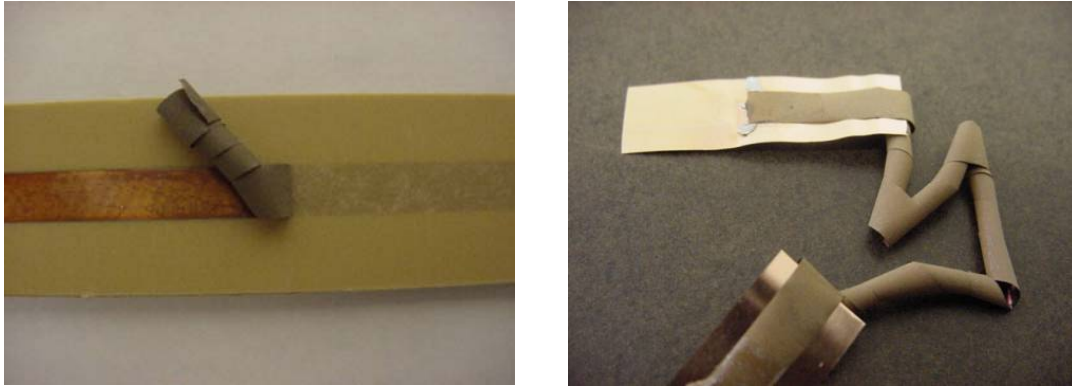


Figure 20: a) Deformed Cu from Quasi-Static Peel Test, b) Deformed Cu from Loop Peel Test

The loop peel tests resulted in copper rolls with smaller radii than in the quasi-static 90° peel tests partially because greater degrees of bending and thus plastic deformation are experienced during the earlier stages of fracture in the loop peel tests. This deformation is actually a function of the peel angle, but was here measured in an average sense. During a loop peel test, the peel angle is greater than 90° until the very end. This difference in peel angle may account for a higher fracture energy, for which a portion is due to increased plastic deformation. For this reason, the impact fracture energy corresponding to the quasi-static 90° peel test would be the limiting value obtained during the loop peel test, whereas the peel angle in the loop peel test begins at an arbitrary angle (about 60° in the present case) and approaches 90° as the test progresses.

3.4.4 Vibrational Analyses

Since the force signals (see Figure 12) exhibit behavior similar to the oscillations of common vibrations, the oscillations were analyzed to determine their causes and to consider possible

effects on the measurements of the SERR (or “peel energy”). The natural frequency of the loop peel test setup was first measured with regard to its axial vibration (in the direction of Δx) for the geometry at time equal to zero. The natural frequency was measured by first restraining the copper from debonding by securing it with small dowel pins, as shown in Figure 21a. The force in the tether, connecting the loop and mass, was then measured after striking the mass with a hammer. This test was conducted 3 – 5 times. The averaged response of these tests is shown in Figure 21b. Finally, the natural frequency of our system for the peel angle at the onset of fracture was determined to be approximately 11.5 Hz by analyzing the waveform of Figure 21b using a fast Fourier transformation (FFT).

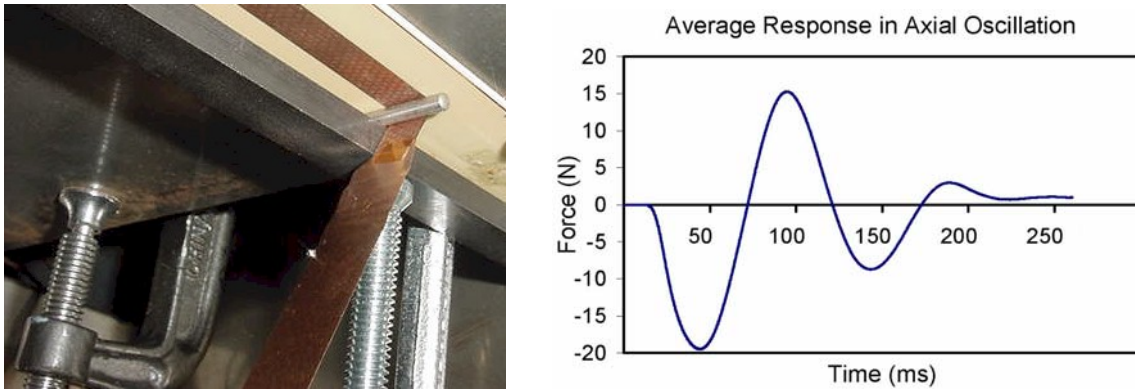


Figure 21: a) Restrained Loop, b) Natural Response in Vibration

This empirical result was then confirmed with vibration theory based on a simplified spring-mass system. Given a twisted steel ($E = 200$ GPa) cable of 0.5 mm diameter and 1.75 m length that is fixed on one end and has a mass of 3.2 kg on the other, the natural frequency in axial vibration may be calculated as:

$$\omega_n = \sqrt{\frac{k}{m}}, \text{ where } k = \frac{AE}{L} \quad \text{Equation 2}$$

Thus, by neglecting the effect of the copper loop, the result of the above calculation gives a natural frequency of 13.3 Hz, which only has a 16% difference from the measured value.

Meanwhile, FFT analyses were also conducted on the force versus time signals that were measured during each debonding test. Since the geometry of the loop changes during crack propagation, so also does the effective stiffness of the “spring-mass” system. Therefore, the dominant frequency observed in the data was also expected to be a function of time. Figure 22a shows the output of a simple FFT conducted on the data of

Figure 12, and a large peak corresponding to the dominant frequency is evident at 125 Hz. However, a fast Fourier transform requires that the waveform analyzed be one period in duration, and its output is thus constant for the same range of time. Therefore, to determine how this dominant frequency changes as a function of time, the following method was used: First, a smaller range of the force versus time signal was considered (e.g., $t_0 - t$), and a FFT was taken on this range of data. Then the range considered was stepped over in time (e.g., $t_0 + \Delta t - t + \Delta t$) and a FFT was taken of this new range. This process was then continued until the full waveform of force versus time for each test was analyzed. Due to the limited resolution of the FFT, however, this process was only able to provide one or two transitions in frequency for a given range of data (t minus t_0). By also varying the range in time (t minus t_0) considered by the FFT, the full frequency sweep over time was obtained for each test. Finally, these were collected, and the result is given in Figure 22b.

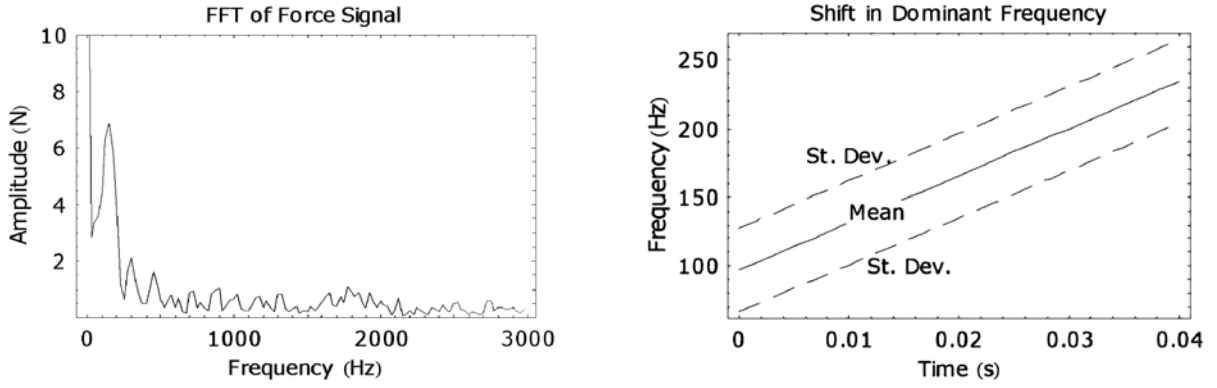


Figure 22: a) FFT of Force vs. Time Signal of Figure 12, b) FFT Results for all Loop Peel Tests

Next, vibration relating to motion of the tether transverse to its axis was considered. The natural frequency of a cable pinned on both ends and vibrating in its n th mode may be calculated as

$$\omega_n = n^2 \pi^2 \sqrt{\frac{EI}{mL^4}}, \text{ where } I = \frac{\pi \cdot r^4}{4} \quad \text{Equation 3}$$

To see if a transverse vibration mode might account for the oscillation in the force versus time signals, frequencies in that range (100 to 250 Hz) were substituted into the above equation to determine the modes that would be required to generate them. Consequently, the range of transverse vibration modes that would be required to produce the oscillations in our loop peel tests is from $n = 120$ to $n = 180$. These would have produced transverse waves in the tether with lengths on the order of 20 to 30 mm. Although transverse waves were visibly observed in the recorded images, their length scale was on the order of 200 to 300 mm. Furthermore, the observed motions were not consistent throughout the debonding period like the oscillations in the force versus time signals, and are therefore not considered to be the primary cause of the dominant oscillation.

3.5 Conclusions

The loop peel test has been successfully used to determine the apparent critical strain energy release rate (SERR) of peel specimens for low velocity impact conditions (5 m/s). Four copper/epoxy material systems common to the electronics industry were analyzed using standard quasi-static 90° peel tests and newly proposed loop peel tests. The amount of energy consumed in plastically deforming the copper film peeled from the printed circuit board laminates was independent of test temperature but dependent on the test method. The greater amount of energy consumed in plastically deforming the copper during the loop peel tests is attributed partially to the larger peel angles subtended during fracture. A statistically significant dependence was not found between the residual plastic energy in the copper and the material system. The amount of plastic energy retained was, however, found to be dependent upon the test method. Since the SERR for these loop peel tests was determined for the limiting case, as the peel angle approached 90°, the SERR should be comparable to that measured by way of a standard 90° peel test at an equivalent velocity.

The general trend for all of the quasi-static and dynamic (loop) tests conducted shows a decrease in peel energy with increasing temperature. This appears contrary to viscoelastic theory, since the glass transition temperature was significantly higher than the temperatures during test. Possible contributors to this effect have been proposed including modulus or yield stress dependences of the copper on temperature and/or rate. However, these hypotheses have not been confirmed.

Oscillations were observed in the data of the loop peel tests. Vibration analyses were then conducted on the data as well as the rigging used to conduct these tests, and the empirical results

were verified with vibration theory. The oscillations observed in the loop peel test data were found to be consistent for each of the material systems tested, and the dominant frequency of those oscillations was found to increase with time. This dominant frequency is considered to be unrelated to vibrations transverse to the loading axis, but it was measured to be within 20% of the natural axial frequency of the system. The increase in the dominant frequency with time may then be attributed to the stiffening of the effective spring constant of the loop as debonding progresses.

Values of the apparent critical strain energy release rate are based on the measured force versus time, without any filtering of that signal. Axial vibrations due to stretching of the load train suggest the need to account for stored energy in calculations of the SERR. All of the oscillations in the force versus time signals, however, decreased with time as the force converged to its steady state value. And the stored energy for the limiting case is considered to be negligible.

A high-speed camera system was utilized to precisely determine the change in displacement with time. Then, using a loading mass with a weight comparable to the force required to maintain quasi-static debonding, the displacement versus time signal was almost linear. Although a high-speed camera was utilized in the tests for this study, it is proposed that a camera may not be necessary to achieve the same results. Specifically, by providing a significant amount of potential energy by way of the falling mass, the amount of energy consumed by the fracture and related events will not be noticeable in the displacement signal during the fracture event. Consequently, if the speed of the mass at the time of impact is known, the slope for a linear displacement versus time signal may be thus defined. Then, by assuming that this displacement

increases from zero at a time near the onset of the force, the SERR may be estimated without the need of the high-speed camera.

Chapter 4. Use of a Falling Wedge Test to Determine the Fracture Energy of Printed Circuit Boards

4.1 Abstract

The purpose of this study was to determine the impact resistance of certain copper/epoxy bonds common to printed circuit boards (PCBs). A falling wedge test was used to determine the apparent critical strain energy release rate of one of these copper/epoxy bonds for low velocity impact (1-10 m/s) conditions, and the use of this test method is described. Quasi-static double cantilever beam (DCB) testing was also conducted. For both the impact and quasi-static tests, delamination was found to occur within the laminate of the DCB specimens used, rather than at the copper/epoxy interface. Fracture energies measured during impact were consistently higher than those measured during slower rates of test.

4.2 Introduction

Delamination of copper “lines” from printed circuit boards (PCBs) is a known mode of failure in electronic systems. These lines are thin, copper film conduits used to interconnect electronic components on a PCB laminate (commonly made of a fiber-reinforced resin). Because such bonds may be subjected to impulsive forces when, for example, a cellular telephone is dropped, a method is sought to characterize fracture energies corresponding to high-speed failure events.

Simple drop tests of populated circuit boards are one method used in attempt to quantify the fracture energy of copper/epoxy bonds. For a given drop height, the number of times a board of this type may be dropped without catastrophic damage is recorded and used for comparative purposes. The mechanics required to derive fracture energies from impacts of a populated circuit board are greatly influenced by undue complications including material properties and geometries of unrelated components. Therefore, a more straightforward method is desired to

measure the fracture energy of copper/epoxy bonds under impact conditions at the materials level. Drop tests of populated circuit boards may, however, provide other relevant information with regard to actual component failure. For example, visual inspection of failed surfaces has revealed that both adhesive (interfacial) and cohesive (within the epoxy) failures are likely to occur during such in situ testing.

Several testing methods have been used to study the impact resistance of adhesively bonded joints, some of which include the block impact test of ASTM D950, and an impact wedge-peel test (IWP)⁵¹. The fracture energies measured using these and other like tests, however, were dependent on the test system. A loop peel test (described in Chapter 3) has been used in the current study to investigate adhesive/interfacial failure during impact, and loop peel test results have been directly related to those of the quasi-static 90° peel test. Yet, even these tests are subject to plastic deformation in the adherends and fracture energies must be offset accordingly. Under certain conditions, quasi-static DCB testing produced failures within the epoxy-filled laminates without showing “machine sensitivity” and while retaining few observable plastic effects. A novel falling wedge test described by Xu³³ yielded comparable results to the quasi-static test for electrically conductive adhesives. This falling wedge test was thus used to investigate fracture of the PCBs prescribed in the current study for rates of test corresponding to low velocity impacts.

4.3 Experimental

4.3.1 Specimen Preparation

Test specimens were made using four types of printed circuit board composites having epoxy matrices. These are specified in Table 2. The laminated composite panels were each made with

16 prepreg layers and a single layer of (½ oz. per sq. ft.) copper film on one side. Each sheet of copper film had furthermore been previously anodized on one side, producing a roughened surface to enhance the mechanical adhesion between the copper and underlying epoxy. Profiles similar to Figure 23 were used for the final cure of each PCB panel. Although these PCB panels were originally prepared using a vacuum autoclave in our own facilities, we found that the DuPont Co., the sponsor, was able to produce panels with fewer surface irregularities. Consequently, we asked that they make the remaining panels as well as etch the copper on them to form narrow parallel strips in one direction. Finally, the specimens were cut to size. The completed specimens were approximately 25 x 200 x 1.63 mm (1 x 8 x 0.064 in.) with a centered copper foil strip along the entire length. The widths of the copper strips were 6.3, 7.6, or 8.9 mm (0.25, 0.30, or 0.35 in.), and they were approximately 0.017 mm (0.0007 in.) thick. Thus, four batches of test specimens were made, each corresponding to a different PCB laminate. For each material type, test specimens were made having one of three possible bond widths.

Table 2: PCB Material Types

Manufacturer's Material Name	Designation Within This Article
E-Series THERMOUNT [®]	Material E
N-Series THERMOUNT [®]	Material N
THERMOUNT [®] RT	Material S
Fiberglass (FR4)	Material F

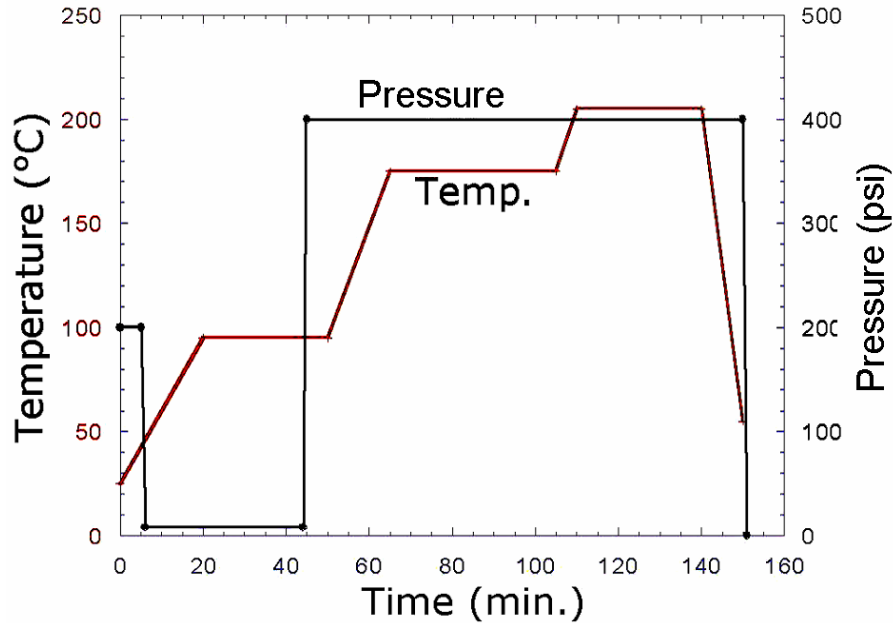


Figure 23: Sample Curing Profile for Epoxy Laminate

To further prepare the above beams for a falling wedge test, two beams (of the same material and having the same width of copper) were bonded together in a double cantilever beam (DCB) configuration. Since the copper film did not cover the entire width of each beam, a method was needed to bond the copper of one beam to the copper of another without also bonding the adjacent and exposed surfaces of the PCB laminates together. The purpose in using a bond width that was less than the beam width was to decrease the effect of plastic deformation and/or damage during test. Consequently, two primary methods were used in the attempt to bond the copper strips of the beams together. Since it was known that solder readily bonds to copper and not these PCB laminates, solder was used in each case. It was presumed that failure would occur somewhere other than at the copper/solder interface.

In the first case, Kester 256 solder paste was used to bond the DCB beams together. This paste was chosen because it is common in the industry. It has a 63/37% lead/tin composition. A bead of paste was applied to the copper strip of one beam with a small spatula. Then the opposite

beam was pressed against the first and clamped along its length using binder clips on both sides. A Model GF-B Gold-Flow reflow oven (Automated Production Systems, Inc.) was then used to solidify the solder. Due to the large thermal mass of the beams and the binder clips, however, the manufacturer's suggested heating profile for the paste was not sufficient. By embedding a thermocouple in the paste, the temperature was monitored to determine the thermal lag along with a more effective heating profile for the DCB specimens. The time elapsed prior to reflow when the oven was set at the suggested reflow temperature of 220 °C (430 °F) was approximately 15 minutes. To reduce the reflow time, an isothermal soak of 330 seconds at 260 °C (max oven temp.) was programmed on the oven. At this setting the temperature inside the oven was 215 °C (420 °F), and the solder paste was able to reflow consistently.

In the second case, 0.5 mm (0.02 in.) diameter, Kester #58/245 solder wire was used to bond two similar beams into a DCB configuration. Parallel rows of these wires were aligned between the copper faces of each beam and held in place by clamping the beams with binder clips as done above. These beams were then heated using the same isothermal soak conditions as above to cure the bond. This 63/37% solder wire has a flux core, but better wetting of the copper was achieved when the copper surfaces were first cleaned with Rubyfluid (soldering and tinning flux, made by the Ruby Chemical Co.). Ten parallel wires of solder provided enough material to the joint to consistently accommodate adequate wetting of each copper face. Excess solder was squeezed from the joint under the pressure from the binder clips. Due to the relative ease of preparation and lack of residue from a carrier resin, this second method of bonding using solder wires was employed to bond the beams of each falling wedge test and quasi-static DCB test specimen.

After the two halves of each DCB specimen were bonded together, cracks were initiated on one side having a length of 35 – 50 mm (1.5 – 2 in.). This was accomplished by pressing a knife blade into the corner of the specimen next to the bonded area. The two beams could then be pried apart until the cracklength was sufficient. Once cracks were thus initiated, loading hinges were bonded to each side of the specimen at that same end. This is illustrated in Figure 24. The loading hinges were cut from either aluminum or stainless steel piano hinge stock and had a bond area of approximately 250 mm² (.37 in²). Initially, a cyanoacrylate (CA) adhesive was used for this purpose. The CA adhesive was not adequate for either the low (< -30 °C) or high (> 90 °C) temperature testing however, so a two-part epoxy was used to bond the hinges to the PCB beams.

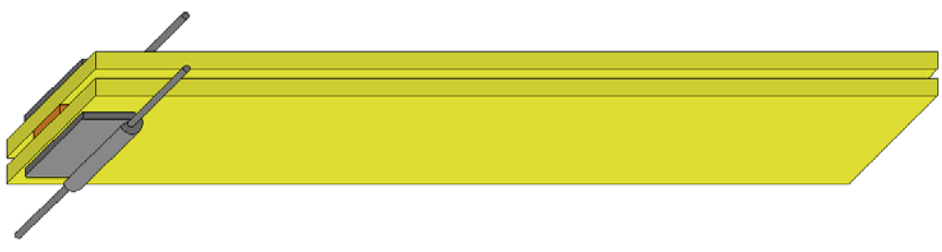


Figure 24: DCB Specimen with Loading Hinges and Pins

All specimens were stored in polyethylene bags at approximately 22 °C (72 °F) until the day of testing. To remove moisture prior to testing, they were then baked 4 hours in a convection oven at 105 °C (220 °F) and allowed to cool to room temperature.

4.3.2 Falling Wedge

Following the work done by S. Xu³³, falling wedge tests were conducted on a modified Dynatup drop tower. Two clear, polycarbonate wedges were mounted to the drop tower sled that had a 30° opening angle. DCB specimens could then be mounted vertically at the base of the tower so that, when activated, the falling wedges would strike the loading pins on the specimen and drive the crack. This is illustrated in Figure 25.

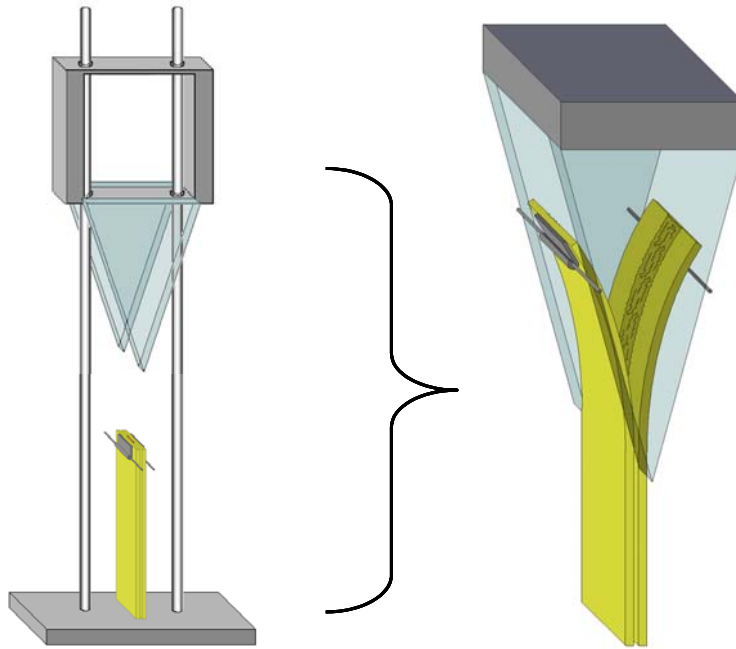


Figure 25: Falling Wedge Test Setup

Specimens tested at temperatures below or above ambient conditions were placed in a convection oven and allowed to equilibrate at the prescribed setting. They were then removed from the oven, placed into the test frame, and fractured. (The time prior to fracture during which each high- or low-temperature specimen was exposed to ambient conditions was from 10 – 15 seconds.) A thermocouple was then immediately placed against the fractured surfaces to verify that the temperature of the bond line remained at the conditioned temperature during fracture. This temperature change was consistently less than 3 °C (5 °F).

There are several accepted ways to determine the critical strain energy release rate for DCB specimens²¹. A displacement-based approach with corrections for large displacements is used here, as S. Xu had done³³. Thus, the apparent critical strain energy release rate, G_c , may be found as a function of the specimen geometry and the bending modulus of the beams at any moment of time during fracture.

$$G_c = \frac{9\delta^2 EI}{4wa^4} F, \quad \text{Equation 4}$$

where δ is the opening displacement, EI is the flexural modulus, w is the bond width, a is the cracklength, and F is a correction factor for large displacements given by³²

$$F = 1 - \frac{3}{10} \left(\frac{\delta}{a} \right)^2 - \frac{3}{2} \left(\frac{\delta l}{a^2} \right), \quad \text{Equation 5}$$

where l is the distance from the center of the loading pin to the middle of the beam on one side. It must be noted, however, that these equations are based on the static deflections of beams and therefore do not include inertial terms and/or account for higher modes that are evident in videos of the dynamic tests.

A Kodak EktaPro Motion Analyzer was used to determine the specimen geometry during test. Images from this high-speed camera system (up to 12,000 fps) were transferred to a PC for processing. With the aid of National Instruments' LabVIEW and Vision Builder software, a program was written to read each sequentially captured image of the fracture event, obtain coordinate data describing the profile of the specimen as displayed in each image, and then output a data file of the results for that test specimen (See Figure 26). Post-processing of this data was originally attempted using LabVIEW code, but it was discovered at the time that LabVIEW's nonlinear curve fitting algorithm did not converge to an accurate result. For this reason, a *Mathematica* program was written for all of the post-processing requirements.

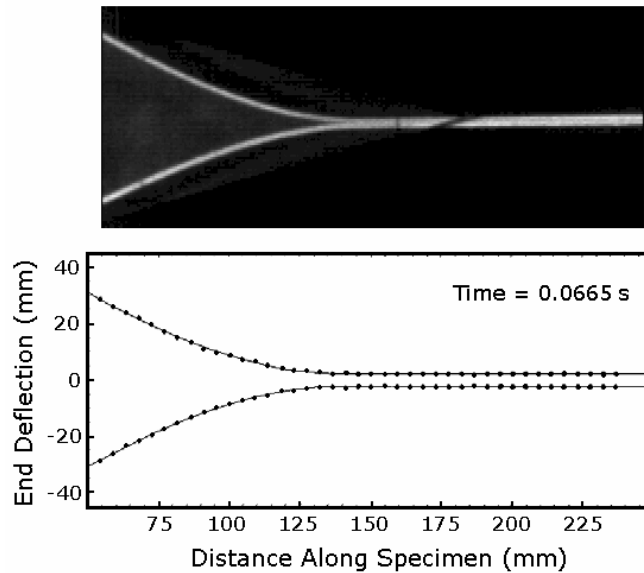


Figure 26: Falling Wedge Test Image and Digitized Beam Profile

It is understood that bending stiffness is dependent on strain rate and temperature for viscoelastic materials. Therefore, a Dynamic Mechanical Analyzer (DMA) made by TA Instruments was used to estimate the effective modulus during test. Dual cantilever beam specimens were made from each PCB material, both without copper bonded to one side and with copper bonded to one side (covering the entire side). These cases were chosen to represent the limits of the expected range of moduli during an actual test. The dual cantilever beam specimens had dimensions of approximately 9 x 55 x 1.63 mm (0.35 x 2.17 x 0.064 in.). Their effective lengths were 35 mm (1.38 in.), as determined by the DMA loading fixture. These specimens were cyclically loaded at frequencies between 0.1 and 100 Hz for temperatures between -120 °C and 245 °C (-185 °F and 480 °F) in 5 °C increments using an oscillation amplitude of 30.0 μm (1.18 mil). Then

master curves were produced of the storage modulus versus oscillation frequency for each case, along with their corresponding shift factor plots—according to standard practice. The time-temperature superposition master curves for E-Series Thermount are given in Figure 27.

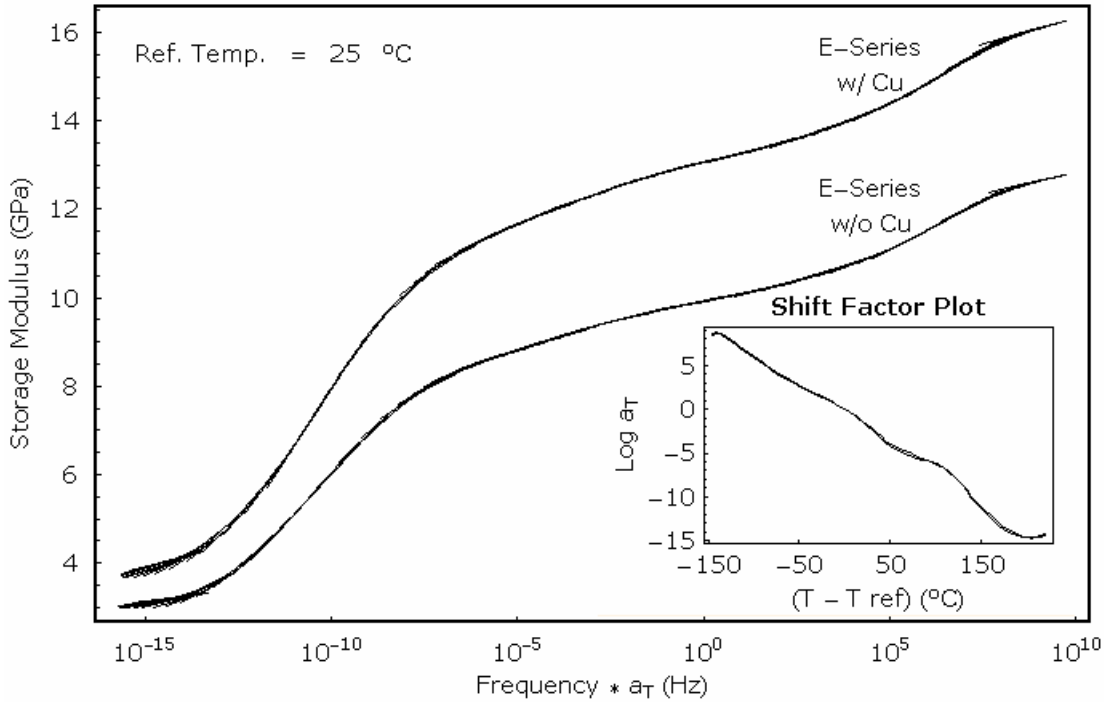


Figure 27: TTSP Master Curves for E-Series Samples w/ and w/o Cu

Having these master curves of modulus versus frequency, we next desired to derive a relationship between the DMA oscillation frequency and the strain rate of our DCB specimens. The strain rate for a DMA dual cantilever beam specimen may be readily estimated via its proportionality to the time rate of change of the beam’s curvature, which is sinusoidally perturbed. However, obtaining the time rate of change of curvature—and thus strain rate—of the falling wedge test’s double cantilever beam specimen is rather complicated. Another method is therefore used here to estimate the viscoelastic behavior.

The following method was used to estimate the modulus of our DCB specimens during test. First, it is understood that the DMA's dual cantilever beam specimens may each be considered as four individual cantilevers. Therefore, a single cantilever may be considered, having a length of $35 \text{ mm}/4$, or $L = 8.75 \text{ mm}$ (.34 in.) and a maximum deflection of $30 \text{ }\mu\text{m}/2$, or $\delta = 15 \text{ }\mu\text{m}$ (.59 mils). The maximum ratio of $\delta/L = 1.7 * 10^{-3}$ is obtained in $1/4$ of a loading period, so that

$$\frac{d}{dt} \left(\frac{\delta}{L} \right) = 4f(1.7 * 10^{-3}) \quad \text{Equation 6}$$

where f is the DMA oscillation frequency. The time rate of change of δ/L for the E-Series DCB specimens of the falling wedge test was empirically found to be approximately 11.5. This value was then substituted into Equation 6 to obtain an effective oscillation frequency of 1.7 kHz. Using this frequency value in conjunction with Figure 27, the expected range of moduli for E-Series DCB specimens fractured at the reference temperature of $25 \text{ }^\circ\text{C}$ using the falling wedge test is $10.2 - 13.4 \text{ GPa}$ ($1.48 - 1.94 \text{ Mpsi}$), where values corresponding to other temperatures may be found with use of the appropriate shift factors.

4.3.3 Quasi-static DCB

Quasi-static DCB tests were conducted using an Instron, Model 4505 universal testing machine. Small pneumatic grips were used to hold the hinges of each DCB specimen under displacement-controlled loading applied according to ASTM D 3433. Additionally, a string and pulley system was used to support the weight of the extended beam and maintain its horizontal position during test, as shown in Figure 28. A compliance method was used to determine the critical strain energy release rate of the bond under a loading rate of 10^{-4} m/s as given by

$$G_c = \frac{9\delta^2 EI_{eff}}{4w(a+x)^4}, \quad \text{Equation 7}$$

where EI_{eff} and x are both obtained from a plot of the cube root of compliance versus cracklength, as given following their graphic depiction in Figure 29.

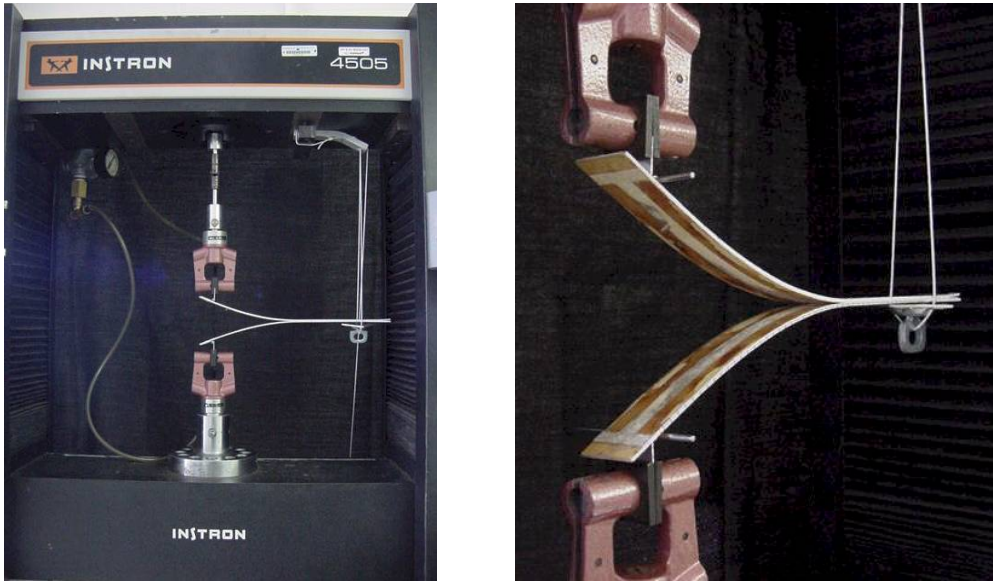


Figure 28: Quasi-static DCB Setup

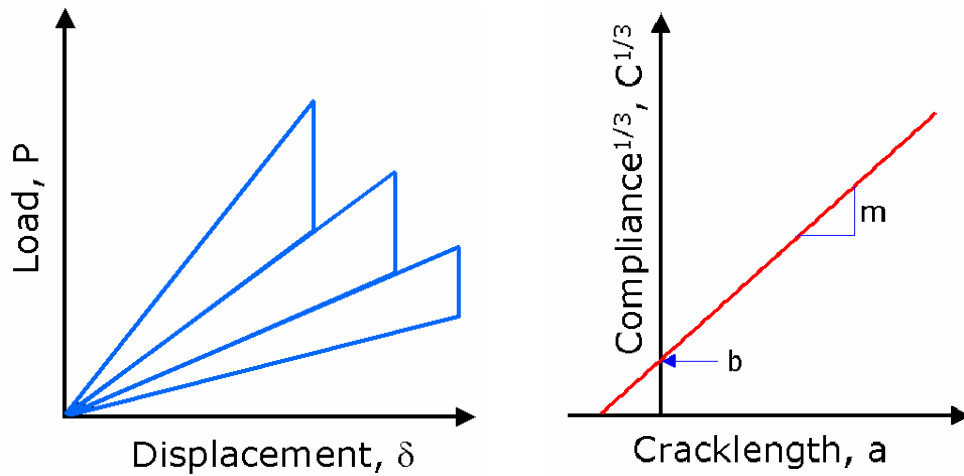


Figure 29: Idealized DCB Load Trace and Reference Plot

$$EI_{eff} = \frac{2}{3m} , \text{ and} \quad \text{Equation 8}$$

$$x = \frac{b}{m} . \quad \text{Equation 9}$$

In addition to testing DCB specimens that were kept at room temperature and humidity prior to testing, quasi-static DCB tests were also performed on specimens that were pre-conditioned at 80 °C (175 °F) and 80 % relative humidity (RH) as well as on specimens conditioned at 80 °C and near 0 %RH. These specimens were kept under respective conditions for 7 months by storing them in an oven in glass tubes containing either a potassium chlorate solution (to maintain 80 % RH at 80 °C) or a desiccant, respectively.

A typical example of the raw data from a quasi-static DCB test is given in Figure 30. A significant amount of plastic deformation is evident, whereas the opening displacement at zero load does not return to zero displacement as the number of cycles increases. This could also be a result of debris in the bondline. Either way, an estimation of this effect was made with use of a fractured specimen. The opening displacement was held closed at various intervals of the cracklength and the overall opening displacement was measured with a ruler. This result is shown in Figure 31. After subtracting this behavior from the original data, a more idealized loading diagram was obtained (See Figure 32.). This modified data was then analyzed according to the previously presented theory.

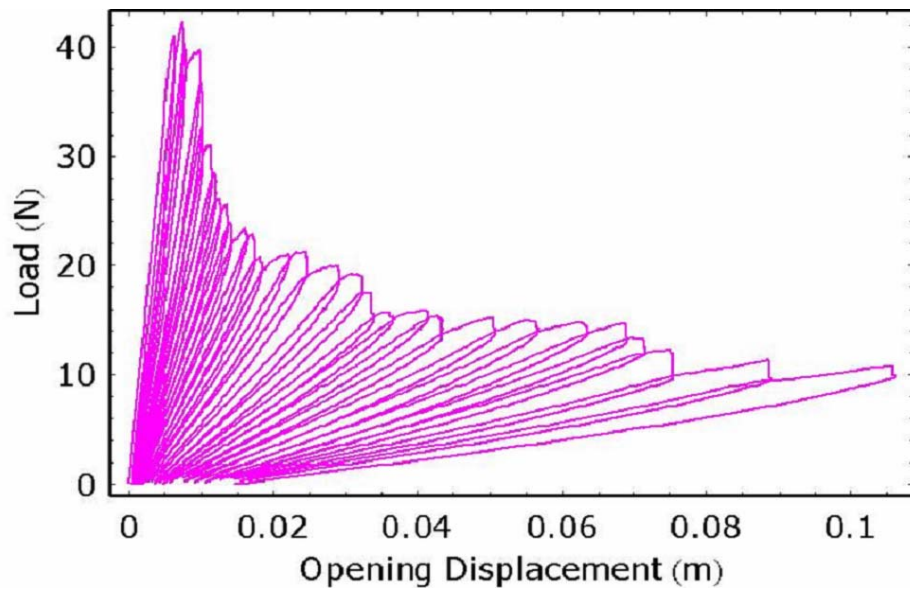


Figure 30: Typical Quasi-static DCB Data with Evident Plastic Deformation

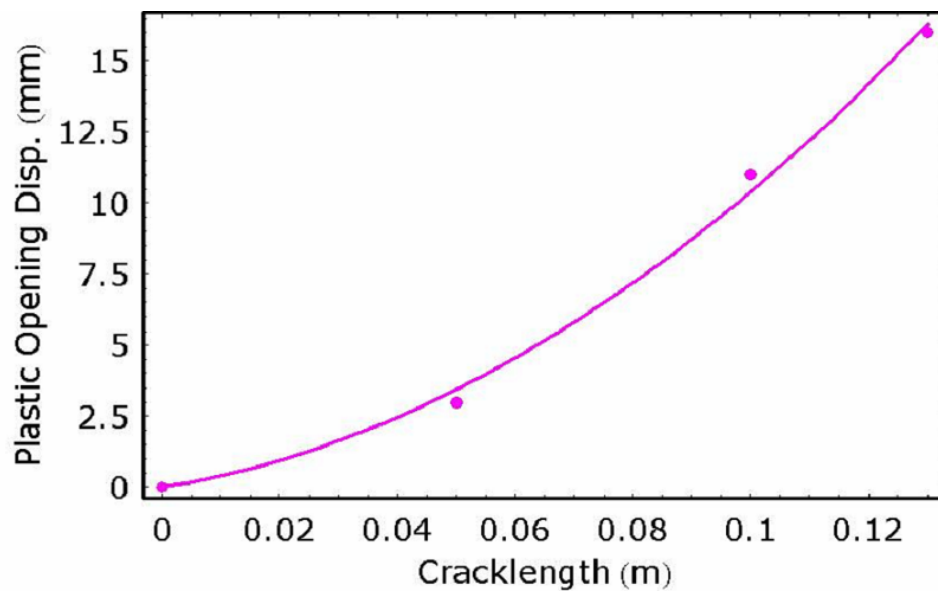


Figure 31: Estimation of Plastic Deformation in DCB Test

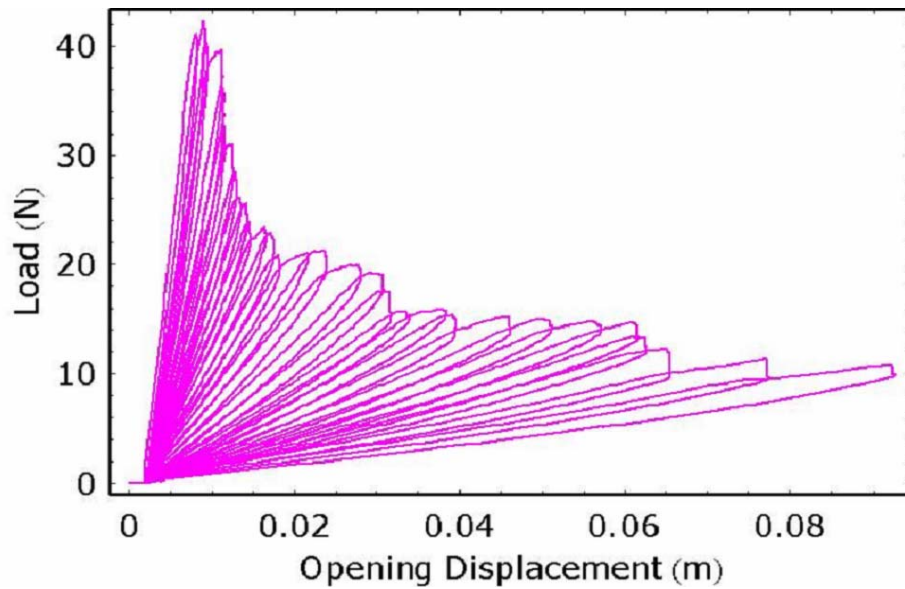


Figure 32: Quasi-static DCB Data After Subtraction of Estimated Plasticity

4.4 Results and Discussion

Double cantilever beam specimens were made corresponding to four material systems, as described in the previous section. Three to five specimens were then assigned from each material group to test at any given temperature. Falling wedge tests conducted on Materials 1, 2, and 3 had loci of failure between the copper strips of the two bonded beams, and thus either at the copper/solder interface or within the solder entirely. This result was not expected, because this copper/solder bond was presumed to be less subject to fracture than the copper/epoxy bonds that are under consideration here. Only Material 4, E-Series Thermount, yielded a consistent locus of failure within the epoxy. There were no failures that appeared to be at the interface of the copper and epoxy, as is the case during peel tests of the same material systems.

Falling wedge tests were conducted on E-Series (Material 4) specimens at temperatures of -75, 25, and 125 °C (-103, 77, and 257 °F). Surface analyses were then conducted on some of these specimens, the results of which are included in the appendices. During the data analysis stage after the fracture testing and surface analyses were completed, it was discovered that an integral piece of data was missing from each falling wedge test specimen (a distance measurement from the loading pins—which were not visible in the recorded images—to a reference mark on the specimens that was visible in the recorded images). This information was easily salvaged from those specimens still intact. Statistical accuracy in this final report, however, has been compromised. And the reader is thus cautioned to weigh the following results accordingly. Specifically, the following plot of the strain energy release rate versus temperature in Figure 33 was obtained from the results of 3 specimens fractured at -75 °C and 1 specimen tested at each 25, and 125 °C. One could rationalize, then, that the falling wedge test values at and above ambient may be outliers to the mean, thus rendering the shape and/or trend of the curve fit inaccurate.

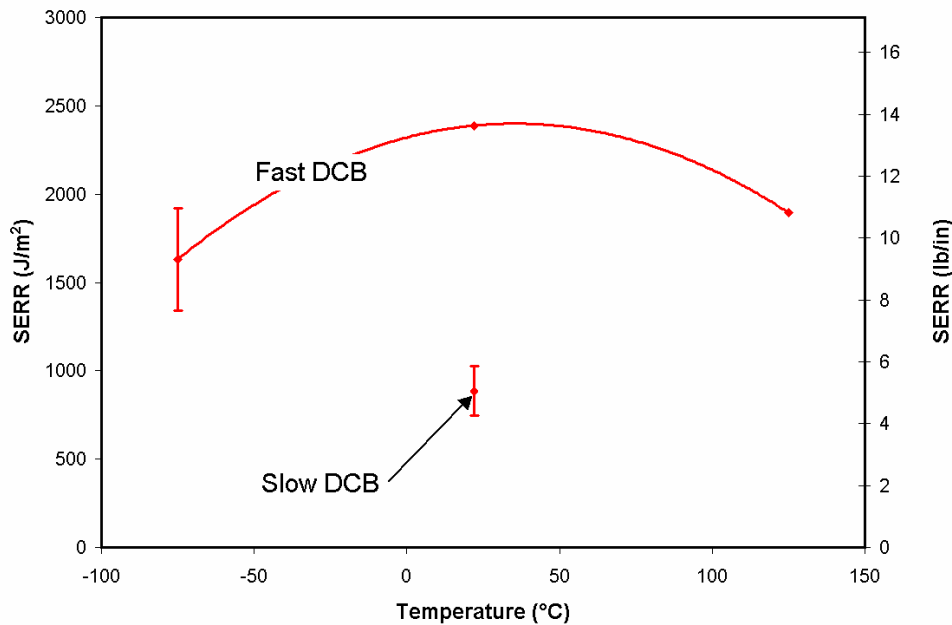


Figure 33: Falling Wedge and Quasi-static DCB Results

Results of quasi-static DCB testing of E-Series Thermount under ambient conditions are also given in Figure 33. The difference in the rate of fracture between the “fast” and “slow” tests was approximately 3 orders of magnitude (from 10^{-4} m/s to 1 m/s).

4.5 Conclusions

The objective of this study was to determine the strain energy release rates of certain copper/epoxy bonds using a falling wedge test. We then wanted to compare the SERR values obtained at high rates of test to those obtained using the quasi-static DCB test method of ASTM D 3433. Specimens from four material systems were analyzed, and the fracture energies measured for quasi-static rates of test were found to be consistent with those measured using quasi-static 90° peel tests. For slow rates of test, the measured fracture energies of the four material systems are usually related as follows: Material 1 < Material 2 < Material 3 < Material 4 (See Section 3.4.1.). Thus Material 1 usually has the lowest fracture energy. Consequently,

falling wedge testing showed that only Material 1 had a locus of failure within the printed circuit board laminate. Each of the other three material systems debonded either between the copper and the solder or within the solder entirely. This might suggest that under the circumstances of the test, the SERR of the copper/epoxy bond was greater than that of the solder/copper bond for Materials 2, 3, and 4. Unfortunately, SERR values were not obtained for the latter three material systems due to their unexpected loci of failure. The apparent SERR for Material 1 was found, however, and these temperature dependent values were higher than those measured during quasi-static testing by a factor of between 2 and 4.

Chapter 5. Results and Conclusions

The loop peel test has been successfully used to determine the apparent critical strain energy release rate (SERR) of peel specimens for low velocity impact conditions (5 m/s). Four copper/epoxy material systems common to the electronics industry were analyzed using standard quasi-static 90° peel tests and loop peel tests, and certain results were consistent for each of these materials. This included a general trend of decreasing peel energy with increasing temperature, and decreasing peel energy with an increase in effective moisture content.

The amount of energy consumed in plastically deforming the copper film peeled from the printed circuit board laminates was independent of temperature but dependent on test method. The greater amount of energy consumed in plastically deforming the copper during the loop peel tests is attributed to the bigger peel angles subtended during fracture. This energy was independent of the material system and thus independent of the SERR, but dependent upon the geometry of the test. Since the SERR for these loop peel tests was determined for the limiting case, as the peel angle approached 90°, the SERR should be equivalent to that measured by way of a standard, 90° peel test at an equivalent velocity.

Oscillations were observed in the data of the loop peel tests. Vibrational analyses were then conducted on the data as well as the rigging used to conduct these tests, and the empirical results were verified with vibrations theory. The oscillations observed in the loop peel test data were consistent for each of the material systems tested, and the dominant frequency of those oscillations increased with time. This dominant frequency is unrelated to vibrations transverse to the loading axis, but it is close to the natural axial frequency of the system. The increase in the

dominant frequency with time may then be attributed to the stiffening of the effective spring constant of the loop as debonding progresses.

Values of the apparent critical strain energy release rate are based on the measured force versus time, without any filtering of that signal. Axial vibrations due to stretching of the load train suggest the need to account for stored energy in calculations of the SERR. All of the oscillations in the force versus time signals, however, decreased with time as the force converged to its steady state value. And the stored energy for the limiting case is negligible.

A high-speed camera system was utilized to precisely determine the change in displacement with time. Then, using a loading mass with a weight comparable to the force required to maintain quasi-static debonding, the displacement versus time signal was almost linear. Therefore, by providing a significant amount of potential energy by way of the falling mass, the amount of energy consumed by the fracture and related events will not be noticeable in the displacement signal during the fracture event. Consequently, if the speed of the mass at the time of impact is known, the slope for a linear displacement versus time signal may be thus defined. Then, by assuming that this displacement increases from zero at a time near the onset of the force, the SERR may be estimated without the need of the high-speed camera.

A falling wedge test has also been used to determine an apparent strain energy release rate for the above material systems at impact velocities. The SERR values obtained at high rates of test were compared to those obtained using the quasi-static DCB test method of ASTM D 3433. Specimens from the four material systems were analyzed, and the fracture energies measured for quasi-static rates of test were consistent with those measured using quasi-static 90° peel tests.

For slow rates of test, the measured fracture energies of the four material systems are usually related as follows: Material 1 < Material 2 < Material 3 < Material 4. Thus Material 1 usually has the lowest fracture energy. Consequently, falling wedge testing showed that only Material 1 had a locus of failure within the printed circuit board laminate. Each of the other three material systems debonded either between the copper and the solder or within the solder entirely. This might suggest that under the circumstances of the test, the SERR of the copper/epoxy bond was greater than that of the solder/copper bond for Materials 2, 3, and 4. Unfortunately, SERR values were not obtained for the latter three material systems due to their unexpected loci of failure. The apparent SERR for Material 1 was found, however, and these temperature dependent values were higher than those measured during quasi-static testing by a factor of between 2 and 4.

Four testing methods were thus employed to analyze the four types of printed circuit boards. The test methods included two types of peel tests and two types of DCB tests, so as to encompass both slow and high rates of test. Furthermore, each peel test produced near interfacial failure and each evaluated DCB test produced totally cohesive failure (within the printed circuit board laminates). If we assume that the measured SERR values are accurate for all four test methods, then the following conclusions might be drawn: At slow rates of test, the fracture energies associated with adhesive (near interfacial) and cohesive (within the laminate) fracture are nearly the same, but at high rates of test, cohesive fracture energies are considerably higher than adhesive fracture energies, where all fracture energies measured at high rates of test are greater than corresponding values at quasi-static rates of test. There is therefore a greater increase in SERR when shifting from cohesive quasi-static to cohesive impact fracture speeds than when shifting from adhesive quasi-static to adhesive impact fracture speeds. One possible

explanation for this behavior might relate to fiber pullout during cohesive fracture. Analysis of cohesive fracture surfaces has shown that the reinforcing fibers of the printed circuit boards are exposed on both sides of the fracture plane and protrude from the epoxy matrix. If the fibers strain relatively slowly under imposed stress, it is possible that this is not perceived under quasi-static rates of test. The fibers could potentially neck down and pull out of their local cavities. Under high rates of test, it would then be possible that these same fibers would not be able to stretch and neck down in time. They would thus remain stiff and potentially cause a greater disturbance to the surrounding epoxy matrix upon fracture.

Surface analyses were conducted on the materials tested, the complete details of which are included in the appendix. This testing included analyses of the fracture surfaces for quasi-static, 90° peel tests. For each material system and for each test temperature (-15 °C, 30 °C, and 90 °C), it was discovered that fracture occurs within the composite layer, yet very near the surface to which the copper was bonded. Evidence for this included x-ray photoelectron spectroscopy (XPS) results showing no copper on either of the debonded surfaces.

5.1 Evaluation

The research presented here was conducted in the pursuit of a Master's degree in Engineering Mechanics. When the author began this course, he was not aware of the results that would eventually be obtained or the path that would be taken in attaining that end. This should be obvious to some extent, wherein any true research is a journey into the unknown. However, were these tasks to be completed again, the author would undoubtedly do some things differently. A few examples include:

- More specimens would be tested under more conditions. Statistical analyses would be conducted beforehand in the “design of experiment” stage, and afterward to strengthen the interpretation of the data.
- Loop peel tests would be conducted under quasi-static conditions. No data was obtained from the loop peel test specimen at the quasi-static rates. This would lend credibility to the test method.
- More data would be gathered to describe the time and temperature effects on copper, and
- Tests would be conducted to further analyze and explain the decreasing peel energy with increasing temperature trend.

Chapter 6. References

1. Poynting, J. H. & Thomson, J. J. in *A Text-Book of Physics* 137 (Charles Griffin and Co., London, 1909).
2. <http://thales.cica.es/rd/Recursos/rd99/ed99-0289-02/biografias/cfgauss.html>.
3. Jones, J. B. & Dugan, R. E. in *Engineering Thermodynamics* 191-193 (Prentice Hall, Inc., 1996).
4. Griffith, A. A. The Phenomena of Rupture and Flow in Solids. *Philosophical Transactions of the Royal Society of London. Series A* **221**, 163-198 (1921).
5. Elliott, H. A. An Analysis of the Conditions for Rupture Due to Griffith Cracks. *Proc. Phys. Soc. London* **59**, 208-223 (1947).
6. Orowan, E. Fracture and Strength of Solids. *Reports on Progress in Physics* **12**, 185-232 (1949).
7. Rivlin, R. S. & Thomas, A. G. Rupture of Rubber. I. Characteristic Energy for Tearing. *Journal of Polymer Science* **10**, 291-318 (1953).
8. Irwin, G. R. Analysis of Stresses and Strains Near the End of a Crack Traversing a Plate. *Journal of Applied Mechanics* **24**, 361-364 (1957).
9. Berry, J. P. Fracture Processes in Polymeric Materials. I. The Surface Energy of Poly(methyl Methacrylate). *Journal of Polymer Science* **50**, 107-115 (1961).
10. Rice, J. R. & Sih, G. C. Plane Problems of Cracks in Dissimilar Media. *Transactions of the ASME*, 418-423 (1965).
11. Sawyer, S. G. & Anderson, R. B. Collocated Interfacial Stress Intensity Factors for Finite Bi-Material Plates. *Engineering Fracture Mechanics* **4**, 605-616 (1972).
12. Ripling, E. J. & Mostovoy, S. Fracture Mechanics: A Tool for Evaluating Structural Adhesives. *Journal of Adhesion* **3**, 107-123 (1971).
13. Piva, A. & Viola, E. Biaxial Load Effects on a Crack Between Dissimilar Media. *Engineering Fracture Mechanics* **13**, 143-174 (1980).
14. Williams, M. L. in *Adhesive Joints: Formation, Characteristics, & Testing* (ed. Mittal, K. L.) 703-737 (Plenum Press, New York, 1984).
15. Liechti, K. M. in *Engineered Materials Handbook* 335-348 (1987).
16. Kanninen, M. F. A Dynamic Analysis of Unstable Crack Propagation and Arrest in the DCB Test Specimen. *International Journal of Fracture* **10**, 415-430 (1974).
17. Wang, S. S., Mandell, J. F. & McGarry, F. J. An Analysis of the Crack Tip Stress Field in DCB Adhesive Fracture Specimens. *International Journal of Fracture* **14**, 39-58 (1978).
18. Williams, J. G. Large Displacement and End Block Effects in the 'DCB' Interlaminar Test in Modes I and II. *Journal of Composite Materials* **21**, 330-347 (1987).
19. Williams, J. G. On the Calculation of Energy Release Rates for Cracked Laminates. *International Journal of Fracture* **36**, 101-119 (1988).
20. Hashemi, S., Kinloch, A. J. & Williams, J. G. Corrections Needed in Double-Cantilever Beam Tests for Assessing the Interlaminar Failure of Fibre-Composites. *Journal of Materials Science Letters* **8**, 125-129 (1989).
21. Blackman, B. R. K., Dear, J. P., Kinloch, A. J. & Osiyemi, S. The Calculation of Adhesive Fracture Energies from Double-Cantilever Beam Test Specimens. *Journal of Materials Science Letters* **10**, 253-256 (1991).
22. Williams, J. G. The Fracture Mechanics of Delamination Tests. *Journal of Strain Analysis* **24**, 207-214 (1989).

23. Hashemi, S., Kinloch, A. J. & Williams, J. G. The Analysis of Interlaminar Fracture in Uniaxial Fibre-Polymer Composites. *Proceeding of the Royal Society of London. Series A, Mathematical and Physical Sciences* **427**, 173-199 (1990).
24. Charalambides, M. N. & Williams, J. G. Mode I Delamination of Angle-Ply Epoxy/Glass-Fibre Laminates Exhibiting Permanent Deformation During Fracture. *Composites Science and Technology* **50**, 187-196 (1994).
25. Lim, W. W., Hatano, Y. & Mizumachi, H. Fracture Toughness of Adhesive Joints. I. Relationship Between Strain Energy Release Rates in Three Different Fracture Modes and Adhesive Strengths. *Journal of Applied Polymer Science* **52**, 967-973 (1994).
26. Lim, W. W. & Mizumachi, H. Fracture Toughness of Adhesive Joints. III. Temperature and Rate Dependencies of Mode II Fracture Toughness and Adhesive Shear Strength. *Journal of Applied Polymer Science* **63**, 835-841 (1997).
27. Williams, M. L., Landel, R. F. & Ferry, J. D. The Temperature Dependence of Relaxation Mechanisms in Amorphous Polymers and Other Glass-forming Liquids. *Journal of the American Chemical Society* **77**, 3701-3707 (1955).
28. Blackman, B. R. K., Kinloch, A. J., Wang, Y. & Williams, J. G. The Failure of Fibre Composites and Adhesively Bonded Fibre Composites Under High Rates of Test. Part II: Mode I Loading - Dynamic Effects. *Journal of Materials Science* **31**, 4451-4466 (1996).
29. Blackman, B. R. K. et al. The Failure of Fibre Composites and Adhesively Bonded Fibre Composites Under High Rates of Test. Part I: Mode I Loading - Experimental Studies. *Journal of Materials Science* **30**, 5885-5900 (1995).
30. Blackman, B. R. K. et al. The Failure of Fibre Composites and Adhesively Bonded Fibre Composites Under High Rates of Test. Part III: Mixed-Mode I/II and Mode II Loadings. *Journal of Materials Science* **31**, 4467-4476 (1996).
31. Thouless, M. D. et al. Determining the Toughness of Plastically Deforming Joints. *Journal of Materials Science* **33**, 189-197 (1998).
32. Blackman, B. R. K. & Kinloch, A. J. *Fracture Mechanics Testing Methods for Polymers, Adhesives, and Composites* (ed. A. Pavan, D. R. M., and J.G. Williams) (Elsevier Science, Amsterdam, 2001).
33. Xu, S. & Dillard, D. A. Determining the Impact Resistance of Electrically Conductive Adhesives Using a Falling Wedge Test. *IEEE Transactions on Components and Packaging Technologies* **26**, 554-562 (2003).
34. Jacquet, P. A. Methods of studying electrodeposited metals. *IX Congr. intern. quim. pura aplicada* **2**, 428-36 (1934).
35. Spies, G. J. Peeling Test on Redux-Bonded Joints. *Aircraft Engineering* **25**, 64-70 (1953).
36. Chen, W. T. Mechanics of Film Adhesion: Elastic and Elastic-Plastic Behavior. *IBM Journal of Research and Development* **16**, 203-213 (1972).
37. Kim, K.-S. & Aravas, N. Elastoplastic Analysis of the Peel Test. *International Journal of Solids and Structures* **24**, 417-435 (1988).
38. Kinloch, A. J., Lau, C. C. & Williams, J. G. The Peeling of Flexible Laminates. *International Journal of Fracture* **66**, 45-70 (1994).
39. Moidu, A. K., Sinclair, A. N. & Spelt, J. K. Analysis of the Peel Test: Prediction of Adherent Plastic Dissipation and Extraction of Fracture Energy in Metal-to-Metal Adhesive Joints. *Journal of Testing and Evaluation* **23**, 241-253 (1995).

40. Moidu, A. K., Sinclair, A. N. & Spelt, J. K. On the Determination of Fracture Energy Using the Peel Test. *Journal of Testing and Evaluation* **26**, 247-254 (1998).
41. Ryschenkow, G. & Arribart, H. Adhesion Failure in the Stick-Slip Regime: Optical and AFM Characterizations and Mechanical Analysis. *Journal of Adhesion* **58**, 143-161 (1996).
42. Maugis, D. Subcritical Crack Growth, Surface Energy, Fracture Toughness, Stick-Slip and Embrittlement. *Journal of Materials Science* **20**, 3041-3073 (1985).
43. Barquins, M. & Ciccotti, M. On the Kinetics of Peeling of an Adhesive Tape Under a Constant Imposed Load. *International Journal of Adhesion and Adhesives* **17**, 65-68 (1997).
44. Ciccotti, M., Giogini, B. & Barquins, M. Stick-Slip in the Peeling of an Adhesive Tape: Evolution of Theoretical Model. *International Journal of Adhesion and Adhesives* **18**, 35-40 (1998).
45. Wei, Y. & Hutchinson, J. W. Interface Strength, Work of Adhesion and Plasticity in the Peel Test. *International Journal of Fracture* **93**, 315-333 (1998).
46. Ciccotti, M., Giogini, B., Vallet, D. & Barquins, M. Complex Dynamics in the Peeling of an Adhesive Tape. *International Journal of Adhesion and Adhesives* **24**, 143-151 (2004).
47. Bowditch, M. R. The Durability of Adhesive Joints in the Presence of Water. *International Journal of Adhesion and Adhesives* **16**, 73-79 (1996).
48. Orman, S. & Kerr, C. in *Aspects of Adhesion* (ed. Alner, D. J.) 64 (University of London Press, London, 1971).
49. Ma, Q., Tran, Q., Pan, C., Fujimoto, H. & Chiang, C. Polymer/Metal Interfaces in Interconnect Structures: Moisture Diffusion and Stress Corrosion Effects. *Materials Research Society Symposium Proceedings* **511**, 329-339 (1998).
50. Yu, D. Y. W. The Yield Strength of Thin Copper Films on Kapton. *Journal of Applied Physics* **95**, 2991-2997 (2004).
51. Blackman, B. R. K., Kinlock, A. J., Taylor, A. C. & Wang, Y. Impact Wedge Peel Performance of Structural Adhesives. *Journal of Materials Science* **35**, 1867-1884 (2000).

Appendix A. Design of Test Fixtures

A.1 Quasi-Static Peel Fixture

A modular fixture for conducting peel tests in an Instron or similar universal testing machine was designed. The purpose in doing so was to provide the following services:

- To create a modular design with components that could be built and added to the base system at later times and thus minimize the required up-front expense
- To allow testing over a range of peel angles, ideally from 0° to 180°
- To offer visual access/inspection of the debond from beneath the peel substrate
- To control the temperature of the peel specimen during testing

From the four views of Figure 34, the heating/cooling unit can be seen as it rotates above and away from the work piece (not shown) that would be clamped between the two-part translating stage. The heating/cooling unit is composed of an inner track to hold a tubular heat exchanger. A shield encloses the track to provide insulation from the heat exchanger. The slotted clamps of the two-part stage allow for differently sized specimens, ranging from 1 to 2 inches in width, and being less than 6 inches in length. The system is capable of achieving peel angles from 0° to just past 90° and from just below 180° to 180° with use of the heating/cooling unit. All peel angles from 0° to 180° may be achieved, however, if the heating/cooling unit is detached.

There is a pulley on one end of the fixture to smoothly guide a cable attached to the stage to the top of the Instron. As the Instron crosshead moves, the pulley system will move the stage so as to keep the location of the crack stationary and the peel angle constant (assuming there is no adherend stretching). To keep the stage from advancing under the influence of the peel force instead of the cable attached to the top of the Instron, a “constant-force” spring (like used in a tape measure) is located below the heating/cooling unit, connecting the frame of the fixture to the two halves of the stage.

Stacy Coulthard and Rachel Roop built the base unit of the peel fixture (without heat exchanger). An independent (not the one described above) heat exchanger was then mounted on top of the two-part stage and used for all of the quasi-static 90° peel testing that I conducted during the course of this research.

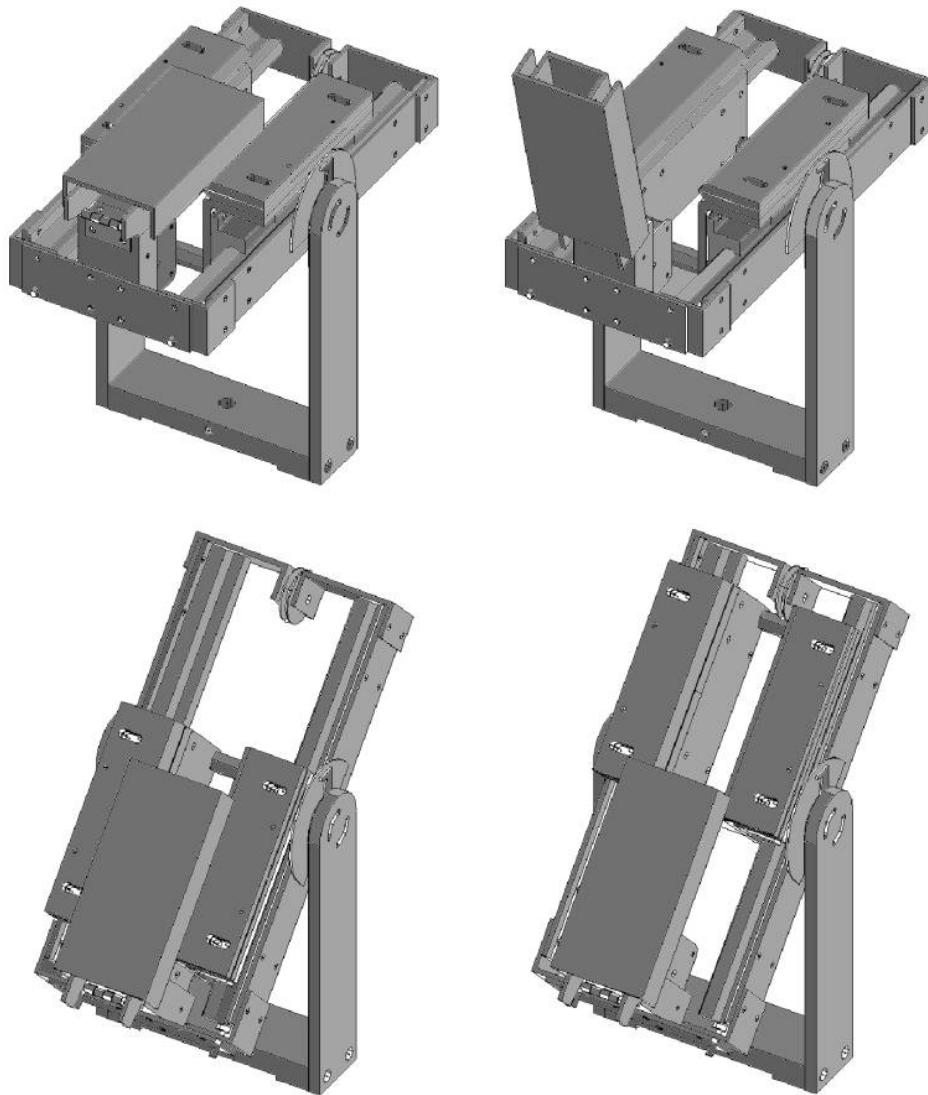


Figure 34: Quasi-Static Peel Fixture

A.2 Climbing Drum

The climbing drum described in the ASTM standard (ASTM D 1781-98) is a heavy steel object, and clearly not suitable for the impact testing described in Section B.3. For this reason, the drum described in the standard was used only as a reference when designing one more applicable. Polycarbonate was used to reduce the weight, and to offer impact resistance. Then the core was removed to further reduce weight in addition to the translational and rotational moments of

inertia. Less a few minor changes, the mechanical drawing in Figure 35 below gives the details according to its making.

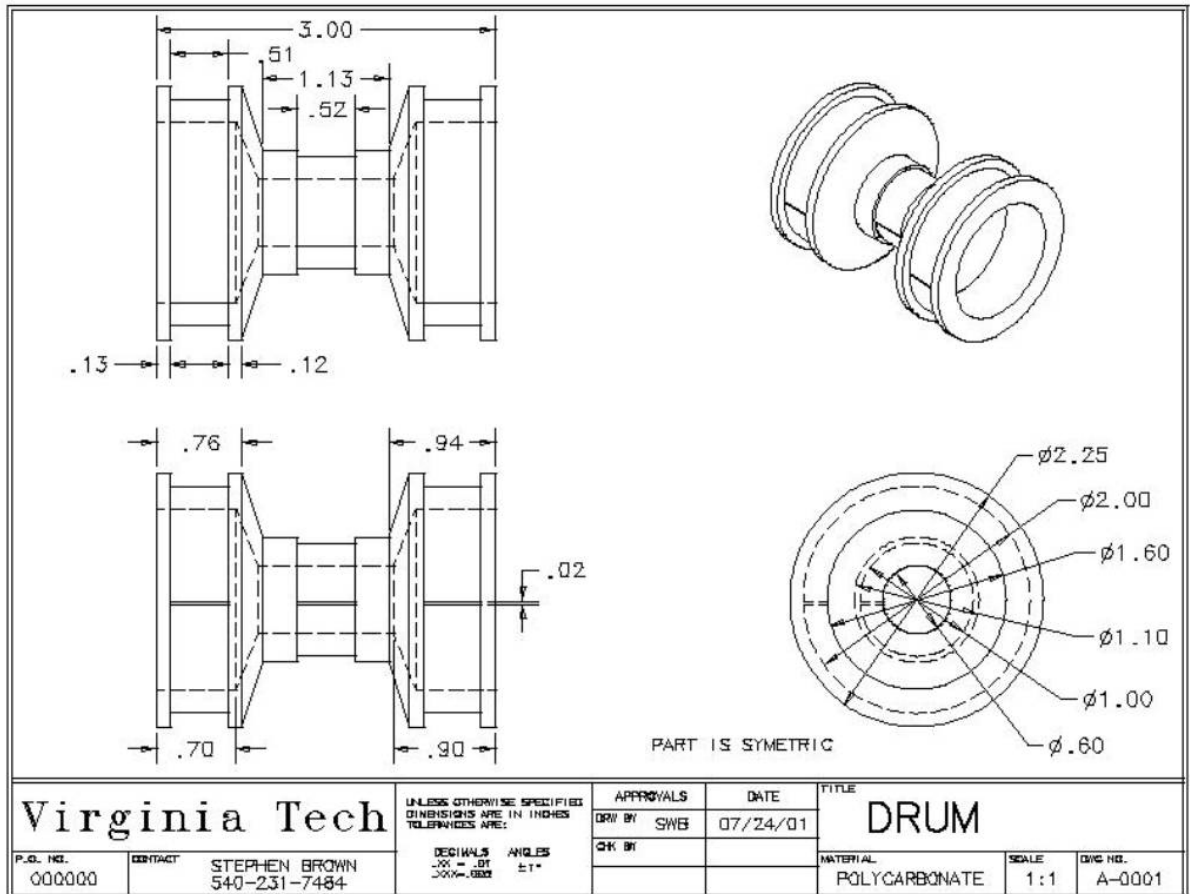


Figure 35: Climbing Drum

The middle section of the drum has a nominal diameter of 1 inch, and the larger diameter end-sections are nominally 2 inches. Within the inner, smaller portion is a recess to accommodate the thickness of the flexible adherend (copper film, in this case) as it rolls up. Also, each of the larger-diameter sections has a recess to guide a loading strap. Slots are then milled across the breadth of each recess to aid attachment of the respective loading strap or adherend.

Appendix B. Preliminary Impact Tests

B.1 Asymmetric 90° Impact Peel Test

The 90° peel test has been accepted as an appropriate test method to determine the apparent critical strain energy release rate for bonds between stiff and flexible adherends, but its use has been limited to quasi-static fracture speeds. A similar test method was therefore first considered when seeking fracture energies at impact speeds, intending to allow the direct comparison of impact results to those obtained using the former method at quasi-static fracture speeds. A falling mass was first used in an attempt to provide an impact (or impulsive load) to an inverted 90° peel specimen.

Specimens were prepared according to the description in Section 3.3 with debonds initiated on one end of the printed circuit boards (PCBs). They were then fixed to the underside of a rigid surface by compressing the exposed portion of the PCB, not covered by copper, to the rigid surface with an aluminum bar of 25 x 6 mm (1 x .25 in.) cross-section and two C-clamps as shown in Figure 36.

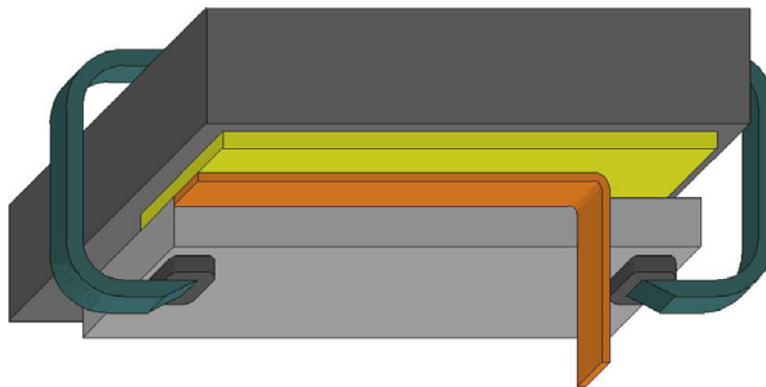


Figure 36: 90° Impact Peel Setup

To impart an impulsive load to the free end of the copper without creating stress concentrations at the point of loading and tearing the copper, the copper strip was wrapped around and bonded

to a 1" long by 1/4" in diameter steel dowel pin. A steel clip was then formed to grip the ends of the dowel and provide a central loop for loading. Finally, a mass was attached to one end of a flexible cable, the other end being connected to the steel clip. This is shown in Figure 37 below.



Figure 37: Impact Loading Mechanism for 90° Peel Tests

- Masses from 100 to 1000 grams were connected to a 4-foot long tether and dropped by hand to impact and debond the full length of copper. After this initial phase of testing, the following qualitative results were determined:
- The forward-facing edge of the aluminum bar (See Figure 36) should be capped with a finely graduated measure, as a better basis for determining debond distance was needed.
- A controllable drop height was needed. Dropping the mass by hand provided little means by which the height could be kept consistent.
- A triggering device was needed to initiate recording at the time of release, because the camera is only able to record at high speed (up to 12,000 fps) for about one second.

- Better understanding of the image analysis software (LabVIEW Vision Builder) was needed. Images were manually analyzed to retrieve quantitative results.
- A closer view of the debonding region was desired. Since both the specimen and the camera were mounted on non-moving platforms, the entire length of the printed wiring board had to be within the field of view of the camera. The resolution was therefore limited.

Using a high-speed camera, images were recorded that captured the cracklength and peel angle at given times during the fracture event. These images were then individually examined to obtain measurements of the displacement and peel angle. Typical results are shown in Figure 38.

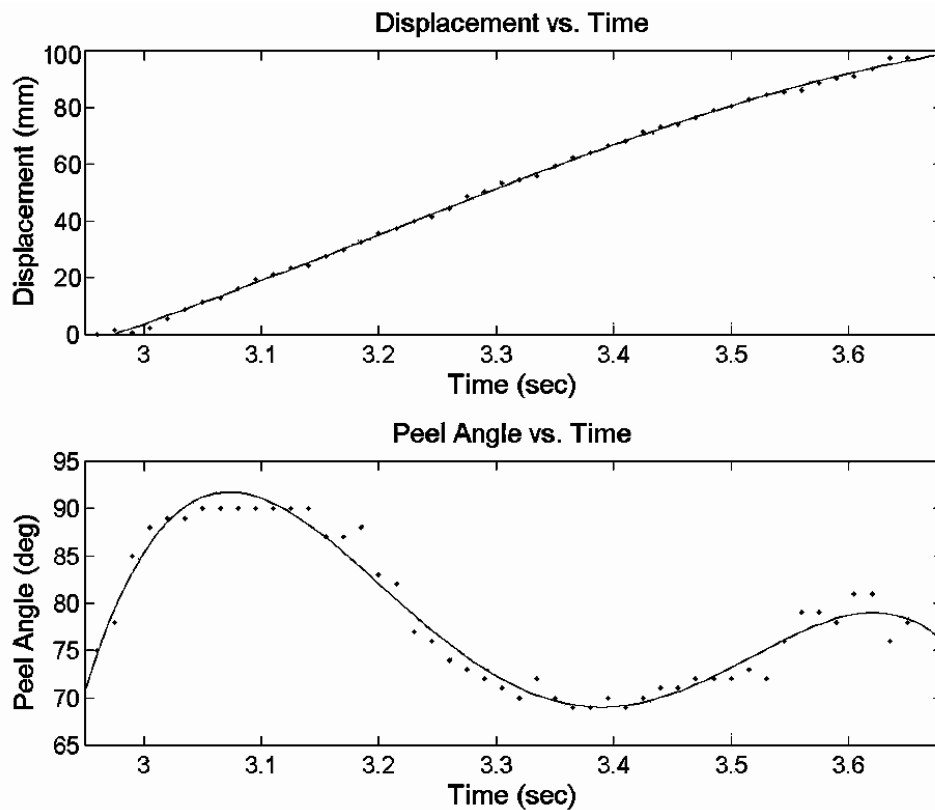


Figure 38: Typical Results of 90° Impact Peel Test

The plot of displacement (or cracklength) versus time, above, is smooth and consistent with our expectations. Since the slope and thus velocity are seen to decrease with time, it may be understood that the weight of the mass is less than the force required to cause debonding. Conversely, a large mass would be minimally affected by the energy consumed in debonding the copper, and the expected displacement versus time plot should resemble that of an unhindered falling mass.

The plot of peel angle versus time, however, was not consistent with our expectations, since the peel angle does not remain at 90° . For this particular test, the initial peel angle (at that time corresponding to zero displacement) is approximately 70° as a result of dropping the mass out of plumb with the initial crack tip. Had the mass been dropped directly below the cracktip to yield an initial 90° peel angle, the behavior to follow would still resemble that shown above. This is due to the asymmetric nature of the test. Since there is an amount of inertia associated with the mass (not to mention the dowel pin, clip, and tether), it's preferred decent path is vertical. This path is only altered after the crack has grown to sufficient length (horizontally) and the after the peel angle and corresponding tension in the cable are such that they may pull the mass back toward a 90° peel angle.

Although using a very long tether may reduce the problem of a varying peel angle, the same introduces other variables of concern that discouraged further pursuit of the method as described.

B.2 180° Impact Peel Test

A 180° impact peel test was considered next after facing obstacles with the asymmetric 90° impact peel test. Specimens were affixed vertically against a rigid support, with the free end of

the copper on top so that they could be loaded with the same rigging as used with the 90° impact peel test (See Figure 39). Unfortunately, the copper strip tore without debonding from the printed circuit board laminate for the majority of the 180° impact peel tests conducted. This tearing was attributed somewhat to the increased plastic deformation and weakening of the copper at the cracktip.

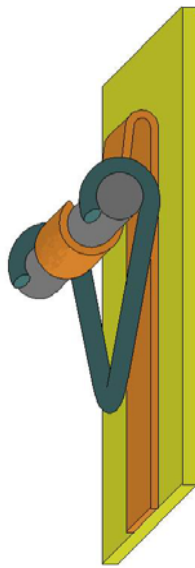


Figure 39: 180° Impact Peel Setup

B.3 Climbing Drum Test

The climbing drum test is an ASTM standard (ASTM D 1781-98) that has been used for debonding the face-sheets from sandwich panels. A similar concept has been applied here, in which a dumbbell-shaped drum was made to peel a flexible adherend at an approximately 0° peel angle from a relatively stiff adherend. The purpose for choosing this method was two-fold. First, all moving masses remain in a vertical line, such that the dynamic “swinging” affects observed in the 90° impact peel testing would be minimal. Second, by approaching (or

attempting to approach) a 0° peel angle, the increased plastic deformation and weakening of the copper at the cracktip observed in the 180° impact peel tests would be minimal.

After securing a PCB specimen to a rigid, vertical support, such that its free end of copper (for which debonding was initiated prior to testing) was located at the bottom, that free end of copper was wrapped around and bonded to the smaller diameter of the drum. Loading straps were fixed to and wrapped around the larger diameters of the drum such that when the straps were pulled down, the induced rotation of the drum would cause it to climb up the vertically mounted specimen, debonding the copper at the same time. The climbing drum setup is shown below.

To provide an impact load to the loading straps of the climbing drum in a more consistent manner than obtained by dropping a mass by hand that was connected with a flexible cord to the straps, a rod was utilized with a translating mass. Use of linear bearings inside the mass minimized friction during its fall.

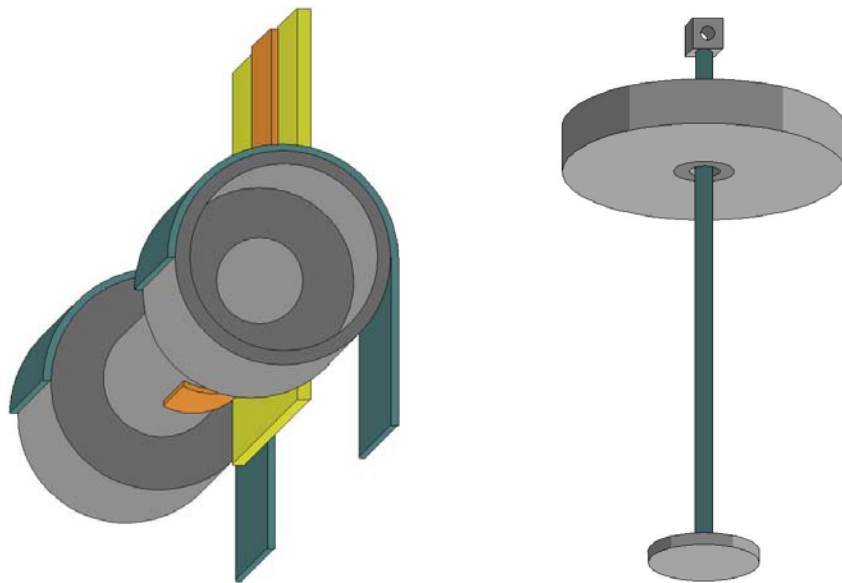


Figure 40: Climbing Drum Setup

The apparent critical strain energy release rate was sought with use of the climbing drum method. As shown in Figure 41, a third mass—the mass of the drum, m_D —must be considered when determining the change in energy to calculate G_c . Only the loading mass, m_L , and the mass of the rigging, m_R , where necessary to compute the change in energy during the 90° and 180° impact peel tests.

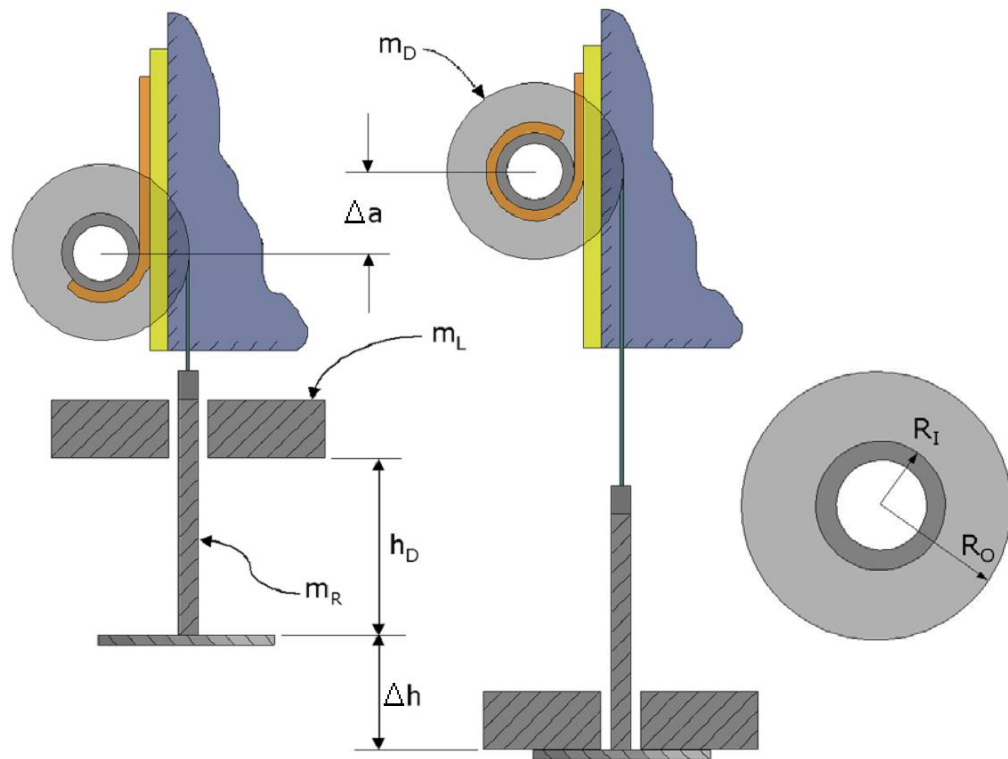


Figure 41: Variables of Climbing Drum Test

The apparent critical strain energy release rate, G_c , for debonds associated with the climbing drum test may be computed as the change in energy of the system divided by the corresponding area of the bond that was fractured.

$$G_c = \frac{\left(\frac{1}{2} m_L \cdot v_o^2\right) + ((m_L + m_R)g \cdot \Delta h) - (m_D \cdot g \cdot \Delta a)}{w \cdot \Delta a}$$

$$\left(\frac{1}{2} m_L \cdot v_o^2\right) = m_L \cdot g \cdot h_D$$

Equation 10

$$\Delta h / \Delta a = R_o / R_i$$

The climbing drum method described above was not, however, as well suited to our needs as expected. The conditions motivating its use were met, however a more serious consequence was overlooked. Although the drum was made lightweight, it still possessed too much inertia to be accelerated to impact speeds without first yielding the copper film in tension. As a result, the copper tended to break without debonding when impacted. Furthermore, the expected 0° peel angle was not realized, in that the inner diameter of the drum tended to slip along the PWB/copper surface such that the peel angle varied from near-0° to near-90°. Only Material #2 was tested using the climbing drum method, and the average apparent critical strain energy release rate determined from the tests conducted was 2200 J/m² with a standard deviation of 130 J/m². These values are a factor of two greater than those measured using quasi-static 90° peel tests.

Appendix C. Mechanical Properties of Materials

A Dynamic Mechanical Analyzer (DMA) made by TA Instruments was used to estimate the storage modulus of the printed circuit boards. Dual cantilever beam specimens were made from each PCB material, both without copper bonded to one side and with copper bonded to one side (covering the entire side). These cases were chosen to represent the limits of the expected range of moduli during an actual test. The dual cantilever beam specimens had dimensions of approximately 9 x 55 x 1.63 mm (0.35 x 2.17 x 0.064 in.). Their effective lengths were 35 mm (1.38 in.), as determined by the DMA loading fixture. These specimens were cyclically loaded at frequencies between 0.1 and 100 Hz for temperatures between -120 °C and 250 °C (-185 °F and 480 °F) using an oscillation amplitude of 30.0 µm (1.18 mil). Only frequency data of 0.1, 1, and 10 Hz were used however, because there was reason to believe that the 100 Hz signal may have approached a natural frequency of the test frame. Master curves were produced of the storage modulus versus oscillation frequency for each case, along with their corresponding shift factor plots. DMA data was not found for N-Series Thermount specimens (Material #2). The storage modulus for Material #2 was expected to fall between those moduli found for Material #1 (E-Series Thermount) and Material #3 (Thermount RT). Since the values obtained for Materials #1 and #3 were nearly the same for the highest frequencies on their master curves, the modulus of Material #2 could be estimated with precision. Data was obtained for Material #4 (FR4) without copper, but this data was corrupted.

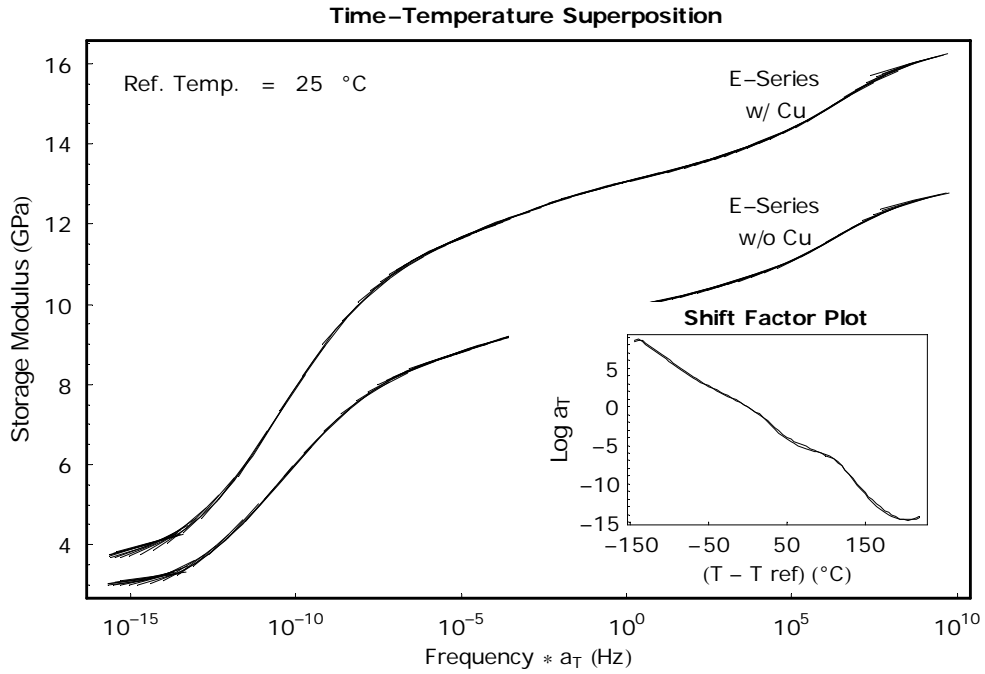


Figure 42: Master curve of storage modulus versus frequency for Material #1

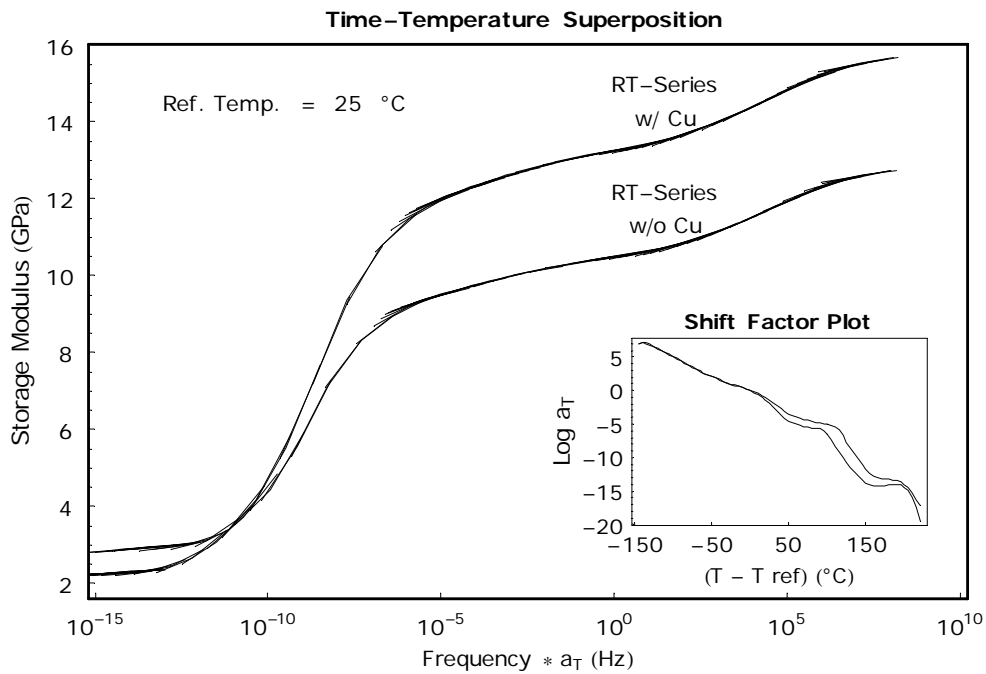


Figure 43: Master curve of storage modulus versus frequency for Material #3

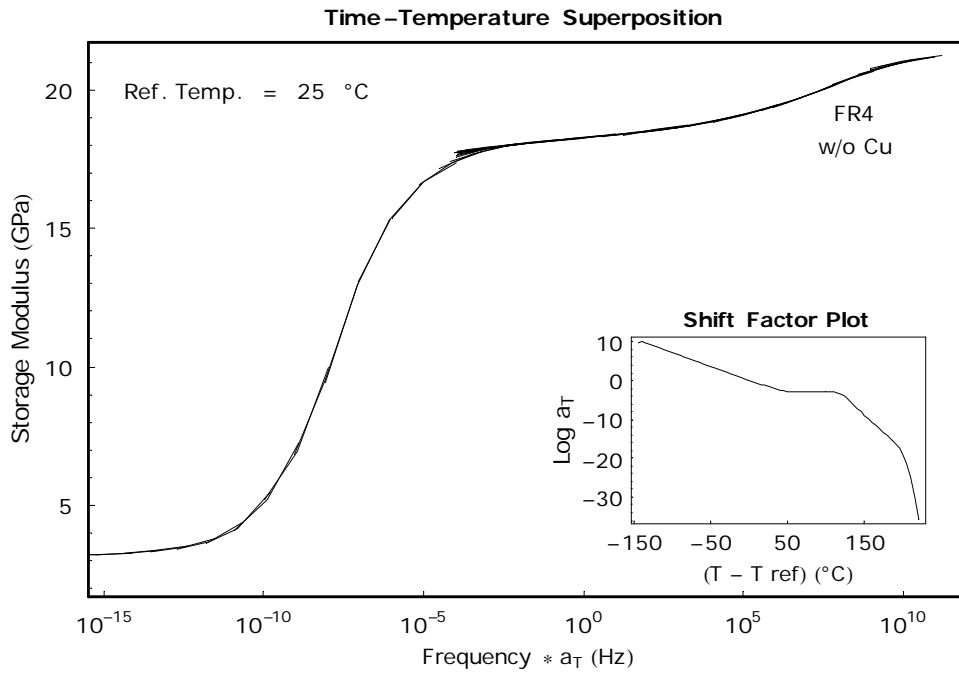


Figure 44: Master curve of storage modulus versus frequency for Material #4

Appendix D. Mathematica Programs

During the course of these studies, various programs were written to collect and analyze data.

The primary languages used include MATLAB, LabVIEW, and *Mathematica*. Certain programs written in *Mathematica* (of Wolfram Research) that may be of interest to the reader are included below.

D.1 Analysis of Loop Peel Tests Using Fast Fourier Transformations

The force versus time signals recorded with each loop peel test showed periodic behavior that was analyzed with Fast Fourier Transformations (FFT's). It was discovered, however, that the dominant frequencies during each test were not constant in time. (This phenomenon was readily attributed to the nonlinearity of the system.) *Mathematica* code was therefore written to determine the dominant frequencies as well as their variability. This code is included below, preceded by a brief description of its development.

Sample FFT Analysis

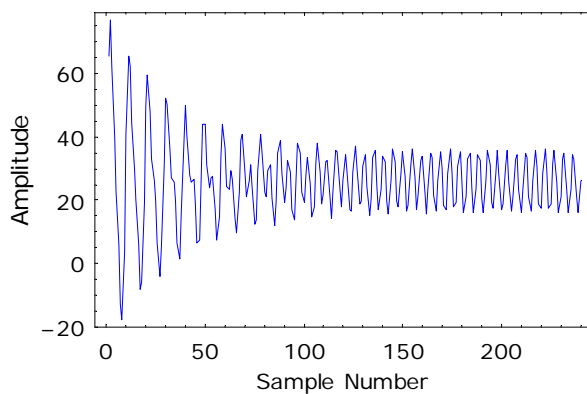
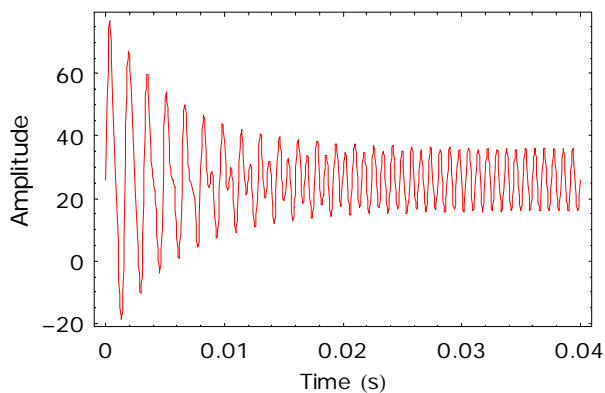
I will first create a mock signal and run a Fast Fourier Transform (FFT) on it. Then I will try to re-create the original signal from the FFT results to verify that I correctly understand the process.

```
n = 240;  
(*Number of samples in waveform to be analyzed-- Must be even for mock analysis*)  
fs = 6000; (*Sampling frequency*)  
 $\Delta t = 1/fs$ ; (*Time interval between samples*)  
T = n  $\Delta t$ ; (*Period*)  
 $\omega = \frac{2\pi}{T}$ ; (*Fundamental rotational frequency*)  
 $f = \frac{1}{T}$ ; (*Fundamental cyclic frequency*)
```

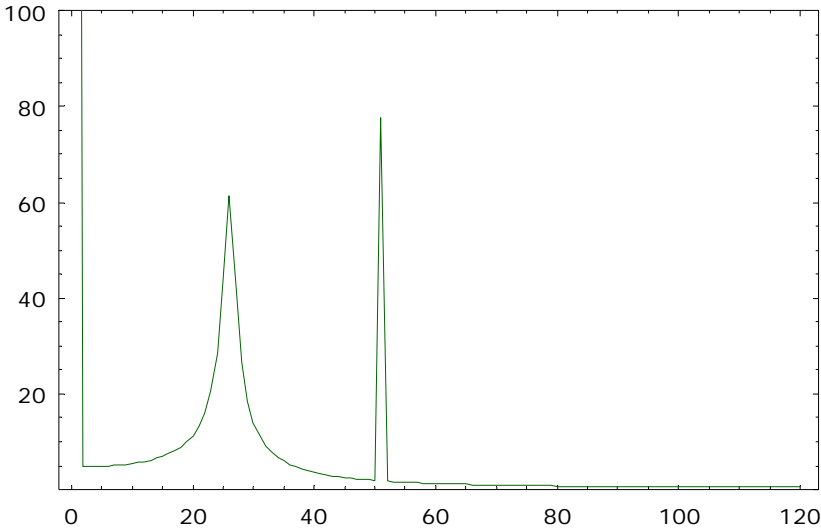
Typically, an analog waveform is produced by a transducer. Then the transducer's signal is sampled by a computer for analysis. A waveform may thus be plotted in respective ways. For example, an analog waveform is first plotted below in red. Consequently, its amplitude (of any units) may be plotted versus time (or some other units-carrying dimension) as shown. Next, a very similar waveform is created as a list of sampled points. It is plotted in blue and looks the former, but its amplitude (of any units) may only be

plotted versus the sample number. A FFT requires a 1-D set of data (amplitudes of waveform) like that used to produce the blue, digital waveform below.

```
MockFunction[t_] = 26 + 50 Sin[25 ω t] * Exp[-ω t] + 10 Sin[50 ω t];
MockData = Table[26 + 50 Sin[25  $\frac{2 \pi r}{n}$ ] * Exp[- $\frac{2 \pi r}{n}$ ] + 10 Sin[50  $\frac{2 \pi r}{n}$ ], {r, n}];
DisplayTogetherArray[{
  Plot[MockFunction[t], {t, 0, .04},
    FrameLabel->{"Time (s)", "Amplitude"},
    PlotStyle->RGBColor[1, 0, 0]],
  {ListPlot[MockData,
    FrameLabel->{"Sample Number", "Amplitude"},
    PlotJoined->True,
    PlotStyle->RGBColor[0, 0, 1]],
  ImageSize->300];
```



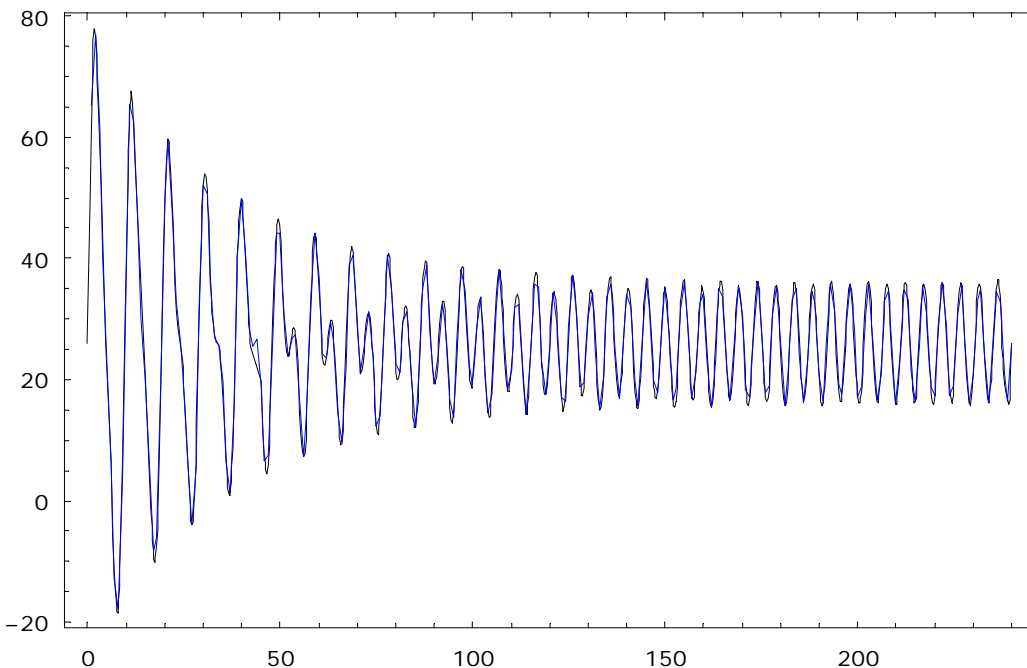
```
MockFFT = Drop[Fourier[MockData],  $\frac{-n}{2}$ ];
ListPlot[Abs[Drop[MockFFT, 0]], PlotJoined->True, PlotRange->{All, {0, 100}},
  PlotStyle->RGBColor[0, .4, 0];
```



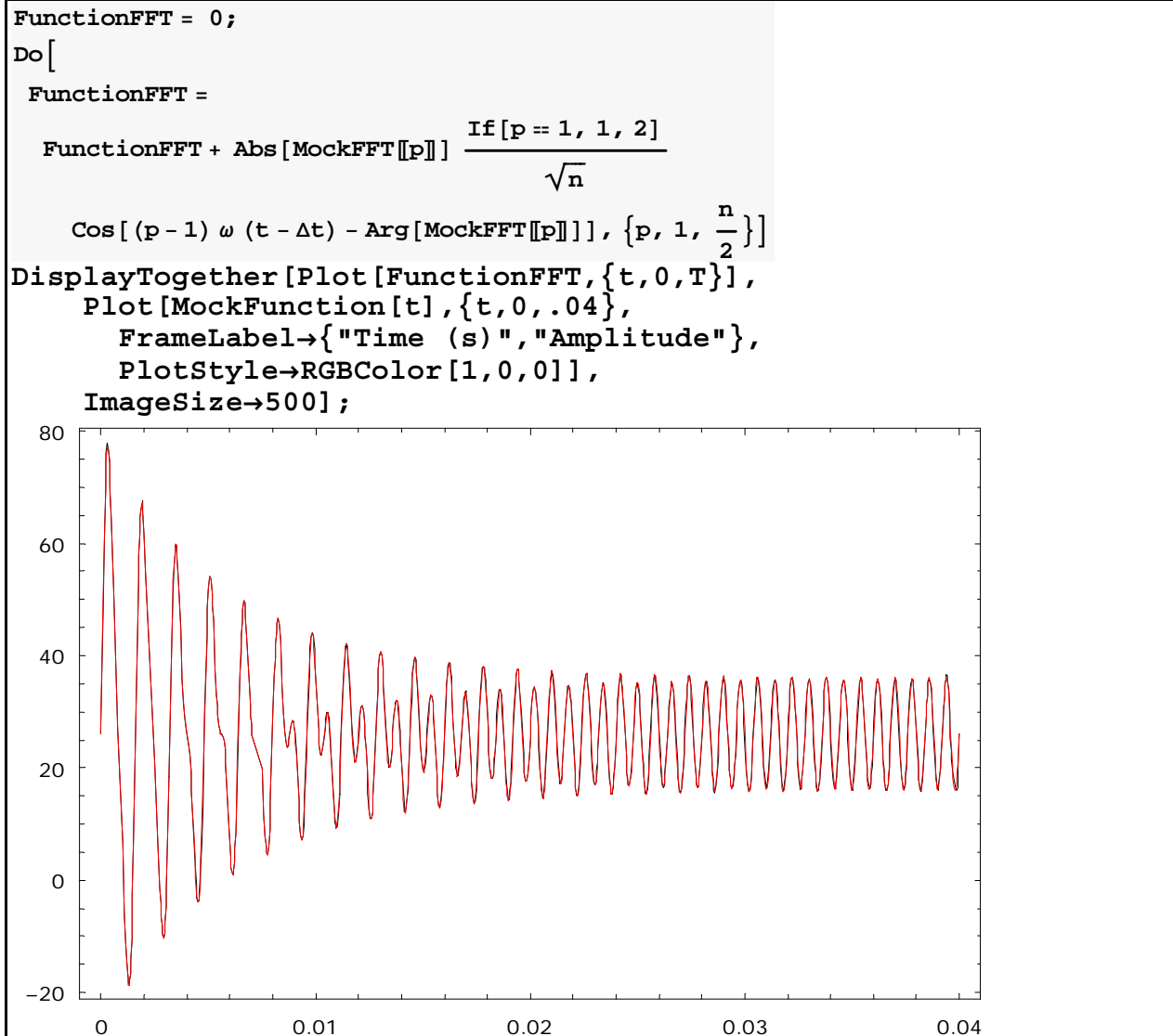
```
FunctionFFT = 0;
Do[
  FunctionFFT =
    FunctionFFT + Abs[MockFFT[[p]]]  $\frac{\text{If}[p == 1, 1, 2]}{\sqrt{n}}$ 
    Cos[ $\frac{2 \pi}{n} (p - 1) (r - 1) - \text{Arg}[\text{MockFFT}[[p]]]$ ], {p, 1,  $\frac{n}{2}$ }]
```

Here is the signal generated from the FFT results (in black) plotted on top of the original 1-D, digital signal given to the FFT (in blue):

```
DisplayTogether[Plot[FunctionFFT, {r, 0, n}],
  ListPlot[MockData, PlotJoined→True, PlotStyle→RGBColor[0, 0, 1],
    ImageSize→500];
```



Plotted below is a variation of the FFT results (in black) in which the amplitudes have been plotted versus time. They are displayed on top of the original analog signal (in red).



Application

```
Data=Transpose[Import["C:\VT Research\Raw Data\Loop Peel
(New)\FR4 25C KTest1\Force Data.txt", "Table"]][[1]];

```

Set n = number of samples in waveform to be analyzed, and force to be even for simplicity.

```
If[EvenQ[Length[Data]], n=Length[Data];, Data=Drop[Data, -
1]; n=Length[Data];]
```

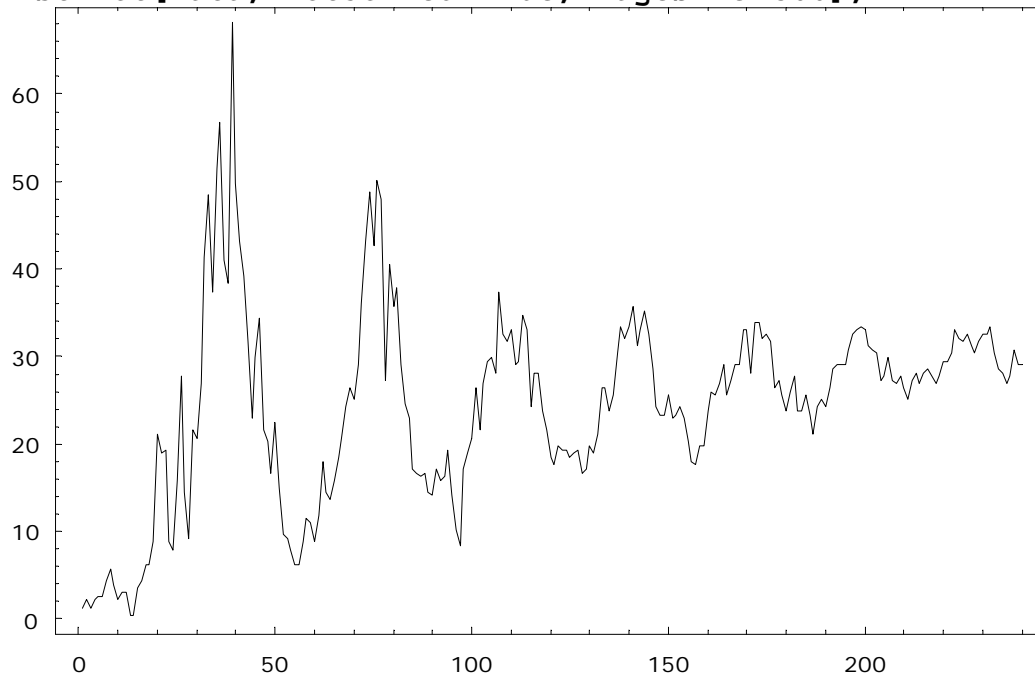
```

fs = 6000; (*Sampling frequency*)
Δt = 1/fs; (*Time interval between samples*)
T = n Δt; (*Period*)

$$\omega = \frac{2\pi}{T};$$
 (*Fundamental rotational frequency*)

$$f = \frac{1}{T};$$
 (*Fundamental cyclic frequency*)
ListPlot[Data, PlotJoined→True, ImageSize→500];

```

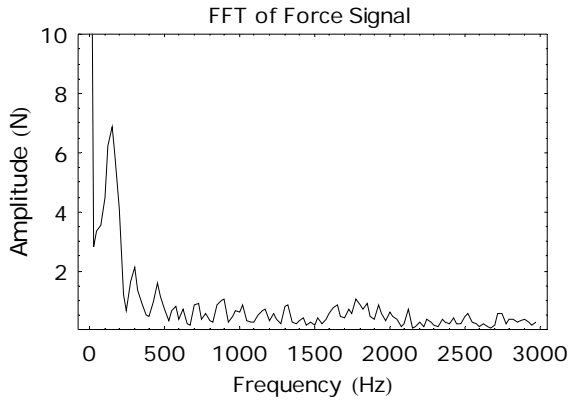


Each data point corresponds to 1/6 of a millisecond. The above signal appears (when plotted against true time) to have a harmonic component of period, $T = 5$ ms (and frequencies, $f = 200$ Hz, and $\omega = 125$ rad/sec).

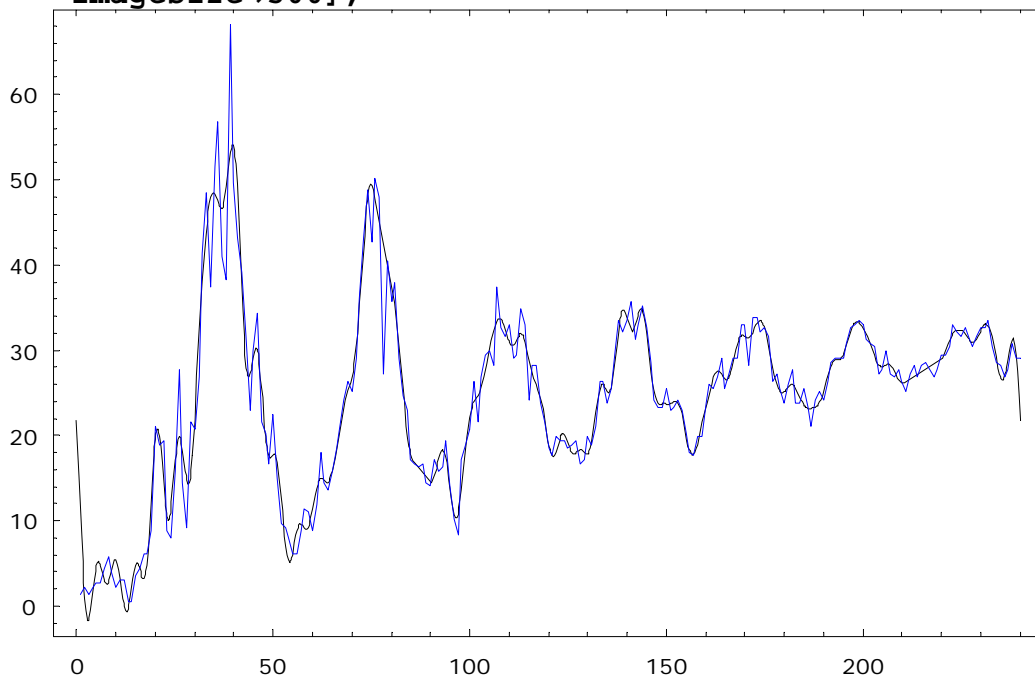
```

FFT = Drop[Fourier[Data],  $\frac{-n}{2}$ ];
amps = Table[Abs[FFT[[r]]]  $\frac{\text{If}[r == 1, 1, 2]}{\sqrt{n}}$ , {r,  $\frac{n}{2}$ ]];
freqs = Table[(r - 1) f, {r,  $\frac{n}{2}$ ]];
FFTdata = Transpose[{freqs, amps}];
ListPlot[FFTdata, PlotJoined→True, PlotRange→{All, {0, 10}}, PlotLabel->"FFT of Force Signal", FrameLabel→{"Frequency (Hz)", "Amplitude (N)"}, ImageSize→300];

```

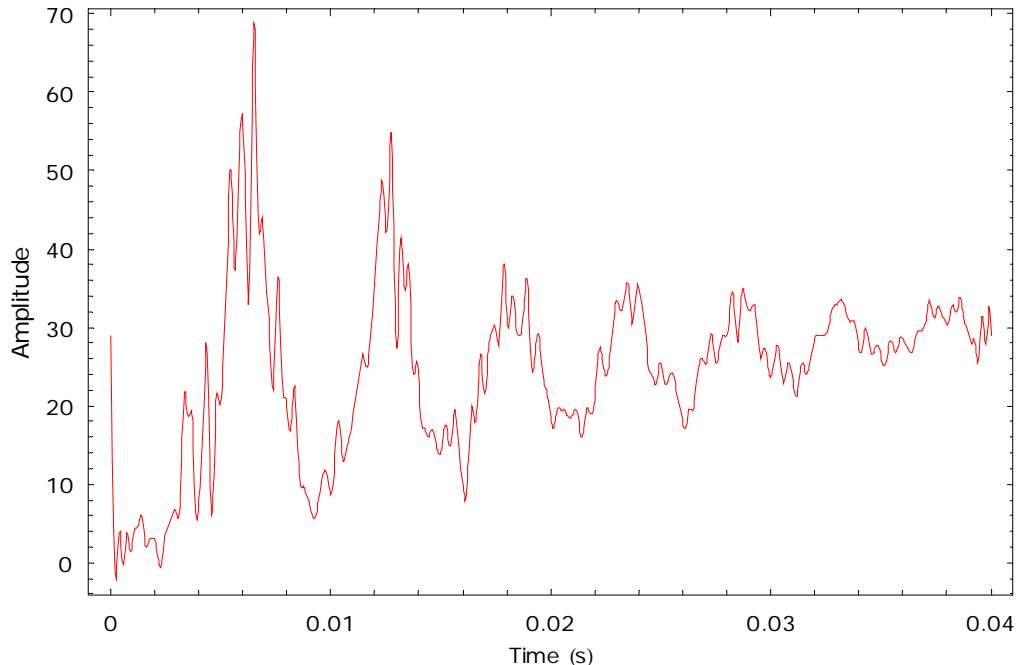


```
FunctionFFT = 0;
Do[
FunctionFFT =
FunctionFFT + Abs[FFT[r]]  $\frac{\text{If}[r == 1, 1, 2]}{\sqrt{n}}$  Cos[ $\frac{2 \pi}{n} (r - 1) (t - 1) - \text{Arg}[FFT[r]]$ ],
{r, 50}]
DisplayTogether[Plot[FunctionFFT, {t, 0, n}],
ListPlot[Data, PlotJoined→True, PlotStyle→RGBColor[0, 0, 1]],
ImageSize→500];
```



```
FunctionFFT = 0;
Do[
FunctionFFT =
FunctionFFT + Abs[FFT[p]]  $\frac{\text{If}[p == 1, 1, 2]}{\sqrt{n}}$  Cos[(p - 1) ω (t - Δt) - Arg[FFT[p]]],
{p, 1,  $\frac{n}{2}$ }]
```

```
Plot[FunctionFFT, {t, 0, T},
  FrameLabel -> {"Time (s)", "Amplitude"},
  PlotStyle -> RGBColor[1, 0, 0],
  ImageSize -> 500,
  PlotRange -> All];
```



FFT on Subdivided Signal

```
Data = Transpose[Import["C:\VT Research\Raw Data\Loop Peel
(New)\FR4 25C KTest1\Force Data.txt", "Table"]][[1]];
```

Since the frequency changes in time, let's divide up the signal into "windows in time" to see how the FFT signals change.

```
m = 1.5;
(*Divide number of samples in data by this to get
  "number of samples to be analyzed at a time"*)
n = IntegerPart[Length[Data] / m];
(*Number of samples that will be analyzed at a time with FFT*)
fs = 6000; (*Sampling frequency*)
Δt = 1 / fs; (*Time interval between samples*)
T = n Δt; (*Period*)
ω =  $\frac{2\pi}{T}$ ; (*Fundamental rotational frequency*)
f =  $\frac{1}{T}$ ; (*Fundamental cyclic frequency*)
```

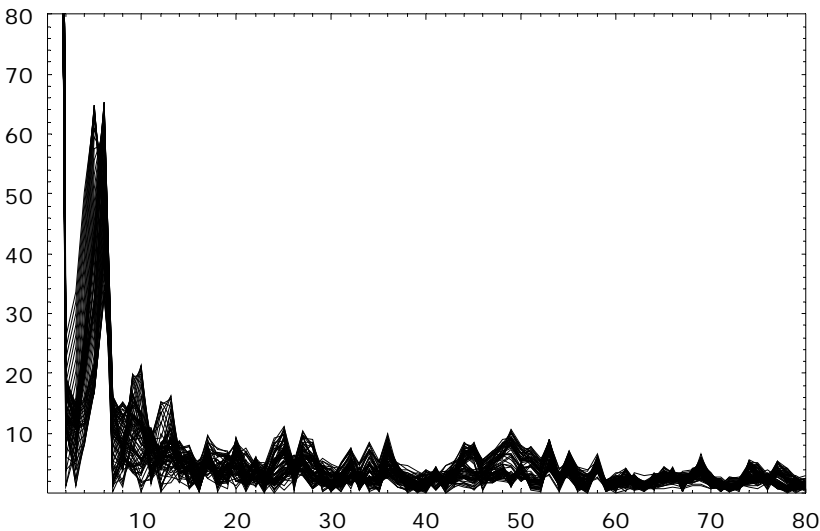
Each term in FFTArray corresponds to the result of an FFT analysis for a window in time. Each window is separated by Δt .

```

FFTAmpArray={}; (*Each term of FFTAmpArray contains a list of
amplitudes for that "window"*)
Do[FFTAmpArray=Append[FFTAmpArray,Fourier[Take[Data,{i,i+n}]]],{i
,Length[Data]-n}]
Plots={};

Do[Plots=Append[Plots,ListPlot[Abs[Take[FFTAmpArray[[i]],{1,Round[n
/2]}]],PlotJoined→True,PlotRange→{{0,n/2},{0,80}}]],{i,Length[FF
TAmpArray]};
Show[Plots];

```



Gives the position of the largest peak for the "ith" (50) FFTArray, where the DC term at position 1 is dropped.

```

Ordering[Abs[Take[FFTAmpArray[[50]],{2,Round[n/2]}]],-1][[1]];

```

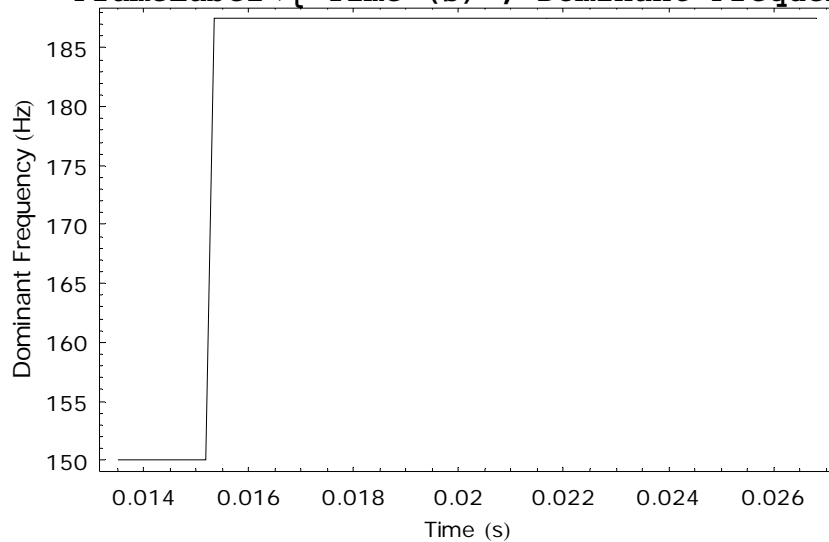
Each term of MaxFreq contains the dominant frequency (highest non-DC peak) of the FFT for a given window in time. Since the "windows" move in time, each window must be related to a specific moment in time. These moments are here defined for each window as that time/moment in the middle of the range defined by the width of the window.

```

MaxFreq = {};
Do[
  MaxFreq =
  Append[MaxFreq, f Ordering[Abs[Take[FFTAmpArray[[i]],{2,Round[n/2]}]],-1][[1]],
  {i,Length[FFTAmpArray]};
WaveformTimes = Table[ $\frac{T}{2} + r \Delta t$ , {r,Length[MaxFreq]};
Points = Transpose[{WaveformTimes,MaxFreq}];

```

```
ListPlot[Points,
  PlotJoined→True,
  FrameLabel→{"Time (s)", "Dominant Frequency (Hz)"}];
```



```
For[i=1, i>Length[Points]; Points[[i, 2]]==Points[[i+1, 2]], i++];
```

```
N[{Mean[{Points[[i, 1]], Points[[i+1, 1]]}], Mean[{Points[[i, 2]], Points[[i+1, 2]]}]]]
```

```
{0.01525, 168.75}
```

The above plot essentially gives one point--corresponding to the transition between 150 and 187 Hz at 15 ms. Let's put everything above into a single Do loop and generate a list of these points corresponding to transitions as they may be resolved by using different "window" sizes.

```

FreqTransitions = {};
Do[m = (j + 20) / 20;
  (*Divide number of samples in data by m to get
  "number of samples to be analyzed at a time"*)
  n = IntegerPart[Length[Data] / m];
  (*Number of samples that will be analyzed at a time with FFT*)
  fs = 6000; (*Sampling frequency*)
  Δt = 1 / fs; (*Time interval between samples*)
  T = n Δt; (*Period*)
  ω =  $\frac{2\pi}{T}$ ; (*Fundamental rotational frequency*)
  f =  $\frac{1}{T}$ ; (*Fundamental cyclic frequency*)

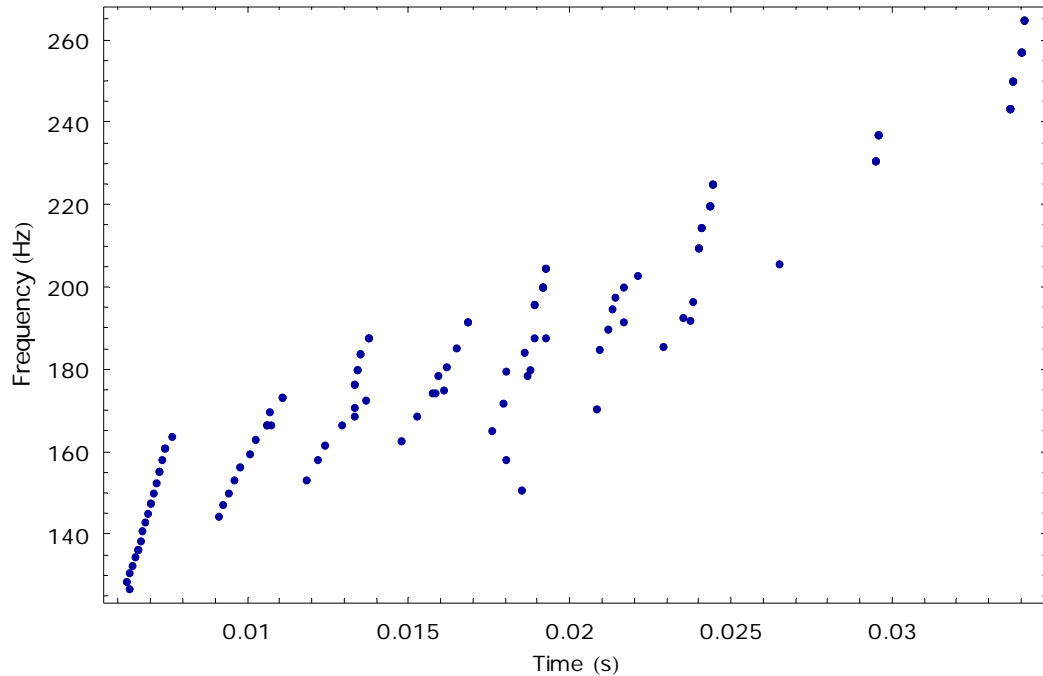
  FFTampArray = {};
  (*Each term of FFTampArray contains a list of amplitudes for that "window"*)
  Do[FFTampArray = Append[FFTampArray, Fourier[Take[Data, {i, i + n}]]],
    {i, Length[Data] - n}];

  MaxFreq = {};
  (*Each term of MaxFreq contains the dominant frequency (highest non-DC peak)
  of the FFT for a given window in time*)
  Do[
    MaxFreq =
      Append[MaxFreq, f Ordering[Abs[Take[FFTampArray[[i]], {2, Round[n / 2]}]], -1][[1]],
      {i, Length[FFTampArray]}];

  (*Since the "windows" move in time,
  each window must be related to a specific moment in time. These
  moments are here defined for each window as that time/moment in the
  middle of the range defined by the width of the window.*)
  WaveformTimes = Table[ $\frac{T}{2} + r \Delta t$ , {r, Length[MaxFreq]}];

  Points = Transpose[{WaveformTimes, MaxFreq}];
  For[i = 1, i > Length[Points]; Points[[i, 2]] = Points[[i + 1, 2]], i++];
  FreqTransitions = Append[FreqTransitions,
    {Mean[{Points[[i, 1]], Points[[i + 1, 1]]}], Mean[{Points[[i, 2]], Points[[i + 1, 2]]}]},
    {j, 120}];
ListPlot[FreqTransitions,
  ImageSize→500,
  PlotJoined→False,
  FrameLabel→{"Time (s)", "Frequency (Hz)"},
  PlotStyle→RGBColor[0, 0, .6]];

```



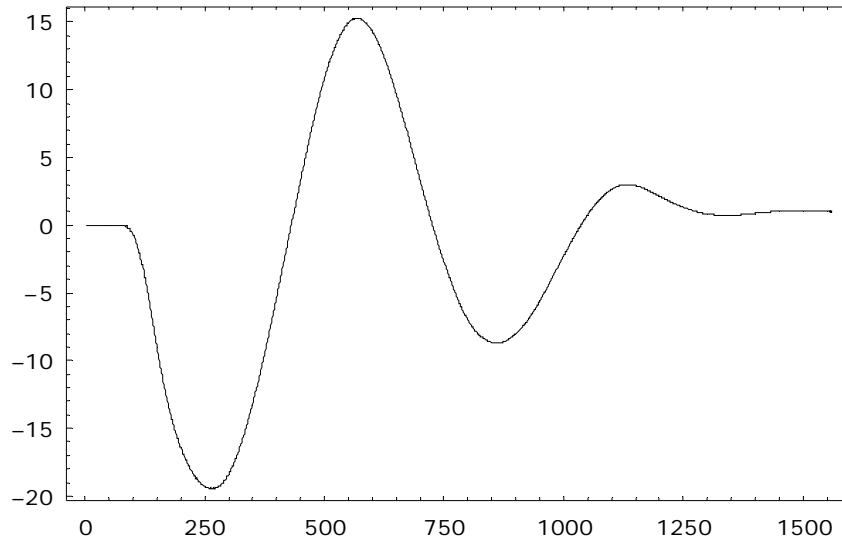
FFT on Natural Frequency Data

```
VibData=Transpose[Import["C:\VT Research\Raw Data\Loop Vibration
Tests\Averaged Data.txt","Table"]][[1]];

If[EvenQ[Length[VibData]],n=Length[VibData];,VibData=Drop[VibData
,-1];n=Length[VibData];]
fs = 6000; (*Sampling frequency*)
Δt = 1/fs; (*Time interval between samples*)
T = n Δt; (*Period*)

$$\omega = \frac{2\pi}{T};$$
 (*Fundamental rotational frequency*)

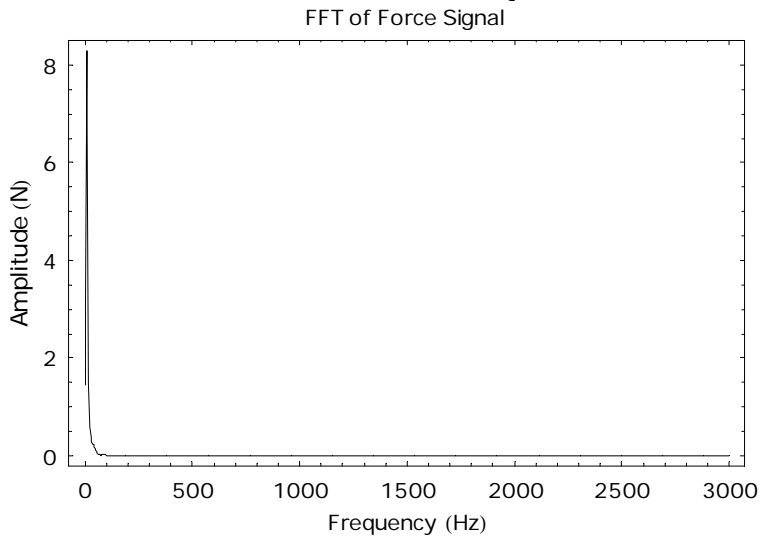
$$f = \frac{1}{T};$$
 (*Fundamental cyclic frequency*)
ListPlot[VibData,PlotJoined→True];
```



```

FFT = Drop[Fourier[VibData],  $\frac{-n}{2}$ ];
amps = Table[Abs[FFT[[r]]]  $\frac{\text{If}[r == 1, 1, 2]}{\sqrt{n}}$ , {r,  $\frac{n}{2}$ ]];
freqs = Table[(r - 1) f, {r,  $\frac{n}{2}$ ]];
FFTdata = Transpose[{freqs, amps}];
ListPlot[FFTdata, PlotJoined -> True, PlotRange -> All, PlotLabel -> "FFT
of Force Signal", FrameLabel -> {"Frequency (Hz)", "Amplitude (N)"}];

```



Dominant frequency, in Hz:

```

N[f*Ordering[Abs[FFT], All, Greater][[1]]]

```

11.5385

Loop Peel FFT Analysis

Import data

```
Data=Table[0,{i,34}];
```

E-Series

```
Data[[1]]=Transpose[Import["C:\VT Research\Raw Data\Loop Peel
```

```
(New)\E n85C Test1\Force Data.txt", "Table"]][[1];
```

```
Data[[2]]=Transpose[Import["C:\VT Research\Raw Data\Loop Peel
```

```
(New)\E n85C Test2\Force Data.txt", "Table"]][[1];
```

```
Data[[3]]=Transpose[Import["C:\VT Research\Raw Data\Loop Peel
```

```
(New)\E 27C Test1\Force Data.txt", "Table"]][[1];
```

```
Data[[4]]=Transpose[Import["C:\VT Research\Raw Data\Loop Peel
```

```
(New)\E 26C Test2\Force Data.txt", "Table"]][[1]];
```

```
Data[[5]]=Transpose[Import["C:\VT Research\Raw Data\Loop Peel
```

```
(New)\E 26C Test3\Force Data.txt", "Table"]][[1]];
```

```
Data[[6]]=Transpose[Import["C:\VT Research\Raw Data\Loop Peel
```

```
(New)\E 25C Test4\Force Data.txt", "Table"]][[1]];
```

```
Data[[7]]=Transpose[Import["C:\VT Research\Raw Data\Loop Peel
```

```
(New)\Test 1 - E at 22C\Force Data.txt", "Table"]][[1]];
```

```
Data[[8]]=Transpose[Import["C:\VT Research\Raw Data\Loop Peel
```

```
(New)\Test 2 - E at 22C\Force Data.txt", "Table"]][[1]];
```

```
Data[[9]]=Transpose[Import["C:\VT Research\Raw Data\Loop Peel
```

```
(New)\Test 3 - E at 22C\Force Data.txt", "Table"]][[1]];
```

```
Data[[10]]=Transpose[Import["C:\VT Research\Raw Data\Loop Peel
```

```
(New)\Test 4 - E at 22C\Force Data.txt", "Table"]][[1]];
```

```
Data[[11]]=Transpose[Import["C:\VT Research\Raw Data\Loop Peel
```

```
(New)\E 125C Test2\Force Data.txt", "Table"]][[1]];
```

```
Data[[12]]=Transpose[Import["C:\VT Research\Raw Data\Loop Peel  
  
(New)\E 125C Test3\Force Data.txt", "Table"]][[1]];
```

```
Data[[13]]=Transpose[Import["C:\VT Research\Raw Data\Loop Peel  
  
(New)\E 125C Test4\Force Data.txt", "Table"]][[1]];
```

N-Series, RT

```
Data[[14]]=Transpose[Import["C:\VT Research\Raw Data\Loop Peel  
  
(New)\RT n30C KTest2\Force Data.txt", "Table"]][[1]];
```

```
Data[[15]]=Transpose[Import["C:\VT Research\Raw Data\Loop Peel  
  
(New)\RT n30C KTest3\Force Data.txt", "Table"]][[1]];
```

```
Data[[16]]=Transpose[Import["C:\VT Research\Raw Data\Loop Peel
```

```
(New)\RT n30C KTest4\Force Data.txt", "Table"]][[1];
```

```
Data[[17]]=Transpose[Import["C:\VT Research\Raw Data\Loop Peel
```

```
(New)\RT 26C KTest1\Force Data.txt", "Table"]][[1];
```

```
Data[[18]]=Transpose[Import["C:\VT Research\Raw Data\Loop Peel
```

```
(New)\RT 26C KTest2\Force Data.txt", "Table"]][[1];
```

```
Data[[19]]=Transpose[Import["C:\VT Research\Raw Data\Loop Peel
```

```
(New)\RT 125C KTest1\Force Data.txt", "Table"]][[1];
```

```
Data[[20]]=Transpose[Import["C:\VT Research\Raw Data\Loop Peel
```

```
(New)\RT 125C KTest2\Force Data.txt", "Table"]][[1]];
```

```
Data[[21]]=Transpose[Import["C:\VT Research\Raw Data\Loop Peel
```

```
(New)\RT 125C KTest3\Force Data.txt", "Table"]][[1]];
```

```
Data[[22]]=Transpose[Import["C:\VT Research\Raw Data\Loop Peel
```

```
(New)\RT 125C KTest4\Force Data.txt", "Table"]][[1]];
```

FR4

```
Data[[23]]=Transpose[Import["C:\VT Research\Raw Data\Loop Peel
```

```
(New)\FR4 n30C KTest1\Force Data.txt", "Table"]][[1]];
```

```
Data[[24]]=Transpose[Import["C:\VT Research\Raw Data\Loop Peel
```

```
(New)\FR4 n30C KTest2\Force Data.txt", "Table"]][[1]];
```

```
Data[[25]]=Transpose[Import["C:\VT Research\Raw Data\Loop Peel
```

```
(New)\FR4 22C Test1\Force Data.txt", "Table"]][[1]];
```

```
Data[[26]]=Transpose[Import["C:\VT Research\Raw Data\Loop Peel
```

```
(New)\FR4 22C Test2\Force Data.txt", "Table"]][[1]];
```

```
Data[[27]]=Transpose[Import["C:\VT Research\Raw Data\Loop Peel
```

```
(New)\FR4 23C Test3\Force Data.txt", "Table"]][[1]];
```

```
Data[[28]]=Transpose[Import["C:\VT Research\Raw Data\Loop Peel
```

```
(New)\FR4 23C Test4\Force Data.txt", "Table"]][[1];
```

```
Data[[29]]=Transpose[Import["C:\VT Research\Raw Data\Loop Peel
```

```
(New)\FR4 25C KTest1\Force Data.txt", "Table"]][[1];
```

```
Data[[30]]=Transpose[Import["C:\VT Research\Raw Data\Loop Peel
```

```
(New)\FR4 25C KTest2\Force Data.txt", "Table"]][[1];
```

```
Data[[31]]=Transpose[Import["C:\VT Research\Raw Data\Loop Peel
```

```
(New)\FR4 125C Test1\Force Data.txt", "Table"]][[1];
```

```
Data[[32]]=Transpose[Import["C:\VT Research\Raw Data\Loop Peel
```

```
(New)\FR4 125C Test2\Force Data.txt", "Table"]][[1]]];
```

```
Data[[33]]=Transpose[Import["C:\VT Research\Raw Data\Loop Peel
```

```
(New)\FR4 125C Test4\Force Data.txt", "Table"]][[1]]];
```

```
Data[[34]]=Transpose[Import["C:\VT Research\Raw Data\Loop Peel
```

```
(New)\FR4 125C KTest1\Force Data.txt", "Table"]][[1]]];
```

Determine for each data set

```

FreqData = {};
Limits = {144, 147, 80, 118, 121, 141, 112, 95, 35, 105, 94, 56, 45, 0, 0,
        66, 84, 67, 80., 65, 82, 169, 65, 94, 154, 171, 77, 137, 180, 43, 73, 126,
        114, 124};
Do[FreqTransitions = {};
  Do[m = (j + 20) / 20;
    (*Divide number of samples in data by m to get
    "number of samples to be analyzed at a time"*)
    n = IntegerPart[Length[Data[[q]] / m];
    (*Number of samples that will be analyzed at a time with FFT*)
    fs = 6000; (*Sampling frequency*)
    Δt = 1 / fs; (*Time interval between samples*)
    T = n Δt; (*Period*)
    ω =  $\frac{2\pi}{T}$ ; (*Fundamental rotational frequency*)
    f =  $\frac{1}{T}$ ; (*Fundamental cyclic frequency*)

    FFTampArray = {};
    (*Each term of FFTampArray contains a list of amplitudes for that "window"*)
    Do[FFTampArray = Append[FFTampArray, Fourier[Take[Data[[q]], {i, i + n}]]],
      {i, Length[Data[[q]]] - n}];

    MaxFreq = {};
    (*Each term of MaxFreq contains the dominant frequency (highest non-DC peak)
    of the FFT for a given window in time*)
    Do[
      MaxFreq = Append[MaxFreq,
        f Ordering[Abs[Take[FFTampArray[[i]], {2, Round[n / 2]}]], -1][[1]],
        {i, Length[FFTampArray]}];

    (*Since the "windows" move in time,
    each window must be related to a specific moment in time. These
    moments are here defined for each window as that time/moment in
    the middle of the range defined by the width of the window.*)
    WaveformTimes = Table[ $\frac{T}{2} + r \Delta t$ , {r, Length[MaxFreq]}];

    Points = Transpose[{WaveformTimes, MaxFreq}];
    For[i = 1, If[i + 1 < Length[Points], Points[[i, 2]] == Points[[i + 1, 2]], Continue[]],
      i++];
    FreqTransitions = Append[FreqTransitions,
      {Mean[{Points[[i, 1]], Points[[i + 1, 1]]}], Mean[{Points[[i, 2]], Points[[i + 1, 2]]}]}],
      {j, 200}];
    FreqData = Append[FreqData, Take[FreqTransitions, Limits[[q]]];
    Print[q, " of 34",
    {q, 34}]

```

```

Do [ListPlot [FreqData [[i]],

      ImageSize→600,
      PlotJoined→False,
      FrameLabel→{"Time (s)", "Frequency (Hz)"},
      PlotStyle→RGBColor [1, 0, 0],
      PlotRange→All], {i, 34}];

```

Consider Temperature and Material Dependencies

```

Functions={};

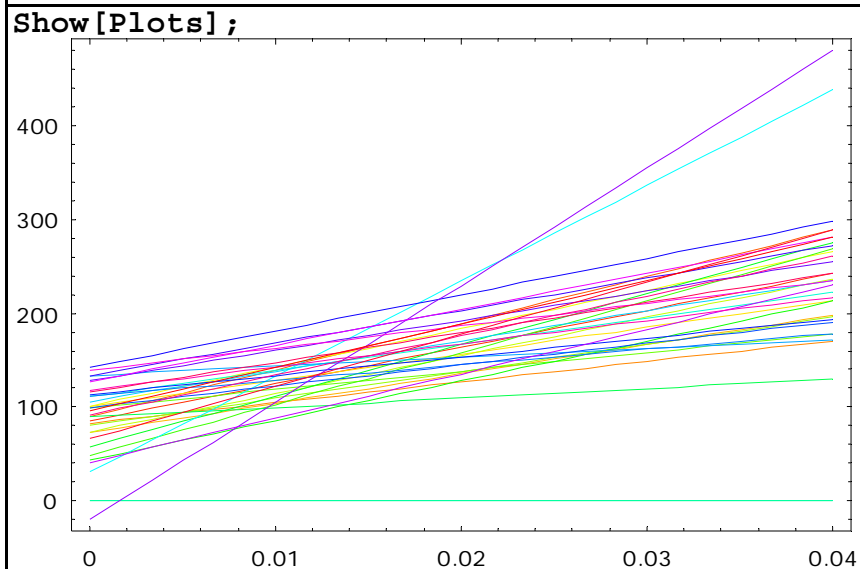
Do [Functions=Append [Functions, g [x_]=Fit [FreqData [[q]], {1, x}, x]], {q,

34}]
Plots={};

Do [Print [i]; Plots=Append [Plots, Plot [Functions [[i]], {x, 0, .04}, PlotSt

yle→Hue [i/34]]], {i, 34}]

```



Neither temperature nor material dependencies are observed. Therefore, all results will be averaged, except for the few outliers evident in the plots above.

```

Functions=Join[Take[Functions,{1,12}],Take[Functions,{16,16}],Take
e[Functions,{18,25}],Take[Functions,{27,34}]];
Plots={};

```

```

Do[Print[i];Plots=Append[Plots,Plot[Functions[[i]},{x,0,.04},PlotSt

```

```

yle→Hue[i/29]]],{i,29}]

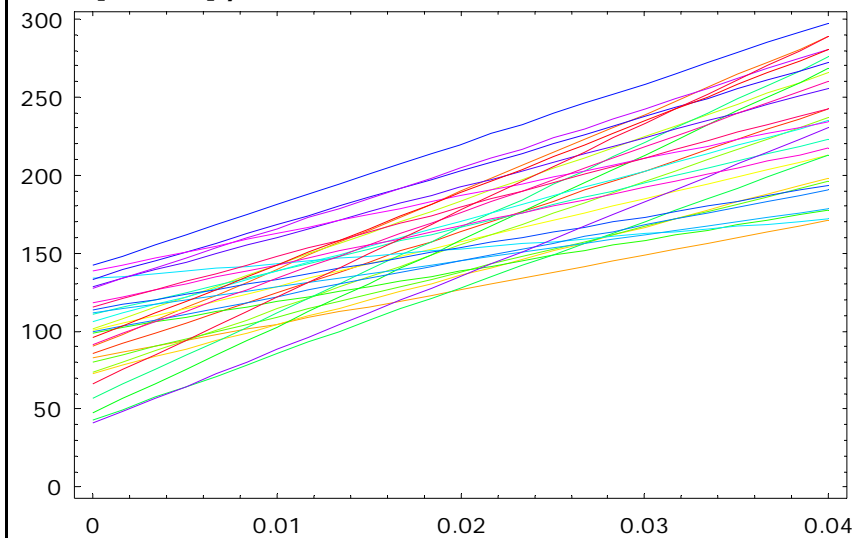
```

1

```

Show[Plots];

```



Final result

```

Num=0;

```

```

Do[Num=Num+Functions[[i]},{i,Length[Functions]}]

```

```

Avg=Num/Length[Functions];

```

```

Dots=Transpose[Table[x=(j-

```

```

1)*.02;Functions[[i]},{i,Length[Functions]},{j,3}]];

```

```

StDev=Mean[Table[StandardDeviation/.DispersionReport[Dots[[i]][[2]]

```

```

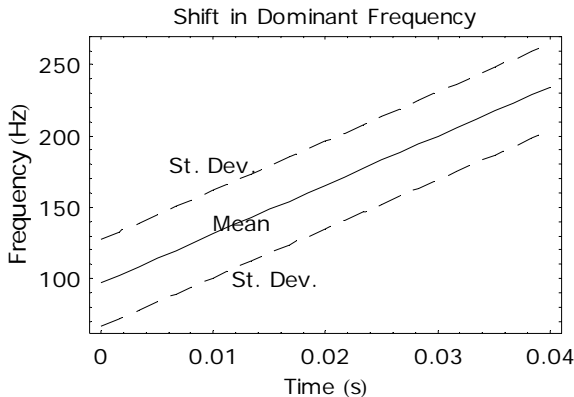
,{i,3}]];

```

```

<<Graphics`Legend`
DisplayTogether[Plot[Avg, {x, 0, .04}, PlotStyle->Thickness[.005]],
  Plot[Avg+StDev, {x, 0, .04}, PlotStyle->Dashing[{.05, .03}]],
  Plot[Avg-StDev, {x, 0, .04}, PlotStyle->Dashing[{.05, .03}]],
  Show[Graphics[Text["Mean", {.0125, 140}]]],
  Show[Graphics[Text["St. Dev.", {.01, 180}]]],
  Show[Graphics[Text["St. Dev.", {.0155, 100}]]],
  PlotLabel->"Shift in Dominant Frequency",
  FrameLabel->{"Time (s)", "Frequency (Hz)"},
  ImageSize->300];

```



D.2 DCB Data Processor

LabVIEW programs were used to analyze the sequences of images taken of DCB specimens during their fracture. The output of these LabVIEW programs was a matrix of data including coordinate pairs that defined the profile of the DCB specimen for each instant in time. The following *Mathematica* program was written to determine the critical strain energy release rate of a DCB specimen as a function of time (or cracklength), when given the above noted matrix of coordinate pairs.

E_22C_1

Import and Scale Raw Data

A 2D matrix of data is imported such that each group of two rows represents coordinate data for a given image. The odd-numbered rows should be alike and represent the distance along the axis of the DCB specimen and measuring to the location at which an edge detection algorithm was run. The even-

numbered rows are, respectively, the distances between edges detected at the location recorded in the preceding row.

```
RawData=Import["C:\VT Research\Raw Data\Falling Wedge DCB
(New)\E_22C_1\DispData.txt", "Table"];
```

The raw data with units of pixels must be scaled to represent units of millimeters. The matrix is also here transposed for easier manipulation.

```
Data =  $\frac{100}{228}$  * Transpose [RawData] ; RawData = .
```

It is presumed that each image is obtained sequentially and uniformly in time, such that any property obtained "per image" may be referenced to time accordingly.

Record Rate (Images/sec.)

```
RecordRate=2000.;
```

Since two *columns* of data now exist for each picture recorded during the fracture event, the total number of images may be found as:

```
NumberOfImages =  $\frac{(\text{Dimensions}[Data])[1]}{2}$ 
200
```

The total time = . Therefore, a time array may be compiled as:

```
TimeArray =  $\frac{\text{Table}[i, \{i, 1, \text{NumberOfImages}\}]}{\text{RecordRate}}$  ;
```

This program was originally written to analyze coordinate data from falling wedge test images for which the wedge propagated from left to right. The following cell is used to convert data gathered on images for which the wedge propagated from right to left.

```
Do [Data[[2j - 1]] = Table [Data[[2j - 1, -
i]], {i, Length [Data[[1]]]}], {j, Length [Data] / 2}];
```

Process Data

The simple beam theory equation for the deflection of a cantilevered beam $\delta(x) = \left(\frac{Px^3}{6EI} - 3L \right)$ is used in the following nonlinear fitting program to determine the crack length of DCB specimens. When rearranged with the variables/directions corresponding to this scenario, the opening displacement Y relates to the distance X via the same force required, P, to separate the beams, modulus, E, and second moment of area, I, as $Y = \left(\frac{Px^3}{6EI} - 3L \right)$ for $x \leq a$. The opening displacement $Y = b$ for $x > a$,

and this may be accounted for algebraically by subtracting $\text{UnitStep}[x - a]$ from the right hand side. Furthermore, there exists an offset in our data due to the thickness of the bonded specimen that may be accounted for by the addition of a constant, b, which should theoretically be the same for each image. By knowing the modulus and second moment of area, the force P may be extracted via a least squares curve fit. The crack length, a, may also be determined.

```
i=1;
PointsArray={};
FitStats={};
```

```

(*Repeat body until test returns false*)
While [NumberOfImages ≥ i,
  (*Create plotable data set for a single image*)
  Points = Transpose [ {Data[[2 i - 1]], Data[[2 i]]} ];
  (*Truncate leading "zeros" from data set*)
  Label [Tag]; If [Points[[1, 1]] < 1, Points = Drop [Points, 1]; Goto [Tag]];
  (*Perform initial Least-Squares curve fit*)
  f [x_] = NonlinearFit [Points,
    b + p * (3 a (a - x)2 - (a - x)3) - p (3 a (a - x)2 - (a - x)3) * UnitStep [x - a],
    x, {{b, 0, 10}, {p, 0, 1}, {a, 300, 400}}, MaxIterations → 1000];
  (*Define residuals to the fit and use them to create a table of weights*)
  Res = Table [f [Points[[k, 1]]] - Points[[k, 2]], {k, 1, Length [Points]}];
  Wts = Table [  $\frac{\text{Abs} [\text{Res} [[j]]] - \text{Max} [\text{Abs} [\text{Res}]]}{-\text{Max} [\text{Abs} [\text{Res}]]}$ , {j, 1, Length [Points]}];
  (*Perform second Least-Squares curve fit, using weights to dictate significance of each point to the fit*)
  f [x_] = NonlinearFit [Points,
    b + p * (3 a (a - x)2 - (a - x)3) - p (3 a (a - x)2 - (a - x)3) * UnitStep [x - a],
    x, {{b, 0, 10}, {p, 0, 1}, {a, 300, 400}}, MaxIterations → 1000,
    Weights → Wts];
  (*Extract points from data set with low weights to make the curve fitting more sensitive to the remainder*)
  NewPoints = {};
  Do [If [Wts [[m]] > .1, NewPoints = Append [NewPoints, Points [[m]]],
    {m, 1, Length [Wts]}];
  (*Build array of all data sets*)
  PointsArray = Append [PointsArray, NewPoints];
  (*Perform third Least-Squares curve fit-->this time using NewPoints, which should include less noise*)
  f [x_] = NonlinearFit [NewPoints,
    b + p * (3 a (a - x)2 - (a - x)3) - p (3 a (a - x)2 - (a - x)3) * UnitStep [x - a],
    x, {{b, 0, 10}, {p, 0, 1}, {a, 300, 400}}, MaxIterations → 1000];
  (*Define residuals to the above fit and use them to create a table of weights*)
  Res = Table [f [NewPoints[[k, 1]]] - NewPoints[[k, 2]],
    {k, 1, Length [NewPoints]}];
  Wts = Table [  $\frac{\text{Abs} [\text{Res} [[j]]] - \text{Max} [\text{Abs} [\text{Res}]]}{-\text{Max} [\text{Abs} [\text{Res}]]}$ , {j, 1, Length [NewPoints]}];
  (*Perform fourth Least-Squares curve fit, using NewPoints and corresponding weights*)
  FitStats = Append [FitStats,
    NonlinearRegress [NewPoints,
      b + p * (3 a (a - x)2 - (a - x)3) - p (3 a (a - x)2 - (a - x)3) * UnitStep [x - a],
      x, {{b, 0, 10}, {p, 0, 1}, {a, 300, 400}}, MaxIterations → 1000,
      Weights → Wts, RegressionReport →
      {BestFit, BestFitParameters, FitResiduals}]];
  i++];
(*Clear obsolete variables*)
i = .
Data = .

```

```

Res=.
Wts=.
Fits={};

Do [Fits=Append [Fits, BestFit/. (Transpose [FitStats] [[1]]) [[i]], {i, 1, L

length [Transpose [FitStats] [[2]]}]

ParameterRules={};
Do [ParameterRules=Append [ParameterRules, BestFitParameters/. (Trans
pose [FitStats] [[2]]) [[i]], {i, 1, Length [Transpose [FitStats] [[2]]}]

Paramb={};
Do [Paramb=Append [Paramb, b/. (Transpose [ParameterRules] [[1]]) [[i]], {i

, 1, Length [Transpose [ParameterRules] [[1]]}]

Paramp={};
Do [Paramp=Append [Paramp, p/. (Transpose [ParameterRules] [[2]]) [[i]], {i

, 1, Length [Transpose [ParameterRules] [[1]]}]

Parama={};

```

```

Do [Parama=Append [Parama, a/. (Transpose [ParameterRules] [[3]]) [[i]], {i
,1, Length [Transpose [ParameterRules] [[1]]}]

Residuals={};

Do [Residuals=Append [Residuals, FitResiduals/. (Transpose [FitStats] [[
3]]) [[i]], {i,1, Length [Transpose [FitStats] [[2]]}]

```

```

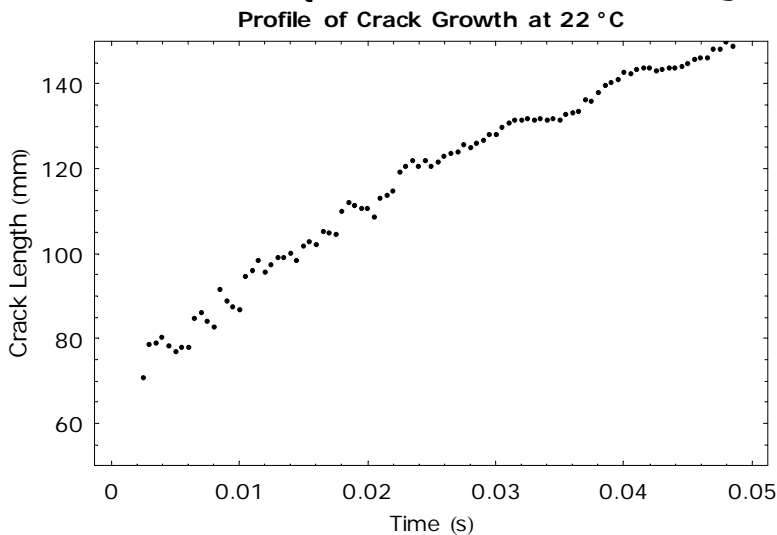
SessionTime[]
60
11.677124213

```

```

p11=ListPlot [Take [Transpose [{TimeArray, Parama}], {5,100}],
PlotRange->{50,150},
PlotLabel->StyleForm ["Profile of Crack Growth at 22
°C", FontWeight->Bold],
FrameLabel->{"Time (s)", "Crack Length (mm)"}];

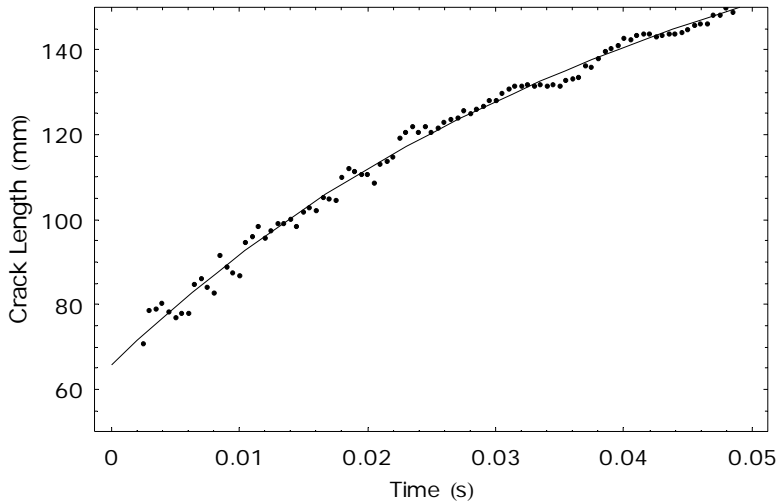
```



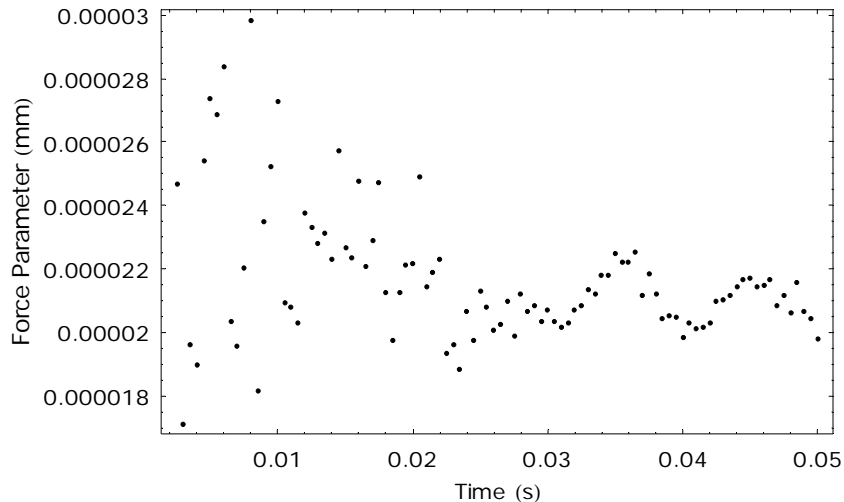
Let's try to fit a curve to the above, then use the "fit" equation to calculate the SERR.

```
FitA = Fit[Take[Transpose[{TimeArray, Parama}], {5, 100}],
  {1, x, x2, x3}, x]
65.7934 + 2894.54 x - 33078.2 x2 + 185586. x3
```

```
DisplayTogether[p11, Plot[FitA, {x, 0, .05}]];
Profile of Crack Growth at 22 °C
```



```
p12=ListPlot[Take[Transpose[{TimeArray, Paramp}], {5, 100}],
  PlotRange->All,
  PlotLabel->StyleForm["Profile of Force Parameter at 22
°C", FontWeight->Bold],
  FrameLabel->{"Time (s)", "Force Parameter (mm)"}];
Profile of Force Parameter at 22 °C
```



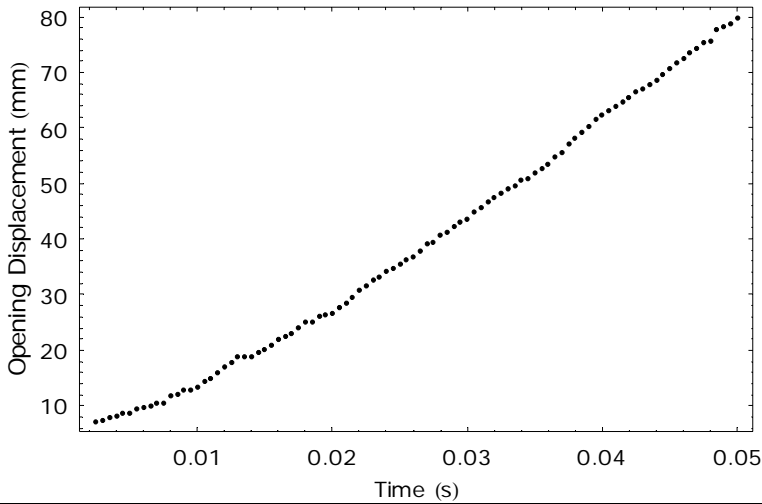
```
x=50;
```

```
OpenDisp=Table[Fits[[i]], {i, 1, Length[Fits]}];
```

```
x=.
```

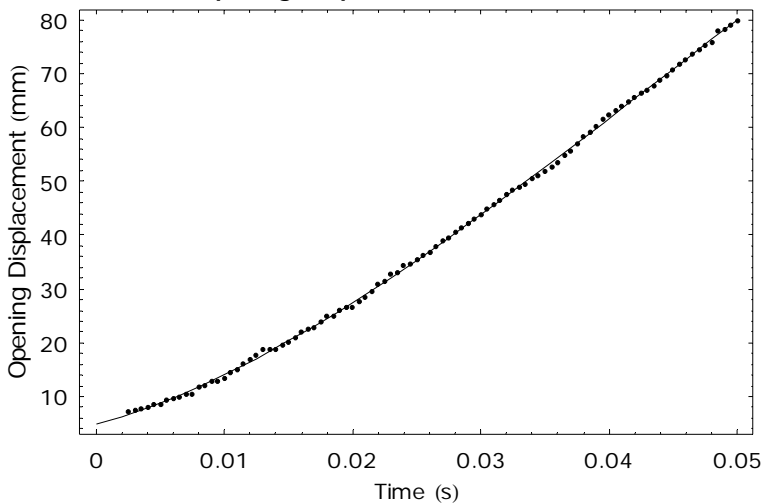
```
p13=ListPlot[Take[Transpose[{TimeArray, OpenDisp}], {5, 100}],
  PlotRange->All,
```

```
PlotLabel->StyleForm["Opening Displacement for E at 22
°C",FontWeight->Bold],
FrameLabel->{"Time (s)","Opening Displacement (mm)"}];
Opening Displacement for E at 22 °C
```



```
FitD = Fit[Take[Transpose[{TimeArray, OpenDisp}], {5, 100}],
{1, x, x^2, x^3}, x]
4.78291 + 678.647 x + 27036.9 x^2 - 211053. x^3
```

```
DisplayTogether[p13,Plot[FitD,{x,0,.05}]]];
Opening Displacement for E at 22 °C
```



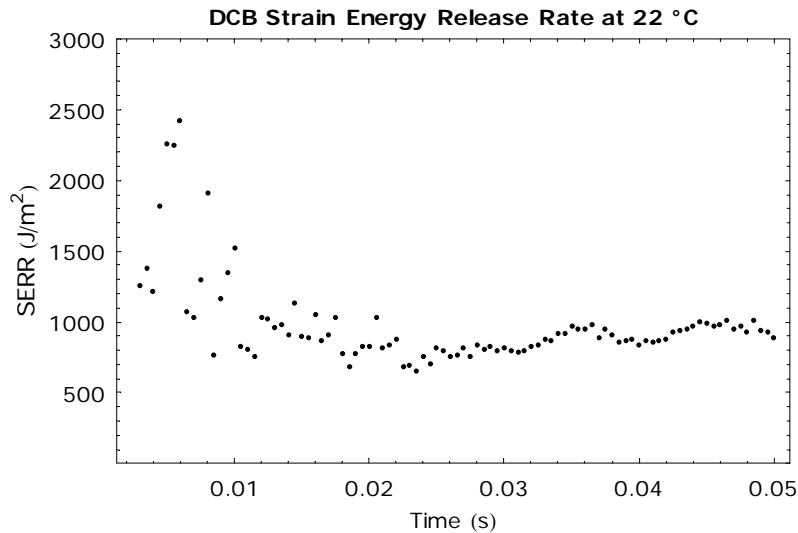
The strain energy release rate may be calculated for a DCB specimen using $SERR =$.

$E = 1.7 \text{ GPa}$ and $I =$

```

SERR = Table [  $\frac{9 \left( \frac{\text{OpenDisp}[[i]]}{1000} \right)^2 * (1.8 * 10^9) (3.5 * 10^{-11})}{4 * .00889 \left( \frac{\text{Parama}[[i]-50}{1000} \right)^4}$  ,
  {i, 1, Length[OpenDisp]} ];
SERRTime = Take[Transpose[{TimeArray, SERR}], {5, 100}];
p14 = ListPlot[SERRTime, PlotRange -> {All, {0, 3000}},
  PlotLabel -> StyleForm["DCB Strain Energy Release Rate at 22 °C",
    FontWeight -> Bold],
  FrameLabel -> {"Time (s)", "SERR (J/m2)"}];

```

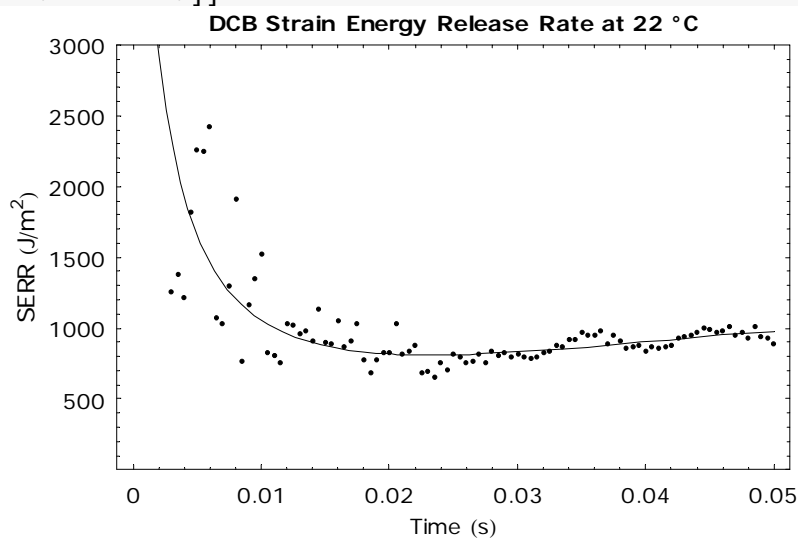


Above with SERR based on fits to data

```

DisplayTogether [p14, Plot [  $\frac{9 \left( \frac{\text{FitD}}{1000} \right)^2 * (1.8 * 10^9) (3.5 * 10^{-11})}{4 * .00889 \left( \frac{\text{FitA}-50}{1000} \right)^4}$  ,
  {x, 0, .05} ] ];

```



The SERR will be computed as the average between 10 and 50 ms, whereas data prior to 10 ms appears unreliable.

```
Mean[Table[x =  $\frac{y}{1000}$ ;  $\frac{9 \left(\frac{\text{FitD}}{1000}\right)^2 * (1.8 * 10^9) (3.5 * 10^{-11})}{4 * .00889 \left(\frac{\text{FitA}-50}{1000}\right)^4}$ , {y, 10, 50}]]
```

882.732

```
Mean1=Mean[Drop[SERR,100]];
StDev1=StandardDeviation[Drop[SERR,100]];
SERR=.
SERRTime=.
FitStats=.
Fits=.
ParameterRules=.
Paramp=.
Paramb=.
Parama=.
Residuals=.
```

D.3 Program to Generate Master Curves from DMA Data

A TA Instruments, Dynamic Mechanical Analyzer (DMA) was used to determine the variability of certain material properties with changes in temperature and bending speed for each of the printed circuit board laminates. The below program was written to generate master curves according to time-temperature-superposition theory (TTSP).

THERMOUNT E-Series (without Cu)

Import Data

```
DataFile=Import["C:/VT Research/Raw Data/DMA/Freq. Sweep - Temp.
Ramp Tests/E-no Cu.txt", "Table"];
RawData=Drop[DataFile,41];
Labels=Take[DataFile,{27,36}];

AllData=Transpose[Drop[RawData,{5,Dimensions[RawData][[1],5]}]];

FreqData100=Transpose[Take[Transpose[AllData],{1,Dimensions[AllDa
ta][[2],4]}]];
```

```
FreqData10=Transpose [Take [Transpose [AllData] , {2,Dimensions [AllData]
al [[2]],4}]]];
```

```
FreqData1=Transpose [Take [Transpose [AllData] , {3,Dimensions [AllData]
l [[2]],4}]]];
```

```
FreqDataPt1=Transpose [Take [Transpose [AllData] , {4,Dimensions [AllDa
ta] [[2]],4}]]];
```

```
TempData=Table [Take [Transpose [AllData] , {4i-
3,4i}]] , {i,1,Dimensions [AllData] [[2]]/4}];
```

```
Temps=Table [Mean [Take [AllData[[2]]] [[{4i-3,4i-2,4i-
1,4i}]]] , {i,Dimensions [AllData] [[2]]/4}];
```

Data with the 100 Hz signal removed

```
DataLess100Hz=Transpose [Drop [Transpose [AllData] , {1,Dimensions [Tra
nspose [AllData] ] [[1]],4}]]];
```

```
TempDataLess100Hz=Table[Take[Transpose[DataLess100Hz],{3i-
2,3i}],{i,1,Dimensions[DataLess100Hz][[2]]/3}];
```

Unmodified Results

TableForm[Labels]

Sig1	Time	(min)	
Sig2	Temperature	(°C)	
Sig3	Storage	Modulus	(MPa)
Sig4	Loss	Modulus	(MPa)
Sig5	Tan	Delta	
Sig6	Frequency	(Hz)	
Sig7	Amplitude	(æm)	
Sig8	Stress	(MPa)	
Sig9	Strain	(%)	
Sig10	Position	(mm)	

Plot Signal j versus Signal i for each frequency.

```
i=2;
j=5;

p1=MultipleListPlot[{Transpose[{FreqData100[[i]],FreqData100[[j]]}],

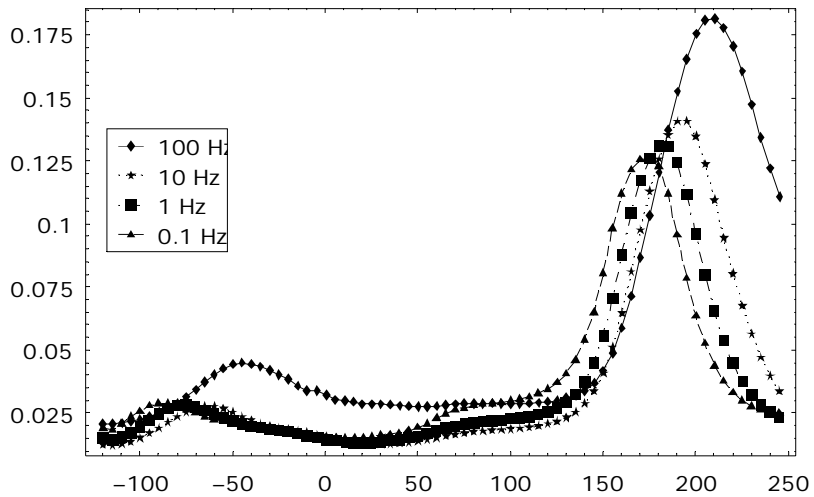
    Transpose[{FreqData10[[i]],FreqData10[[j]]}],

    Transpose[{FreqData1[[i]],FreqData1[[j]]}],

    Transpose[{FreqDataPt1[[i]],FreqDataPt1[[j]]}],

    PlotRange→All,
    PlotLegend→{"100 Hz","10 Hz","1 Hz","0.1 Hz"},
    LegendSize→{.3,.3},
    LegendPosition→{-.75,0},
    PlotJoined→True,
```

```
ImageSize→400];
i=.;j=.
```



```
i=2;
j=5;
```

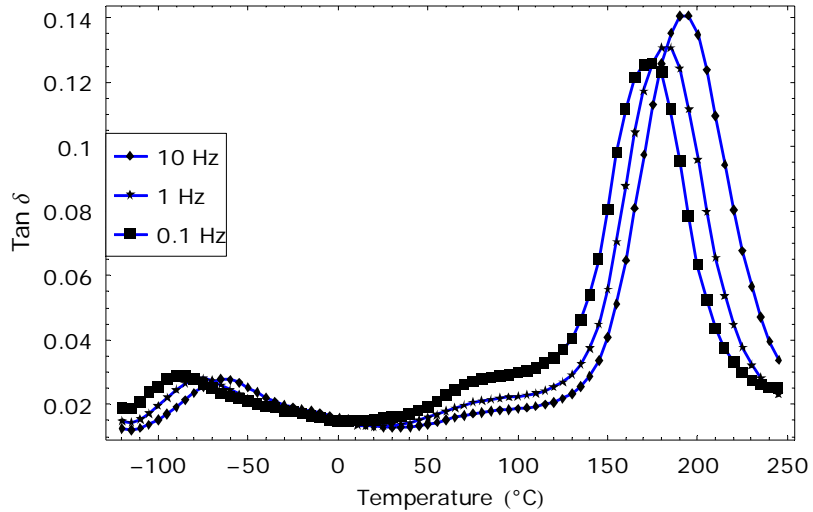
```
p1=MultipleListPlot[{Transpose[{FreqData10[[i], FreqData10[[j]]}],
```

```
Transpose[{FreqData1[[i], FreqData1[[j]]}],
```

```
Transpose[{FreqDataPt1[[i], FreqDataPt1[[j]]}],
```

```
PlotRange→All,
PlotStyle→{{RGBColor[0,0,1], Thickness[.005]}},
PlotLegend→{"10 Hz", "1 Hz", "0.1 Hz"},
LegendSize→{.3, .3},
LegendPosition→{-.75, 0},
PlotJoined→True,
ImageSize→400,
FrameLabel→{"Temperature (°C)", "Tan δ"}];
```

```
i=.;j=.
```



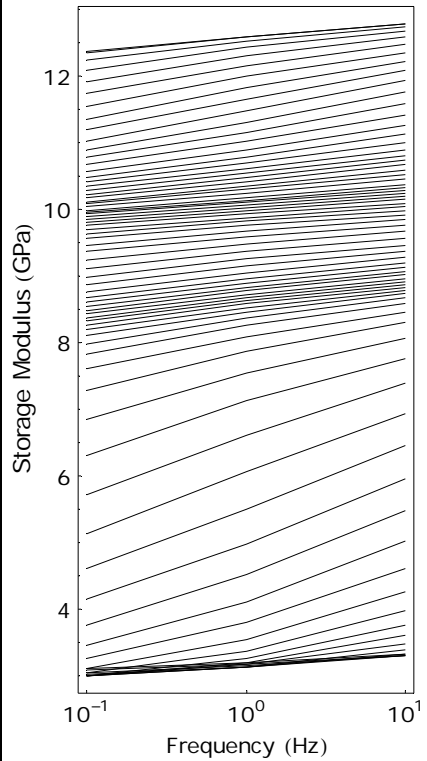
TTSP with Optimized Shift Factors

Plot Storage Modulus (Signal 3) versus Frequency (Signal 6) for each temperature.

```
p2 = {};
Do [p2 = Append [p2,
  LogLinearListPlot [
    Transpose [ { Transpose [TempDataLess100Hz[[i]]][6],
      Transpose [TempDataLess100Hz[[i]]][3] } ],
    1000,
    PlotJoined -> True,
    PlotRange -> All ] ],
  {i, Length [TempDataLess100Hz]}];
```

Display all Modulus vs. Freq. curves together.

```
p3 = DisplayTogether [
  Show [Table [p2[[i]], {i, 74}],
  PlotRange -> {All, All},
  FrameLabel -> {"Frequency (Hz)", "Storage Modulus (GPa)"},
  FrameTicks -> {{{-1, "10-1"}, {0, "100"}, {1, "101"}, {2, "102"}}},
  Automatic, None, None},
  ImageSize -> 200,
  AspectRatio -> 2];
```



```
Curves =
Table [Transpose [ {Transpose [TempDataLess100Hz [[i]] [[6]],
  Transpose [TempDataLess100Hz [[i]] [[3]]} ]], {i, Length [TempDataLess100Hz]}];
1000
```

Temperatures of the curves in degrees Celcius are:

```
Table [Mean [Transpose [TempDataLess100Hz [[i]] [[2]]], {i, 74}]

{-120.025, -114.906, -109.927, -104.998, -99.9715, -94.9511, -89.9633, -
84.9674, -79.9433, -74.9786, -70.0028, -64.9654, -59.9784, -54.9838, -
49.9743, -44.9818, -39.9556, -34.9632, -29.9872, -24.9904, -19.9843, -
14.9847, -9.96657, -
4.25312, 0.589057, 5.76323, 10.7629, 15.5014, 20.2111, 25.0934, 30.081, 3
5.0463, 40.0166, 45.057, 50.0901, 55.1169, 60.1337, 65.1312, 70.1242, 75.
1224, 80.1192, 85.1188, 90.1179, 95.1187, 100.119, 105.121, 110.123, 115.
125, 120.127, 125.128, 130.13, 135.134, 140.134, 145.137, 150.137, 155.14
, 160.138, 165.139, 170.139, 175.145, 180.147, 185.153, 190.151, 195.155,
200.153, 205.16, 210.154, 215.161, 220.155, 225.161, 230.158, 235.167, 24
0.158, 245.167}
```

Choose a reference temperature for the master curve (multiple of 5).

```
RefTemp=25;
```

```
RefPos=Position [Table [Mean [Transpose [TempDataLess100Hz[[i]]][2]], {
i, 74}], _? (Round [#]==RefTemp&)] [[1, 1]];
```

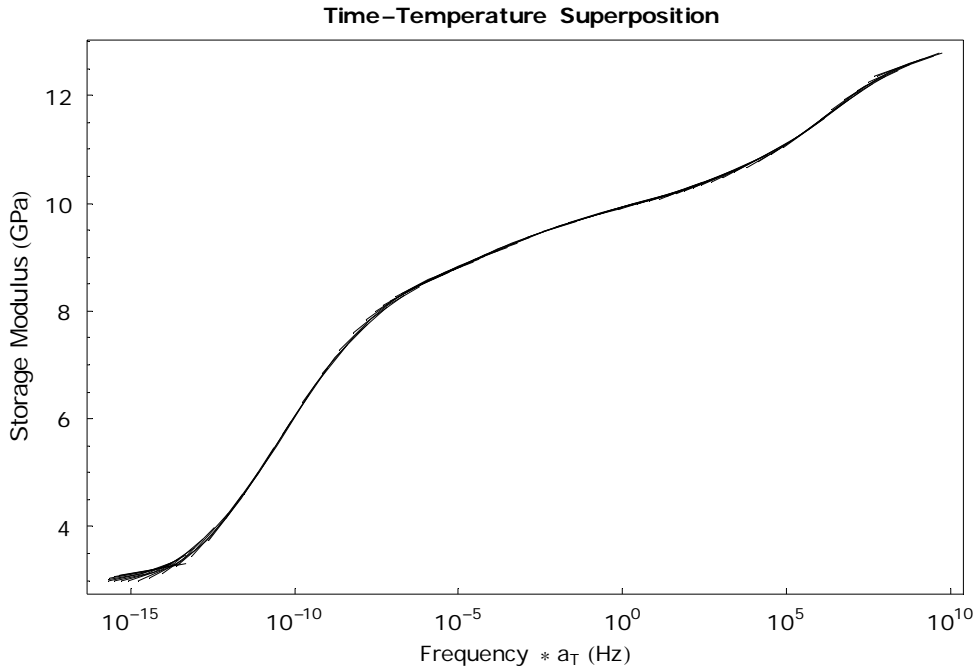
```
ShiftFactors = {0};
Do[Δ = {};
  Δ = Append[Δ, ( Transpose [Curves[[i + 1]][2, 1] - Transpose [Curves[[i]][2, 2]
  Transpose [Curves[[i]][2, 1] - Transpose [Curves[[i]][2, 2] - 1 )];
  Δ = Append[Δ, ( Transpose [Curves[[i + 1]][2, 2] - Transpose [Curves[[i]][2, 3]
  Transpose [Curves[[i]][2, 2] - Transpose [Curves[[i]][2, 3] - 1 )];
  ShiftFactors = Append[ShiftFactors, Mean[Δ] + ShiftFactors[[i]]
  , {i, 73}];
ShiftFactors = ShiftFactors - ShiftFactors[[RefPos]];
```

Plot shifted Storage Modulus (Signal 3) versus Frequency (Signal 6) for each temperature.

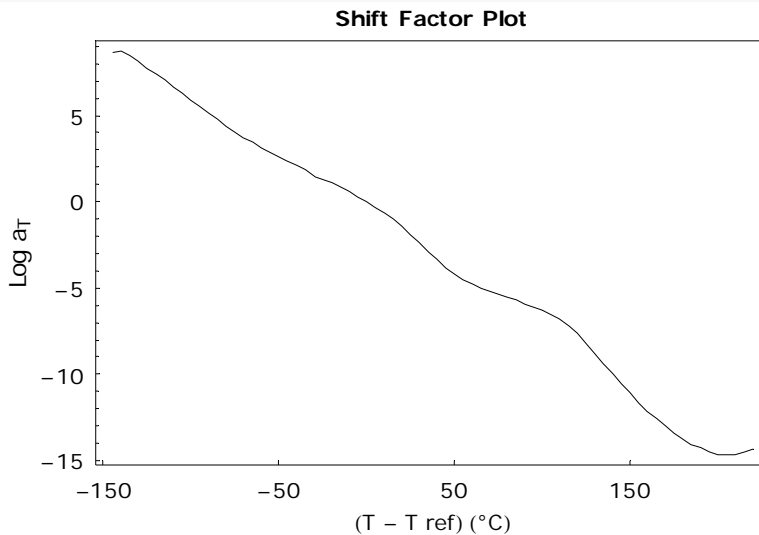
```
p4 = {};
Do[p4 = Append[p4,
  LogLinearListPlot [
    Transpose [ { Transpose [TempDataLess100Hz[[i]][6] * 10ShiftFactors[[i]],
    Transpose [TempDataLess100Hz[[i]][3]
    1000 } ] ],
    PlotJoined → True,
    PlotRange → All ] ],
  {i, 74}];
```

Plot master curve.

```
p5 = DisplayTogether [
  Show [Table [p4[[i]], {i, 1, Length [p4]}],
  PlotRange → All,
  PlotLabel → StyleForm ["Time-Temperature Superposition", FontWeight → Bold],
  FrameLabel → {"Frequency * aT (Hz)", "Storage Modulus (GPa)"},
  FrameTicks → {{{-15, "10-15"}, {-10, "10-10"}, {-5, "10-5"}, {0, "100"},
  {5, "105"}, {10, "1010"}, Automatic, None, None}},
  (*Show [
  Graphics [Text [TableForm [{"Ref. Temp.", "=", RefTemp, "°C"}],
  TableSpacing → {0, 1}], {-6.5 + ShiftFactors[[RefPos]], 11.5}]]], *)
  ImageSize → 500];
```



```
p6 = ListPlot[Transpose[{Temps - Temps[[RefPos]], ShiftFactors}],
  PlotLabel → StyleForm["Shift Factor Plot", FontWeight → Bold],
  FrameLabel → {"(T - T ref) (°C)", "Log aT"},
  FrameTicks → {{-150, -50, 50, 150, 250}, Automatic, None, None},
  PlotJoined → True,
  ImageSize → 400];
```



THERMOUNT E-Series (with Cu)

Import Data

```
DataFile=Import["C:/VT Research/Raw Data/DMA/Freq. Sweep - Temp.
Ramp Tests/E-Cu.txt", "Table"];
RawData=Drop[DataFile, 41];
```

```

Labels=Take [DataFile, {27,36}];

AllData=Transpose [Drop [RawData, {5,Dimensions [RawData] [[1],5}]]];

FreqData100=Transpose [Take [Transpose [AllData], {1,Dimensions [AllData]
[[2],4}]]];

FreqData10=Transpose [Take [Transpose [AllData], {2,Dimensions [AllData]
[[2],4}]]];

FreqData1=Transpose [Take [Transpose [AllData], {3,Dimensions [AllData]
[[2],4}]]];

FreqDataPt1=Transpose [Take [Transpose [AllData], {4,Dimensions [AllData]
[[2],4}]]];

TempData=Table [Take [Transpose [AllData], {4i-
3,4i}], {i,1,Dimensions [AllData] [[2]/4}];

```

```

Temps=Table [Mean [Take [AllData[[2]]][{4i-3,4i-2,4i-
1,4i}]]],{i,Dimensions [AllData] [[2]]/4}];

```

Data with the 100 Hz signal removed

```

DataLess100Hz=Transpose [Drop [Transpose [AllData],{1,Dimensions [Tra
nspose [AllData] ] [[1]],4}]]];

```

```

TempDataLess100Hz=Table [Take [Transpose [DataLess100Hz],{3i-
2,3i}],{i,1,Dimensions [DataLess100Hz] [[2]]/3}];

```

Unmodified Results

TableForm [Labels]

Sig1	Time	(min)	
Sig2	Temperature	(°C)	
Sig3	Storage	Modulus	(MPa)
Sig4	Loss	Modulus	(MPa)
Sig5	Tan	Delta	
Sig6	Frequency	(Hz)	
Sig7	Amplitude	(æm)	
Sig8	Stress	(MPa)	
Sig9	Strain	(%)	
Sig10	Position	(mm)	

Plot Signal j versus Signal i for each frequency.

```

i=2;
j=5;

q1=MultipleListPlot [{Transpose [{FreqData100[[i]],FreqData100[[j]]}],

```

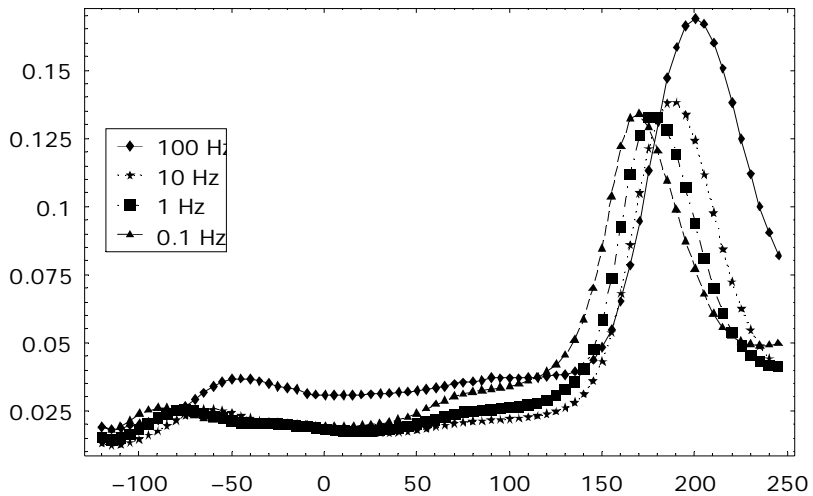
```
Transpose[{FreqData10[[i]], FreqData10[[j]]}],
```

```
Transpose[{FreqData1[[i]], FreqData1[[j]]}],
```

```
Transpose[{FreqDataPt1[[i]], FreqDataPt1[[j]]}],
```

```
PlotRange→All,  
PlotLegend→{"100 Hz", "10 Hz", "1 Hz", "0.1 Hz"},  
LegendSize→{.3, .3},  
LegendPosition→{-.75, 0},  
PlotJoined→True,  
ImageSize→400];
```

```
i=.;j=.;
```



```
i=2;
```

```
j=5;
```

```
q1=MultipleListPlot[{Transpose[{FreqData10[[i]], FreqData10[[j]]}],
```

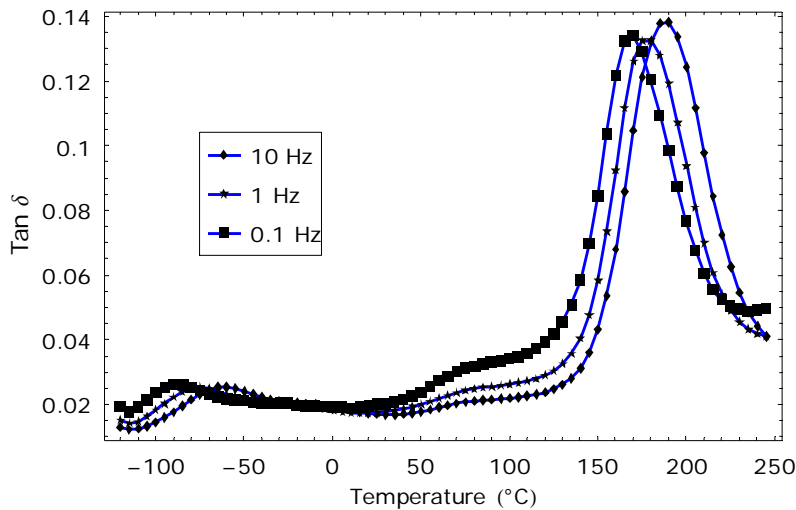
```

Transpose[{FreqData1[[i]], FreqData1[[j]]}],

Transpose[{FreqDataPt1[[i]], FreqDataPt1[[j]]}],

PlotRange→All,
PlotStyle→{{RGBColor[0,0,1], Thickness[.005]}},
PlotLegend→{"10 Hz", "1 Hz", "0.1 Hz"},
LegendSize→{.3, .3},
LegendPosition→{-.5, 0},
PlotJoined→True,
ImageSize→400,
FrameLabel→{"Temperature (°C)", "Tan δ"}];
i=.; j=.;

```



TTSP with Optimized Shift Factors

Plot Storage Modulus (Signal 3) versus Frequency (Signal 6) for each temperature.

```

q2 = {};
Do [q2 = Append [q2,
  LogLinearListPlot [
    Transpose [ { Transpose [TempDataLess100Hz [[i]]] [[6],
      Transpose [TempDataLess100Hz [[i]]] [[3]]
    } ] / 1000,
    PlotJoined → True,
    PlotRange → All ] ],
  {i, Length [TempDataLess100Hz] }];

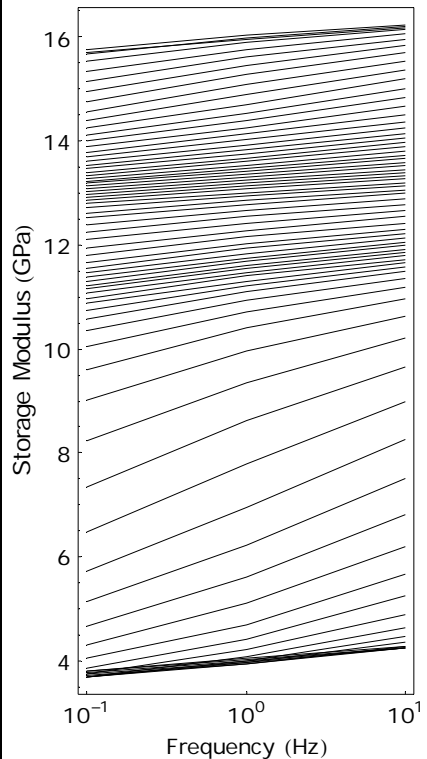
```

Display all Modulus vs. Freq. curves together.

```

q3 = DisplayTogether [
  Show[Table[q2[[i]], {i, 74}],
    PlotRange -> {All, All},
    FrameLabel -> {"Frequency (Hz)", "Storage Modulus (GPa)"},
    FrameTicks -> {{{-1, "10-1"}, {0, "100"}, {1, "101"}, {2, "102"}}},
    Automatic, None, None},
  ImageSize -> 200,
  AspectRatio -> 2]];

```



```

Curves =
  Table [Transpose [ {Transpose [TempDataLess100Hz[[i]]][[6],
    Transpose [TempDataLess100Hz[[i]]][[3]]
    }], {i, Length[TempDataLess100Hz]}];

```

Temperatures of the curves in degrees Celcius are:

```

Table [Mean [Transpose [TempDataLess100Hz[[i]]][[2]]], {i, 74}]

```

```

{-120.005, -114.911, -109.897, -104.874, -99.9404, -94.9312, -89.9808, -
84.9339, -79.9715, -74.9167, -69.9559, -64.9276, -59.9747, -54.9691, -
49.9858, -44.9663, -39.9515, -34.9625, -29.9732, -24.9886, -19.973, -
14.9489, -9.45874, -
4.5358, 0.633222, 5.60803, 10.5696, 15.4142, 20.2266, 25.1484, 30.1171, 3

```

```
5.0847, 40.057, 45.0946, 50.1086, 55.1268, 60.152, 65.1518, 70.144, 75.13
92, 80.1355, 85.1332, 90.1338, 95.1331, 100.134, 105.135, 110.138, 115.14
, 120.142, 125.143, 130.146, 135.149, 140.151, 145.153, 150.151, 155.15, 1
60.151, 165.153, 170.155, 175.155, 180.163, 185.159, 190.164, 195.171, 20
0.174, 205.175, 210.176, 215.179, 220.18, 225.178, 230.179, 235.177, 240.
178, 245.177}
```

Choose a reference temperature for the master curve (multiple of 5).

```
RefTemp=25;
```

```
RefPos=Position[Table[Mean[Transpose[TempDataLess100Hz[[i]]][2]],{
```

```
i, 74}], _?(Round[#]==RefTemp&)][[1, 1]];
```

```
ShiftFactors = {0};
```

```
Do[Δ = {};
```

```
Δ = Append[Δ, ( Transpose[Curves[[i + 1]][[2, 1]] - Transpose[Curves[[i]][[2, 2]]
Transpose[Curves[[i]][[2, 1]] - Transpose[Curves[[i]][[2, 2]] - 1 )];
```

```
Δ = Append[Δ, ( Transpose[Curves[[i + 1]][[2, 2]] - Transpose[Curves[[i]][[2, 3]]
Transpose[Curves[[i]][[2, 2]] - Transpose[Curves[[i]][[2, 3]] - 1 )];
```

```
ShiftFactors = Append[ShiftFactors, Mean[Δ] + ShiftFactors[[i]]
, {i, 73}];
```

```
ShiftFactors = ShiftFactors - ShiftFactors[[RefPos]];
```

Plot shifted Storage Modulus (Signal 3) versus Frequency (Signal 6) for each temperature.

```
q4 = {};
```

```
Do[q4 = Append[q4,
```

```
LogLinearListPlot[
Transpose[{Transpose[TempDataLess100Hz[[i]][[6]] * 10ShiftFactors[[i]],
Transposed[TempDataLess100Hz[[i]][[3]]}],
1000
```

```
PlotJoined → True,
PlotRange → All]],
```

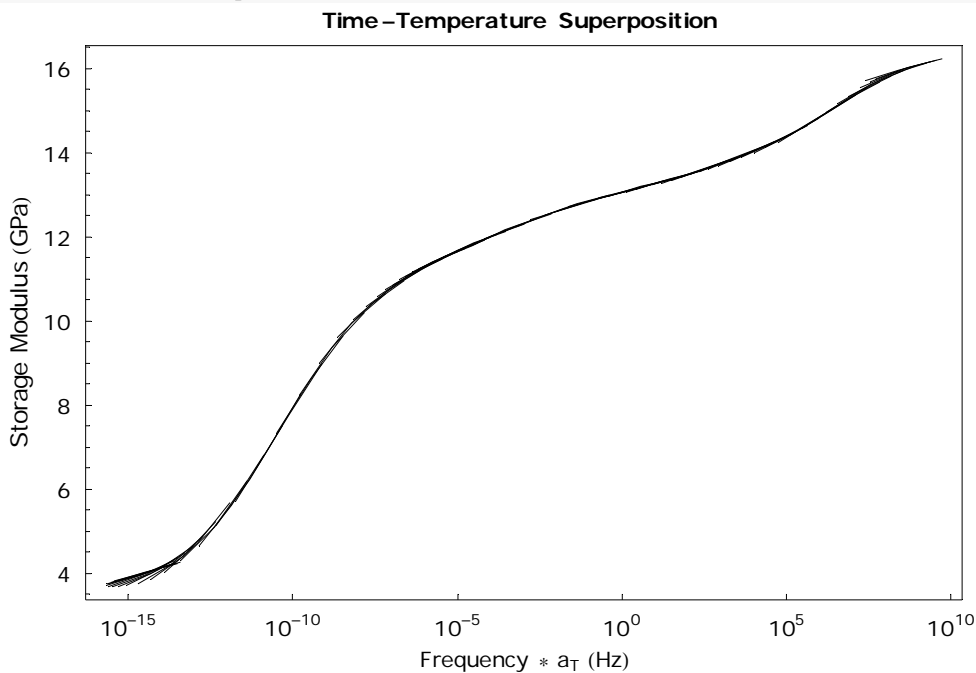
```
{i, 74}];
```

Plot master curve.

```

q5 = DisplayTogether [
  Show[Table[q4[[i]], {i, 1, Length[q4]}],
  PlotRange → All,
  PlotLabel → StyleForm["Time-Temperature Superposition", FontWeight → Bold],
  FrameLabel → {"Frequency * aT (Hz)", "Storage Modulus (GPa)"},
  FrameTicks → {{{-15, "10-15"}, {-10, "10-10"}, {-5, "10-5"}, {0, "100"},
    {5, "105"}, {10, "1010"}}, Automatic, None, None}],
  (*Show[
  Graphics[Text[TableForm[{"Ref. Temp.", "=", RefTemp, "°C"}],
    TableSpacing → {0, 1}], {-6.5 + ShiftFactors[[RefPos]], 14}]]], *)
  ImageSize → 500];

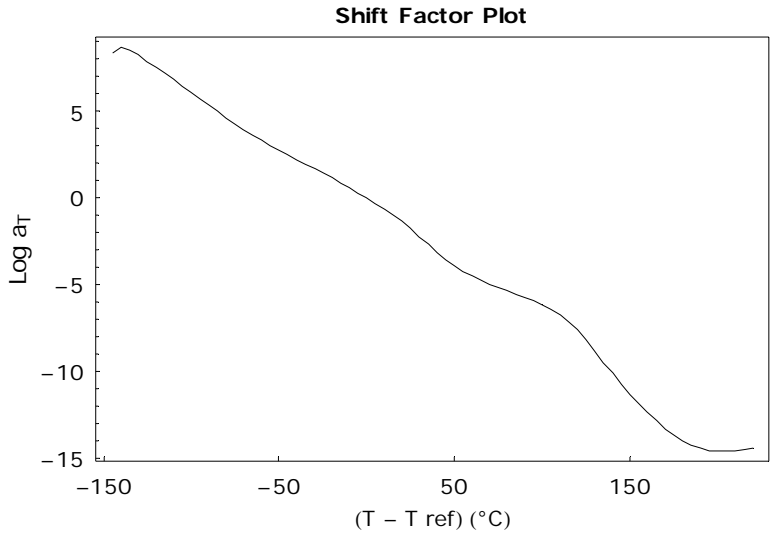
```



```

q6 = ListPlot[Transpose[{Temps - Temps[[RefPos]], ShiftFactors}],
  PlotLabel → StyleForm["Shift Factor Plot", FontWeight → Bold],
  FrameLabel → {"(T - T ref) (°C)", "Log aT"},
  FrameTicks → {{-150, -50, 50, 150, 250}, Automatic, None, None},
  PlotJoined → True,
  ImageSize → 400];

```

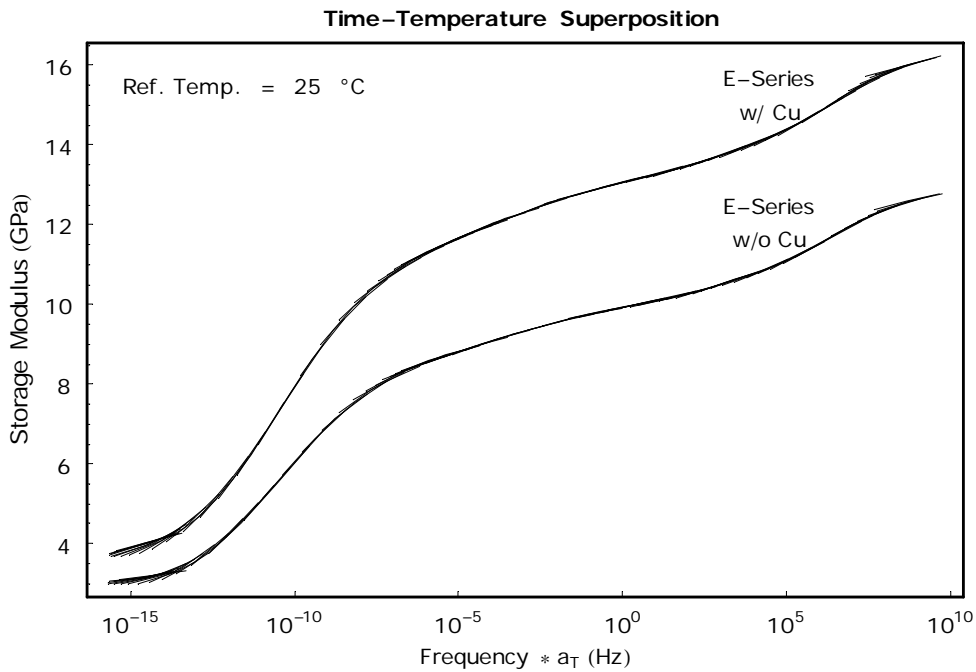


Combinded E-Series Results

```

DisplayTogether [Show [p5, q5] ,
  Show [Graphics [Text [TableForm [ { {"Ref. Temp.",
"=", RefTemp, "°C"} } , TableSpacing -> { 0, 1 } ] , { -11.5, 15.5 } ] ] ] ,
  Show [Graphics [Text [TableForm [ { {"E-Series", "w/
Cu"} , TableAlignments -> Center ] , { 4.5, 15.2 } ] ] ] ,
  Show [Graphics [Text [TableForm [ { {"E-Series", "w/o
Cu"} , TableAlignments -> Center ] , { 4.5, 12 } ] ] ] ,
  ImageSize -> 500,
  FrameStyle -> Thickness [.004] ] ;

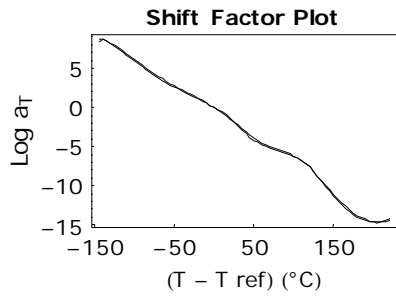
```



```

Show [p6, q6, ImageSize -> 220] ;

```



Appendix E. Surface Characterization Studies

Surface analyses were conducted on the printed circuit board materials to study their chemical makeup when they were received, after environmental conditioning, after quasi-static peel testing, and after loop peel testing. The surface testing was conducted by and through the direction of committee member, Dr. John G. Dillard, and he consequently summarized the results of those studies in several reports. These reports have been edited for continuity within the present document but remain in the most part unaltered with respect to their original forms. Reports 1 through 3 are excerpts from progress reports submitted during the first three quarters of this study. The final two sections summarize the surface analyses conducted on specimens debonded under quasi-static and low-velocity impact conditions, respectively.

E.1 Report 1

E.1.1 Introduction

Surface analysis of copper-coated circuit panels was carried out to determine the chemical composition of the surface in preparation for the adhesion studies of copper to the panels. The data obtained in these initial characterization measurements will be used as reference information in determining the failure mode in the mechanical testing experiments. Two copper-coated circuit panels were received from DuPont personnel. The panels were labeled 4N710 and Arlon 2116. It is not known what is the composition of the panels.

The surfaces were characterized using x-ray photoelectron spectroscopy (XPS). In this technique the specimen is placed in a vacuum and irradiated with soft x-rays; about 1250 eV. Irradiation of the sample causes the ejection of photoelectrons and the kinetic energy of the photoejected electrons is measured. From the energy balance equation,

$$h\nu = \text{BE (binding energy or ionization energy)} + \text{KE (kinetic energy)}$$

the value of $h\nu$ (the photon energy) is known, the value for the kinetic energy is measured, and the binding energy can be calculated. It should be recognized that materials contain different elements and that the electrons in these elements require a different amount of energy to be ionized. Thus the analysis method is sensitive to the elements present in a material and those elements can be identified from the value of the binding energy. Chemical state information can also be obtained for a given element. For example, the binding energies for carbon in different chemical combinations/states are approximately:

CH or CC; carbon singly bonded to carbon or hydrogen: 285.0 eV

C-O; carbon singly bonded to oxygen: 286.5 eV

C=O; carbon doubly bonded to oxygen: 288.0 eV

COOH or COOR; carbon in carboxyl or ester groups: 289.5 eV.

Recognizing that the binding energy can be determined to the nearest 0.1 eV, it is possible to distinguish among different carbon functionalities. The situation is similar for other elements, especially metal-containing compounds where the binding energy for the metal is greater for the metal in higher oxidation states, i.e., $\text{BE}(\text{Fe}/\text{FeC}^{\text{I3}}) > \text{BE}(\text{Fe}/\text{FeC}^{\text{I2}})$.

Another unique feature of the analytical method is that the information is obtained from about the top 5 - 10 nm (nanometers) of the material surface.

E.1.2 Preparation of Samples for Analysis

The circuit panels were cut with a band saw to obtain specimens from the copper and polymer regions of each panel. Upon visual examination of the panels, it appeared that some portions of the panels contained fingerprints or other surface contamination. To assure that the surface analysis measurements were representative of true polymer or copper surfaces, before being characterized the panel specimens were cleaned with a tissue saturated with methanol. Initial surface measurements were carried out on what appeared to be uncontaminated 4N710 polymer surfaces. To determine whether methanol cleaning altered the surface, polymer portions of the 4N710 panel were analyzed. One 4N710-polymer specimen was characterized in the as received condition, in that before analysis it was dry wiped with a lint-free tissue. The 4N710-polymer specimen was then cleaned with a methanol-saturated tissue and was characterized. The analysis results were essentially equivalent, indicating that methanol cleaning did not significantly alter the chemistry of the panel. Thus, prior to characterization measurements, all specimens were cleaned with methanol and dried in air and further cleaned by blowing a stream of argon over the surface. The specimens were mounted on 1" diameter sample probes using double stick tape. Specimens were characterized with the samples maintained at liquid nitrogen temperature (~-150°C) to reduce outgassing from the panels.

The surface analysis was carried out using a Perkin-Elmer PHI Model 5400 x-ray photoelectron spectrometer. Photoelectrons were generated by bombarding the specimens with Mg x-rays ($h\nu = 1253.6$ eV). The electron kinetic energy was determined in the hemispherical analyzer and the

binding energy for the ejected electrons was evaluated from the equation $h\nu = BE + KE$. In the measurement of the spectra, a wide scan (~0 - 1100 eV) was carried out to determine what elements were present. Then narrow scans (20 or 40 eV range) were obtained to determine more accurately the chemical nature of each element. The binding energy scale was calibrated using the C 1s photopeak attributed to background hydrocarbon; the C 1s hydrocarbon binding energy was taken as 285.0 eV. The surface concentration for each element was obtained by measuring the respective area of the photopeak for a given element, adjusting the area to account for differences in x-ray absorption and electron transmission and detection, and combining the collected modified areas to give a result in atomic percent. The atomic percent results are precise and accurate to $\pm 10\%$ of the reported value.

E.1.3 Presentation and Discussion of the Results

Representative wide-scan spectra for the polymer portions of the specimens are shown in Figure 45 for 4N710 and in Figure 46 for Arlon 2116 specimens. The principal elements on these surfaces are carbon, oxygen, silicon, and bromine. Chromium is present at a low concentration on each polymer surface. For the copper regions of the panels, wide scan spectra in Figure 47 and Figure 48 for sample 4N710 and Arlon 2116, respectively, indicate copper, carbon, and oxygen; nitrogen and bromine are present at detectable, but low levels. The surface concentration results are summarized in Table 3. The concentrations in the column Cu/Cr* indicated with an asterisk (*) pertain to concentrations of chromium. Chromium was detected only on the polymer specimens, and copper was found only on the copper samples.

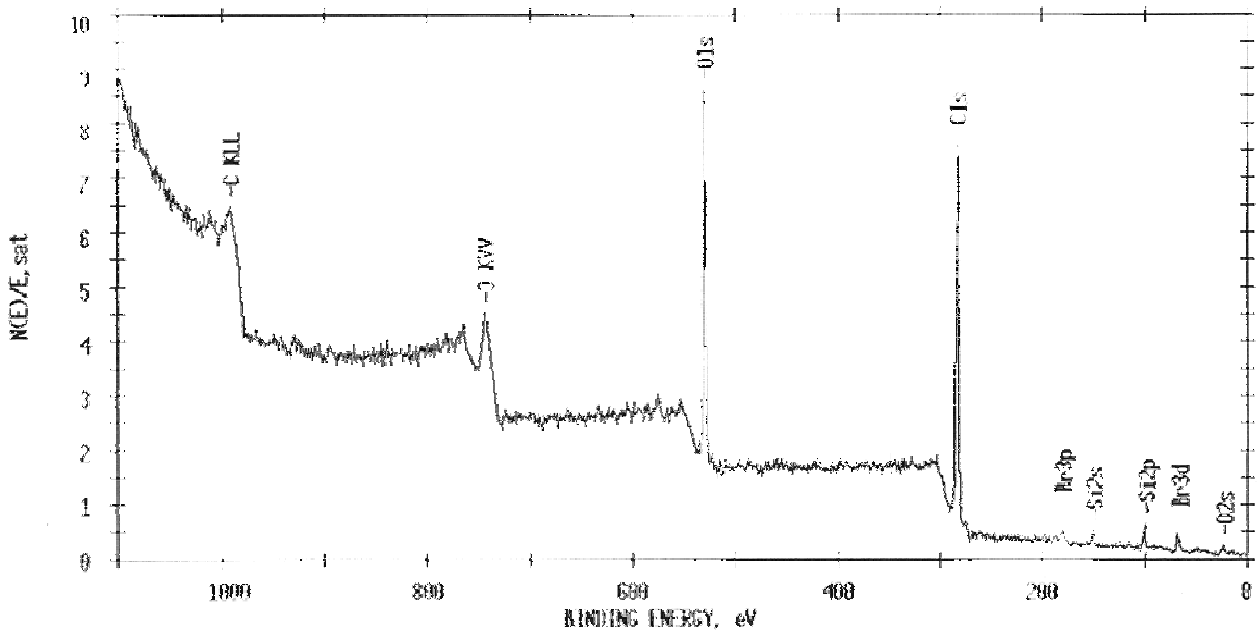


Figure 45: N710 Polymer Region MeOH Cleaned – Wide Scan

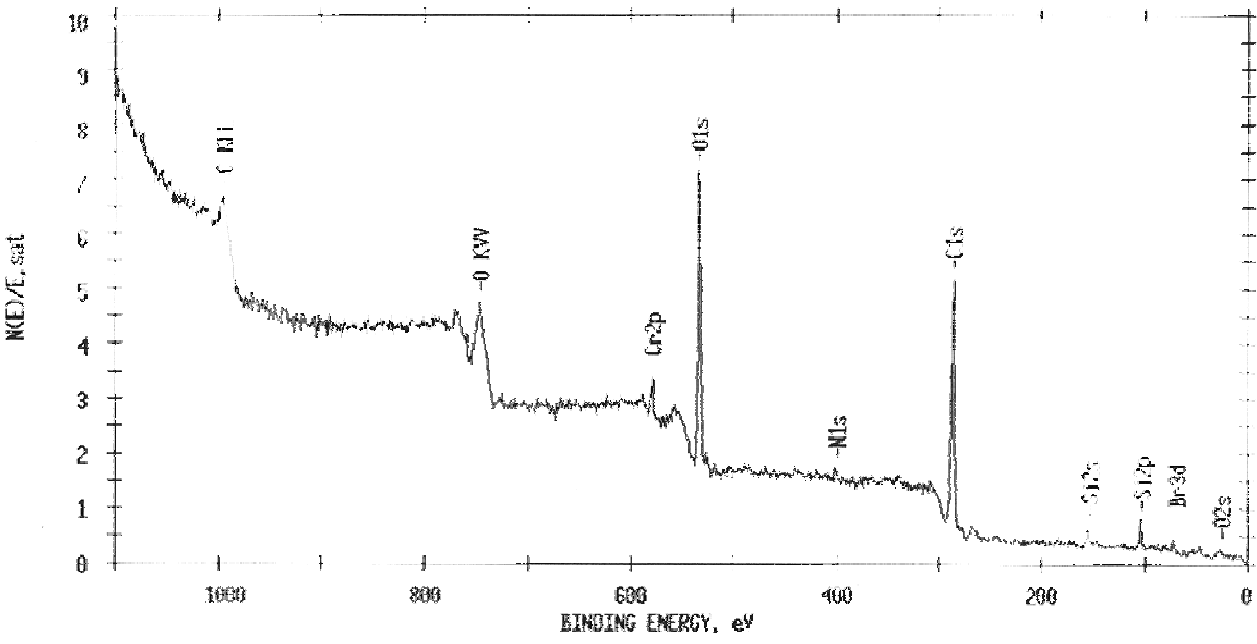


Figure 46: Arlon 2116 Polymer Region MeOH Cleaned – Wide Scan

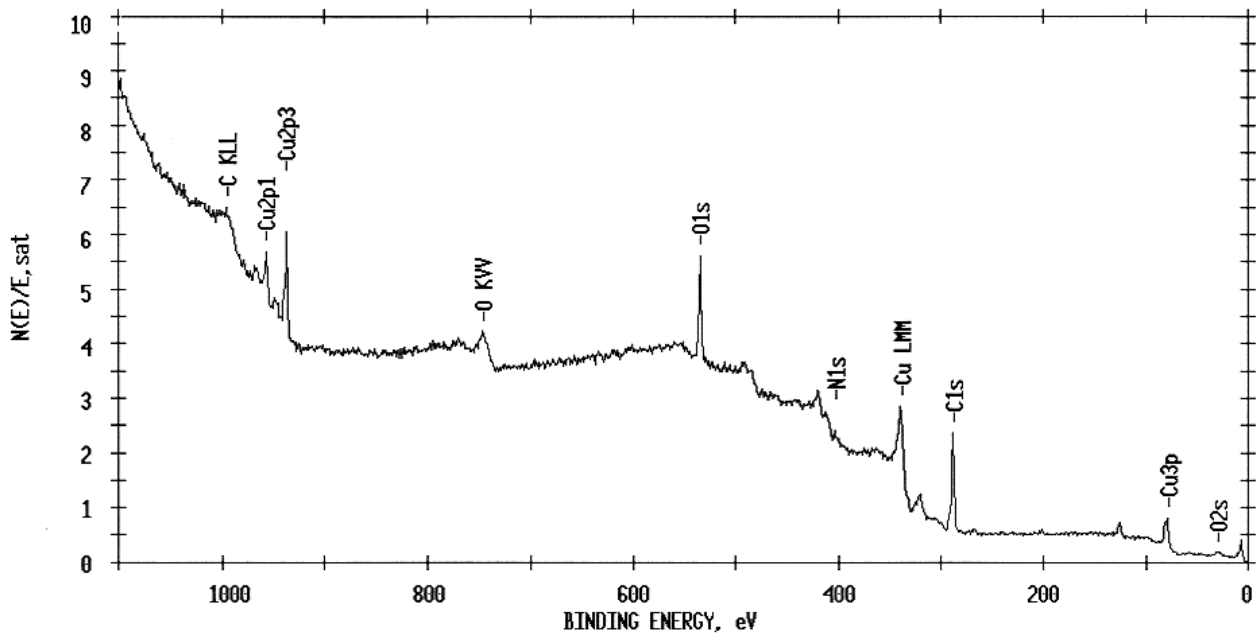


Figure 47: N710 Cu Region MeOH Cleaned – Wide Scan

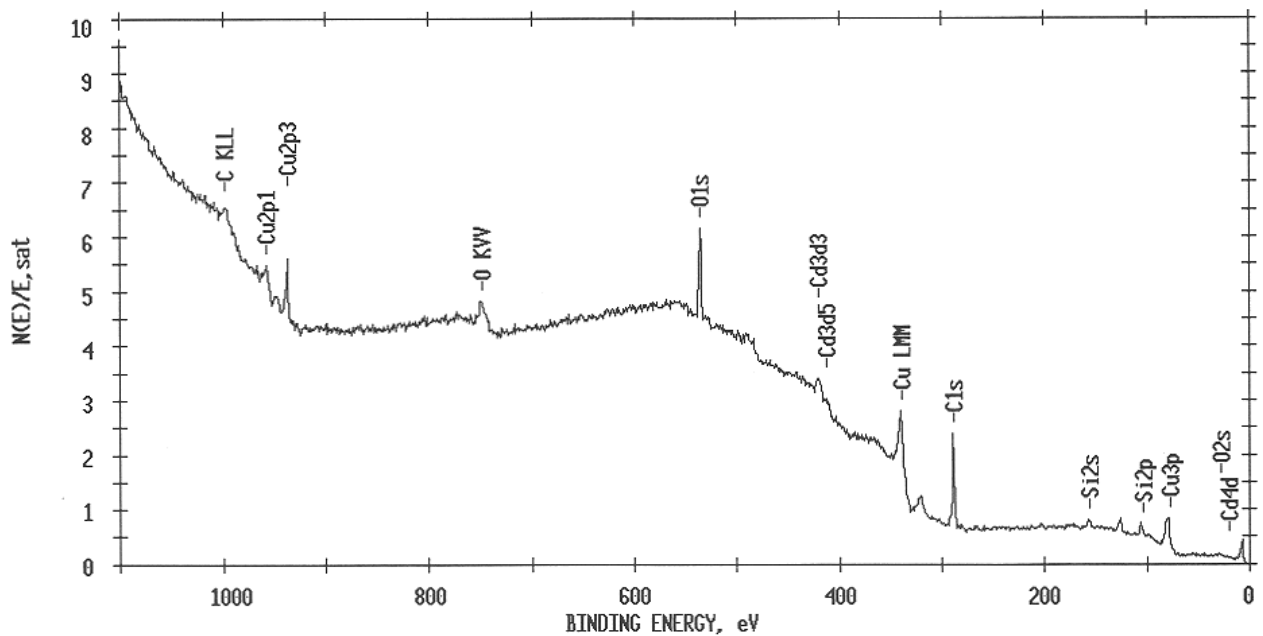


Figure 48: Arlon 2116 Cu Region MeOH Cleaned – Wide Scan

Table 3: XPS Surface Analysis Characterization of Circuit Panels (Atomic %)

Sample	C	O	N	Si	Br	Cu/Cr*
4N710 /P as rec'd	70.6	24.0	0.7	2.6	1.2	0.9*
4N710 /P MeOH clean	71.3	23.4	0.6	2.9	1.0	0.8*
4N710/Cu MeOH clean	65.0	25.7	1.7	<0.2	<0.2	7.6
Arlon2116/P MeOH clean	63.0	27.9	2.0	4.9	0.4	1.8*
Arlon2116/Cu MeOH clean	65.0	27.6	2.1	<0.2	<0.2	5.3

The concentration results for 4N710 polymer MeOH unwashed and washed indicate that methanol cleaning does not alter the chemical concentrations on the surface for the 4N710-polymer sample. This is indicated in Table 3 where the concentrations for each element are within the precision and accuracy of the measurement technique. That the chemical nature of the principal element, carbon, is not altered is evident upon comparing the C 1s spectra in Figure 49 and Figure 50, respectively, for the 4N710-polymer sample before and after the methanol wash. The C 1s spectra include contributions from hydrocarbon (C-C/C-H), carbon singly bonded to oxygen (C-O), and carboxyl carbon (-COOR). The positions in the C 1s spectra for these functional groups are highlighted in Figure 49 and Figure 50.

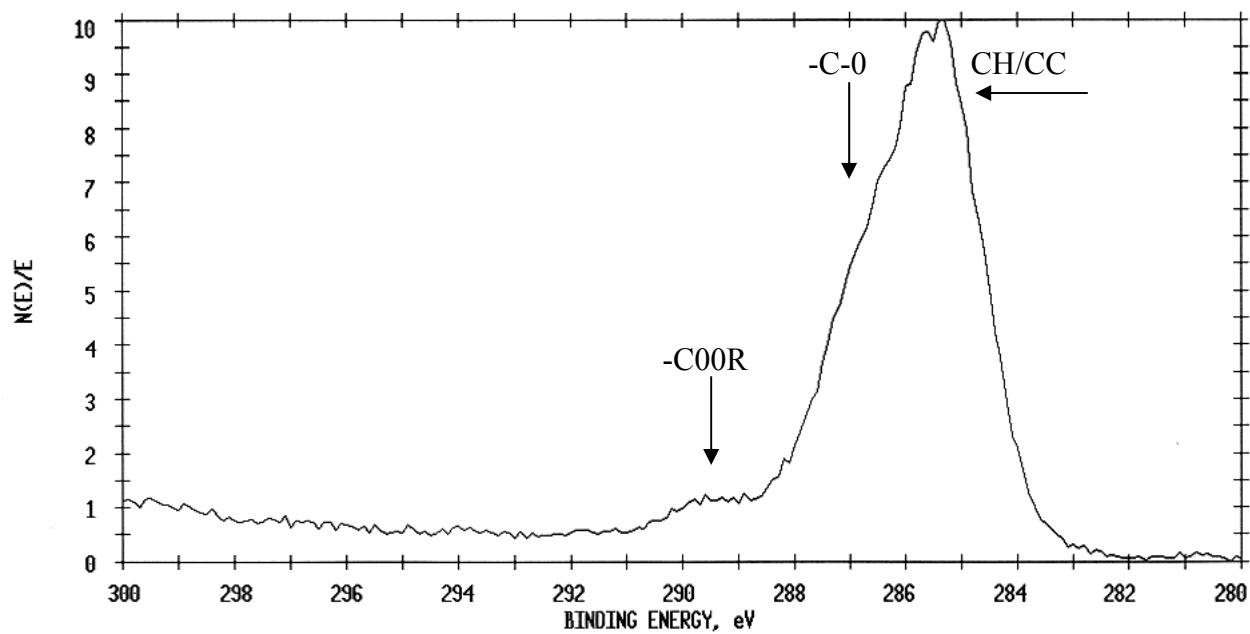


Figure 49: N710 Polymer Region As Received – C 1s

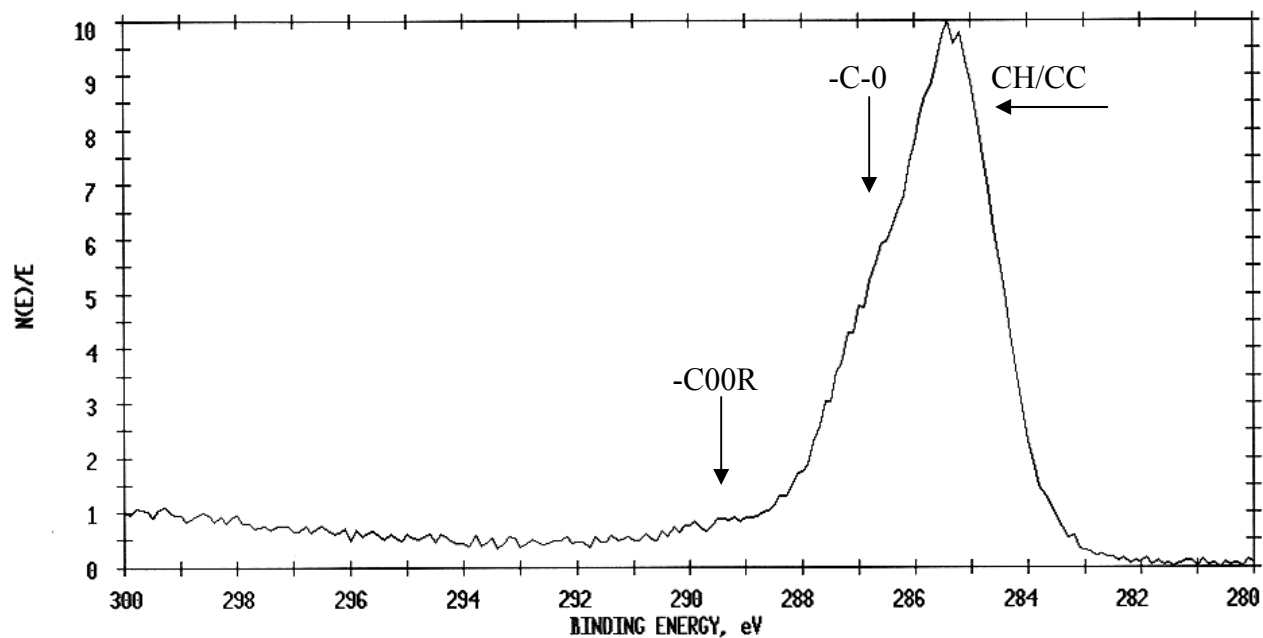


Figure 50: N710 Polymer Region MeOH Cleaned – C 1s

The results for the polymer portions of the two different panels are similar. Upon comparing the concentrations for 4N710 with Arlon 2116, it is noted that carbon and bromine are lower whereas oxygen, nitrogen, silicon and chromium are greater on the Arlon specimen. The reduction in carbon and bromine percent can be explained by recognizing that the increases, particularly in silicon and chromium, must also be accompanied by an increase in oxygen due to the chemical nature of silicon and chromium; silicate or silicone for silicon and chromium(III) oxide for chromium. These increases require that carbon and bromine decrease. While carbon decreases, the chemical nature of carbon is similar among the two samples as shown from the C 1s spectra in Figure 50 and Figure 51. In the figures, the C 1s spectra include contributions from hydrocarbon (C-C/C-H), carbon singly bonded to oxygen (C-O), and carboxyl carbon (-COOR) as discussed above for the spectrum in Figure 50.

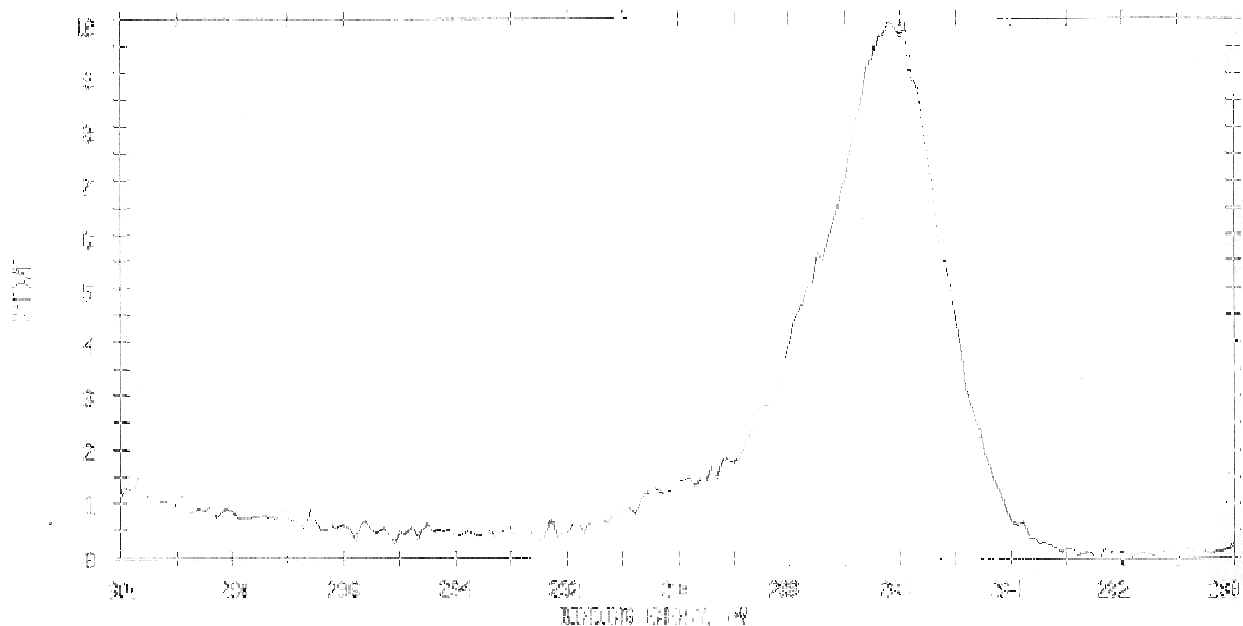


Figure 51: Arlon 2116 Polymer Region MeOH Cleaned – C 1s

The chemical composition of the copper portions of the panels is characterized by carbon, oxygen, nitrogen, and copper. The carbon spectra indicate a principal contribution from hydrocarbon carbon with smaller concentrations for carbon singly bonded to oxygen (C-O) and carboxyl carbon (-COOR). These features are evident in Figure 52 and Figure 53, respectively, where the C 1s spectra for the copper regions of the 4N710 and Arlon 2116 samples are shown. The concentration of copper is slightly greater on the 4N710 specimen, but this difference is not regarded as significant. The chemical nature of copper indicates a contribution from copper metal and oxidized copper as Cu(II). The presence of Cu(II) is evident in each Cu 2p spectrum (Figure 54 and Figure 55) by the presence of a shoulder at about 935 eV on the more intense Cu(0) metal photopeak that appears at about 933 eV.

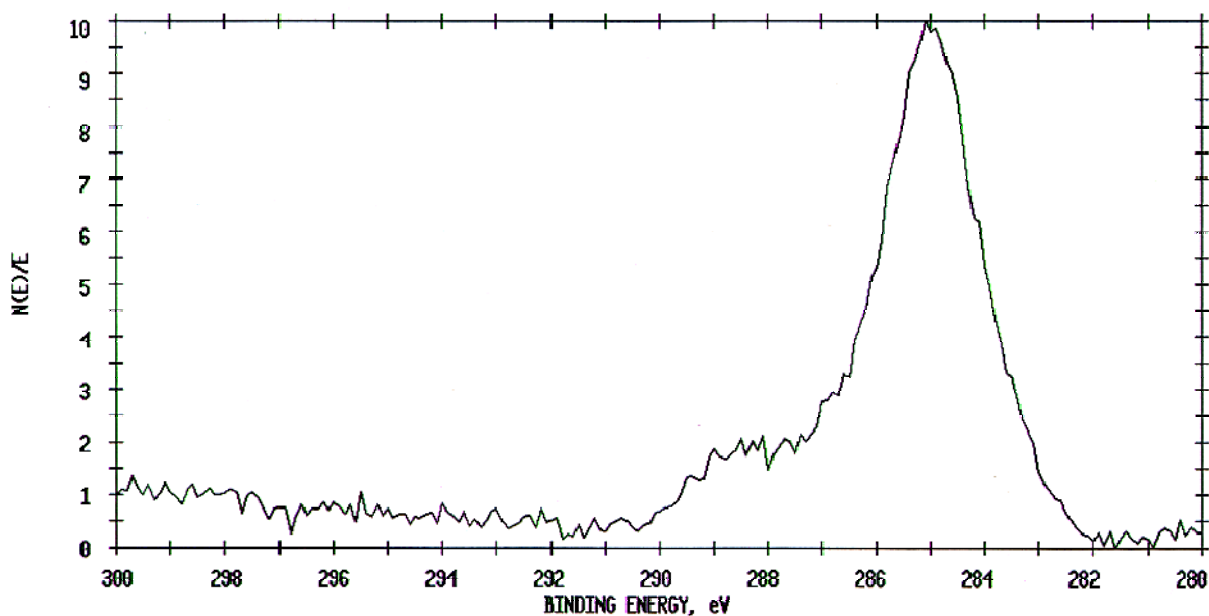


Figure 52: N710 Cu Region MeOH Cleaned – C 1s

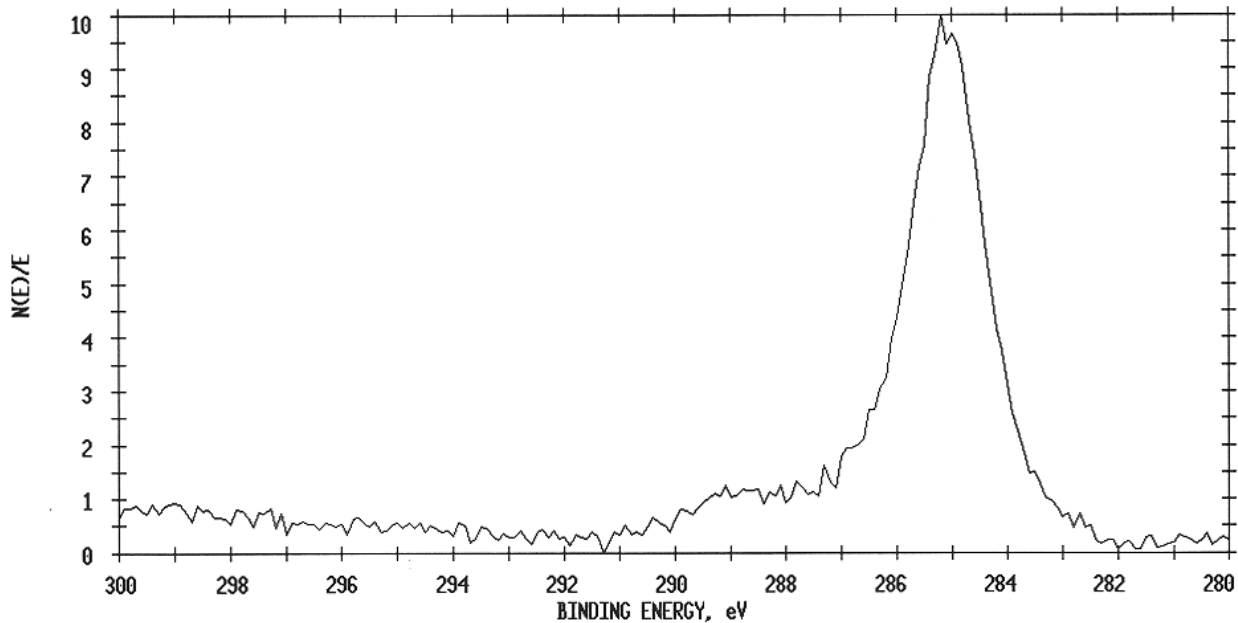


Figure 53: Arlon 2116 Cu Region MeOH Cleaned – C 1s

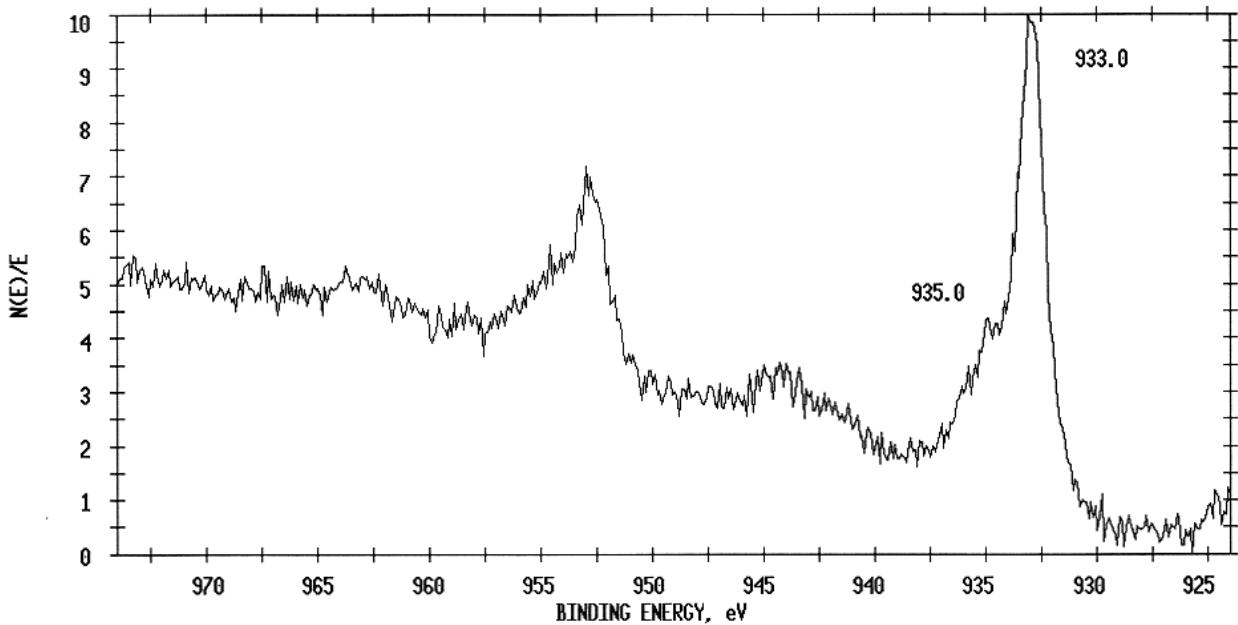


Figure 54: N710 Cu Region MeOH Cleaned – Cu 2p

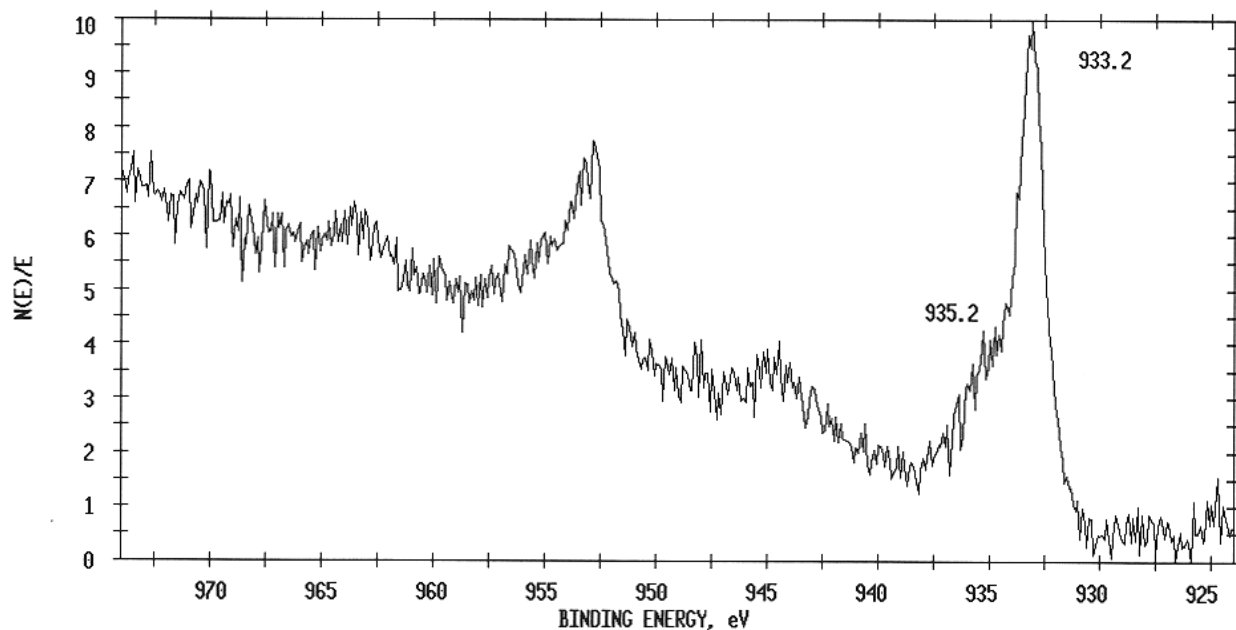


Figure 55: Arlon 2116 Cu Region MeOH Cleaned – Cu 2p

E.1.4 Summary

Surface characterization measurements have been carried out for two different circuit panels. The results indicate a composition of the polymer includes C-C/C-H, C-O, and –COOR functionalities. The polymer surfaces also contain small concentrations of bromine, silicon and chromium. The copper portions of the panels contain carbon functionalities that are similar to those detected on the polymer regions, but the distribution of the functionalities is dissimilar. Copper on the copper parts of the panels is present as elemental and oxidized copper; elemental copper dominates the chemical nature of copper in this region.

E.2 Report 2

E.2.1 Introduction

Surface analyses of failure surfaces from copper coated circuit panels were carried out to determine the chemical composition of the surfaces in the effort to determine the failure mode. Copper-coated circuit panels were received from DuPont. The panels were separated into strips

(1" X 6") for debonding studies. The specific samples studied were fiberglass (specimen number F3F) and Thermount (specimen number N2E). The specimens were debonded by gently peeling the copper strip from the composite substrate. The failure surfaces are designated as metal side and polymer side in accord with the idea that copper was peeled from the composite substrate leaving a failure surfaces of copper and substrate (polymer).

E.2.2 Experimental Approach

The failure surfaces were characterized using x-ray photoelectron spectroscopy (XPS), Scanning Electron Microscopy (SEM), and Energy Dispersive X-Ray Emission Spectroscopy (EDX). In XPS the specimen is placed in a vacuum and irradiated with soft x-rays; about 1250 eV. Irradiation of the sample causes the ejection of photoelectrons and the kinetic energy of the photoejected electrons is measured. From the energy balance equation,

$$h\nu = BE \text{ (binding energy or ionization energy)} + KE \text{ (kinetic energy)}$$

the value of $h\nu$ (the photon energy) is known, the value for the kinetic energy is measured, and the binding energy can be calculated. The composition of the surfaces is evaluated from measurements of the photopeak areas. To obtain elemental composition, in atomic percent, the peak areas are scaled using an instrumentally determined sensitivity factor. The precision and accuracy of the atomic percent determinations are approximately 10% and 10%, respectively.

In SEM an energetic (several KeV) electron beam is focused and rastered across the specimen and the back-scattered, secondary electrons are collected to generate an image of the surface. The EDX results are obtained by producing excited atomic states in the atoms as a result of the

interaction of the electron beam with the atoms in the specimen. De-excitation of the excited atoms produces x-rays whose energies are characteristic of the elements present. Because the electron beam can be rastered across the specimen, an elemental map of the surface can be obtained.

E.2.3 Results and Discussion

Wide scan XPS spectra were determined initially to establish the principal elements on the failure surfaces. The wide scan spectra for the various failure surfaces are given in Figure 56 - Figure 59. The spectra are arranged so that the metal-side failure surfaces, then polymer-side failure surfaces are given for fiberglass and then for Thermount-containing specimens.

An examination of the wide scan spectra for all four failure surfaces, indicates that the surfaces contain carbon, oxygen, copper, zinc and bromine as the dominant elements. Nitrogen was detected on the failure surfaces for the fiberglass specimens, but only at perhaps threshold or low concentrations on the Thermount sample failure surfaces.

The detailed surface composition results are presented in Table 4. First, it is of interest to note that the elemental compositions on the respective fiberglass and Thermount failure surfaces are similar. That is, the elemental composition on each of the metal failure surfaces is not significantly different than that on the corresponding polymer surface. On the other hand, the elemental percentages for nitrogen and bromine are greater on the fiberglass failure surfaces than on the Thermount surfaces. The analysis results among the same substrate failures are similar, suggesting that failure occurs within the material joining copper and the substrate. On the other hand, the differences in the composition (especially nitrogen and bromine) when comparing

fiberglass and Thermount failures, indicate a different failure mode or a different interfacial chemical composition.

E.2.3.1 Fiberglass

The compositions for the two failure surfaces for the fiberglass specimens are, within experimental error, equivalent, as noted above. The carbon 1s spectra for the two fiberglass failure surfaces (Figure 60 and Figure 61) are equivalent and are probably super imposable. The spectra are characterized by contributions from CC/CH and CO (carbon singly bonded to oxygen) functionalities, with the CC/CH group representing approximately 70% of the total carbon content. The spectra for bromine show two peaks – one which appears to be characteristic of organic bromine and one associated with inorganic bromine. The relative portions of organic:inorganic Br are approximately 90:10.

E.2.3.2 Thermount

The elemental percentages for the two failure surfaces are equal – among the dominant elements; carbon, oxygen copper, zinc, and bromine. The carbon 1s spectra shown in Figure 62 and Figure 63 indicate CC/CH and CO functionality. At the same time the contribution of CO to the total carbon is less on the polymer failure surface (This conclusion is apparent upon comparison of the relative intensities of the high binding energy shoulders in Figure 62 and Figure 63. Such results could indicate a heterogeneous failure process for the Thermount specimens.

Table 4: XPS Surface Analysis Characterization of Failure Surfaces (atomic percent)

Samp./ele.	C	O	N	Zn	Cu	Br
Metal side Fiberglass	74.4	18.4	3.2	0.9	0.8	2.3
Polymer side Fiberglass	76.6	17.0	2.9	0.4	0.5	2.6
Metal side Thermount	79.2	18.0	<0.1	0.9	0.6	1.3
Polymer side Thermount	81.9	15.5	0.4	0.3	0.4	1.5

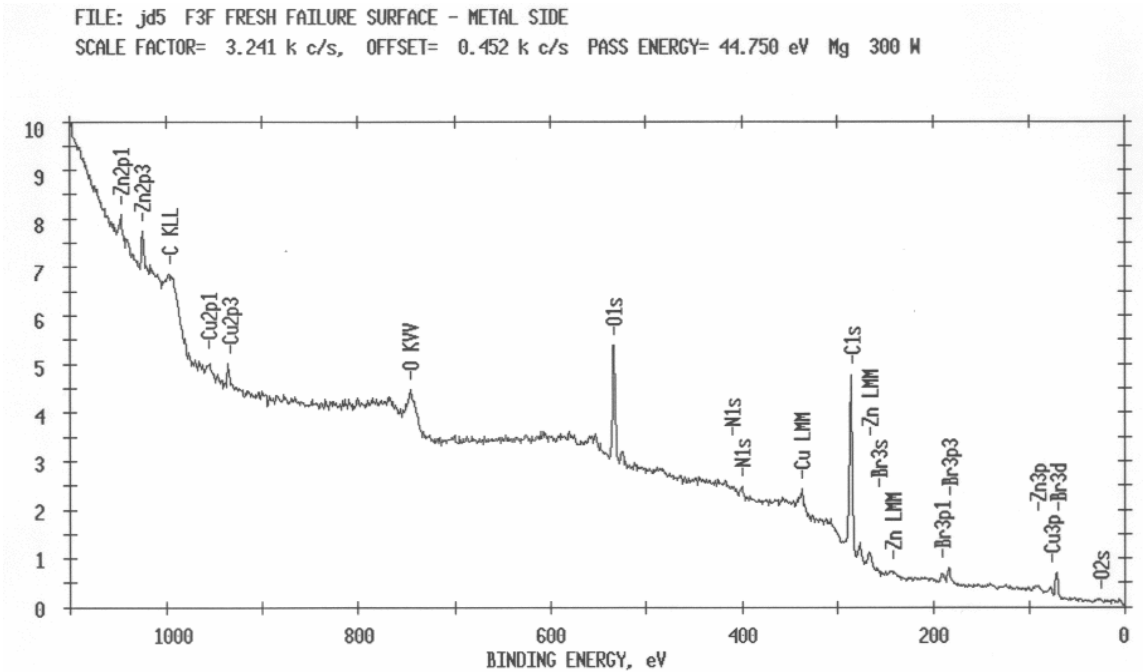


Figure 56: Wide Scan of Metal-Side Failure Surface – Fiberglass-Copper

FILE: jd7 F3F FRESH FAILURE SURFACE - FIBERGLASS SIDE
 SCALE FACTOR= 2.862 k c/s, OFFSET= 0.328 k c/s PASS ENERGY= 44.750 eV Mg 300 W

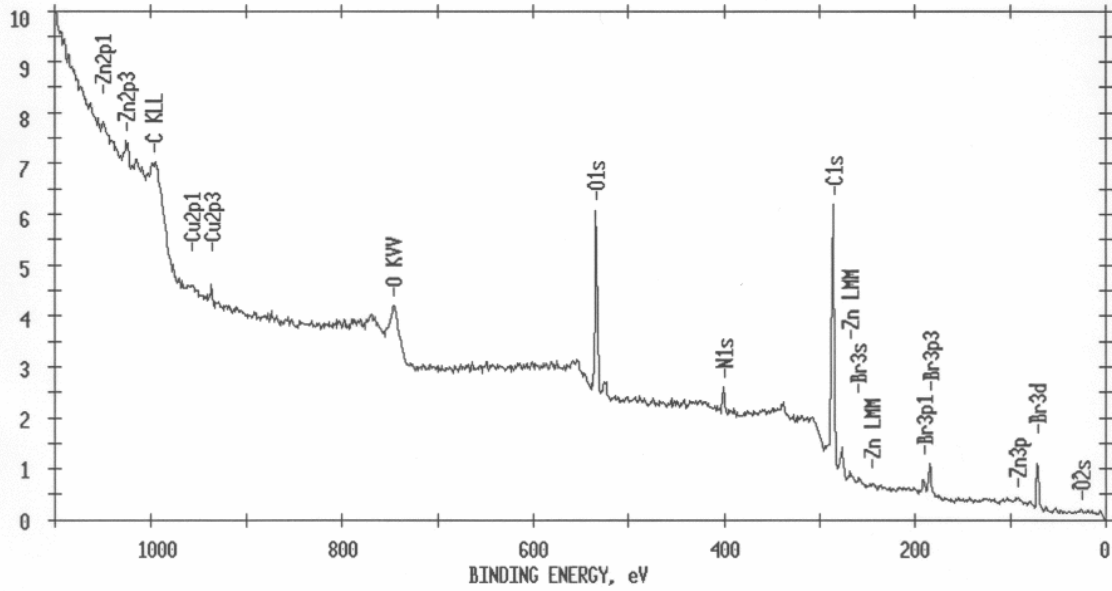


Figure 57: Wide Scan of Polymer-Side Failure Surface – Fiberglass-Copper

FILE: jd1 N2E FRESH FAILURE SURFACE - METAL SIDE
 SCALE FACTOR= 3.592 k c/s, OFFSET= 0.444 k c/s PASS ENERGY= 44.750 eV Mg 300 W

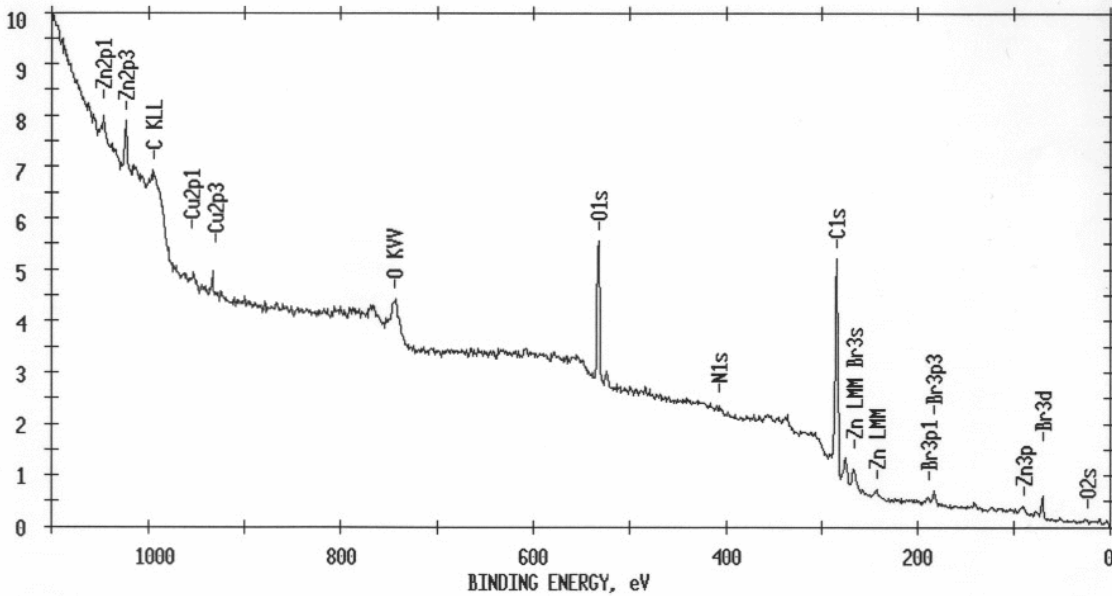


Figure 58: Wide Scan of Metal-Side Failure Surface – Thermount-Copper

FILE: jd3 N2E FRESH FAILURE SURFACE - THERMAMOUNT SIDE
SCALE FACTOR= 2.728 k c/s, OFFSET= 0.265 k c/s PASS ENERGY= 44.750 eV Mg 300 W

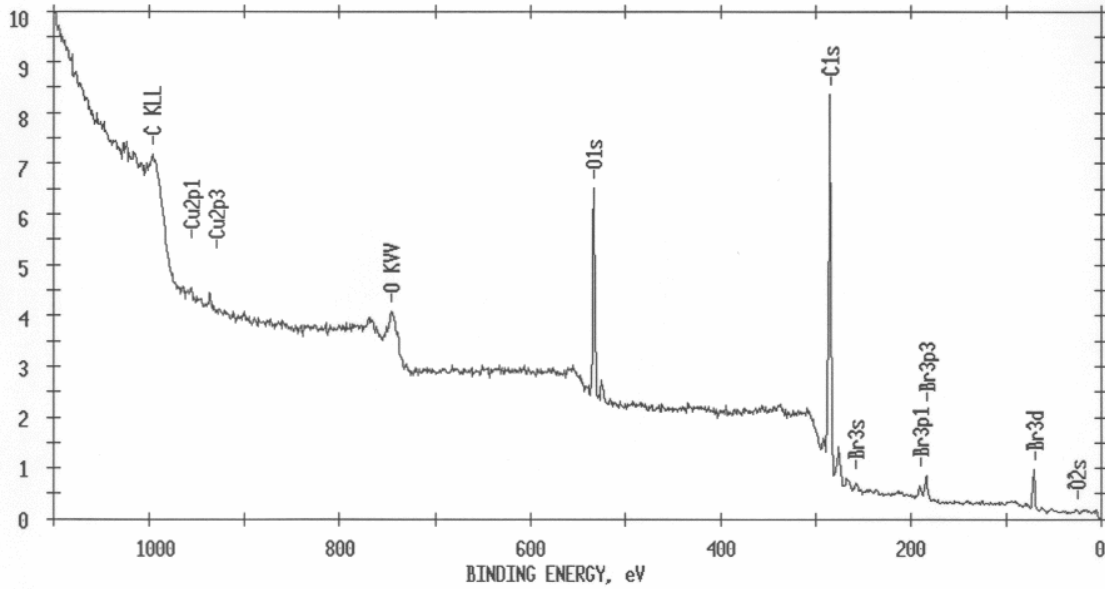


Figure 59: Wide Scan of Polymer-Side Failure Surface – Thermount-Copper

FILE: jd6 F3F FRESH FAILURE SURFACE - METAL SIDE
SCALE FACTOR= 0.452 k c/s, OFFSET= 1.179 k c/s PASS ENERGY= 17.900 eV Mg 300 W

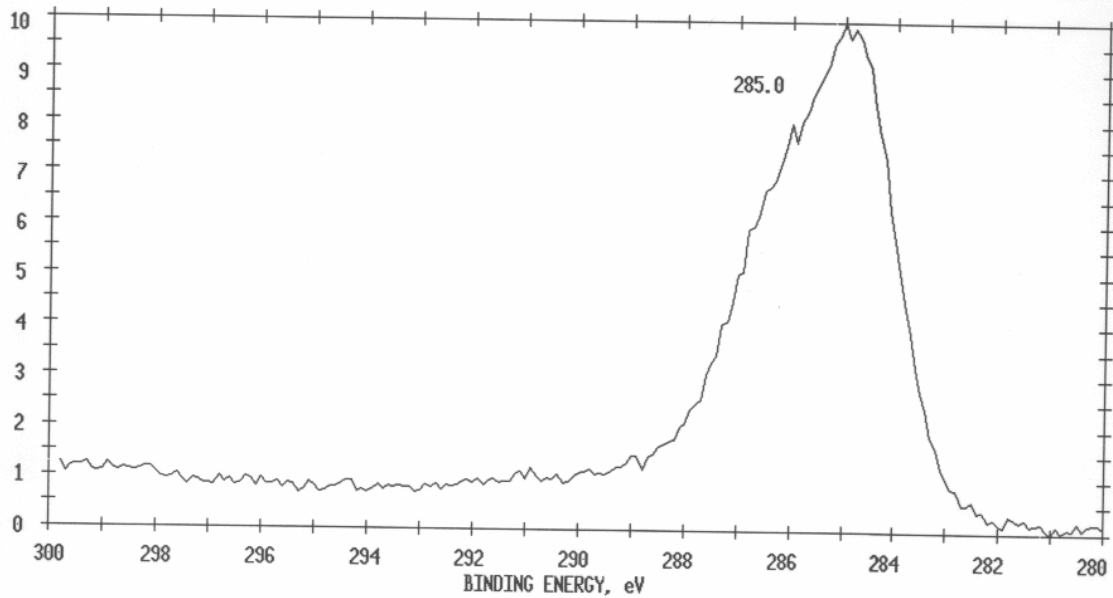


Figure 60: C 1s Spectrum of Metal-Side Failure Surface – Fiberglass-Copper

FILE: jd8 F3F FRESH FAILURE SURFACE - FIBERGLASS SIDE
SCALE FACTOR= 0.574 k c/s, OFFSET= 0.974 k c/s PASS ENERGY= 17.900 eV Mg 300 W

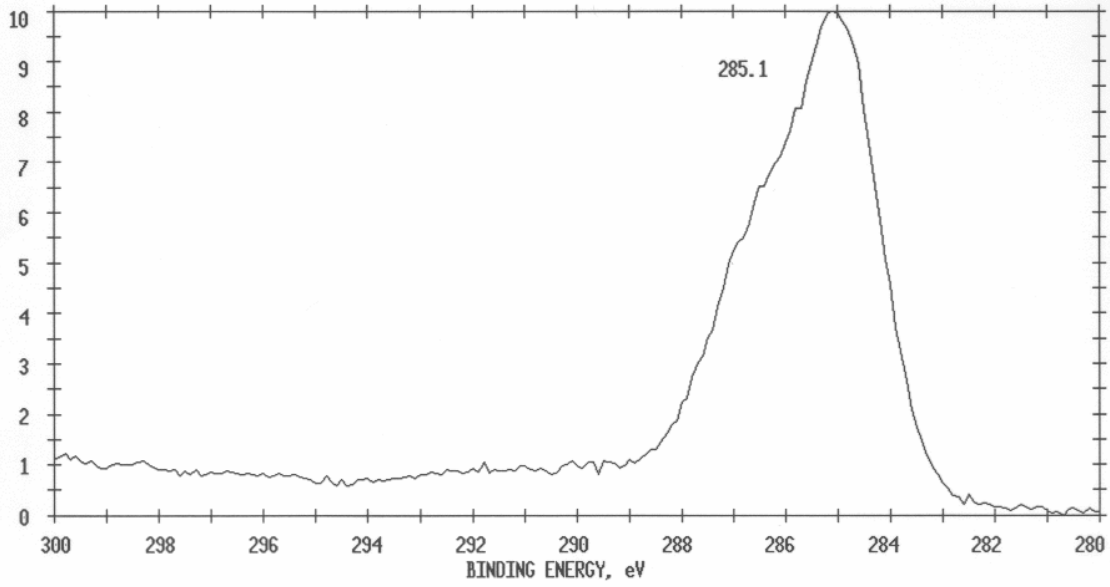


Figure 61: C 1s Spectrum of Polymer-Side Failure Surface – Fiberglass-Copper

FILE: jd2 N2E FRESH FAILURE SURFACE - METAL SIDE
SCALE FACTOR= 0.551 k c/s, OFFSET= 1.256 k c/s PASS ENERGY= 17.900 eV Mg 300 W

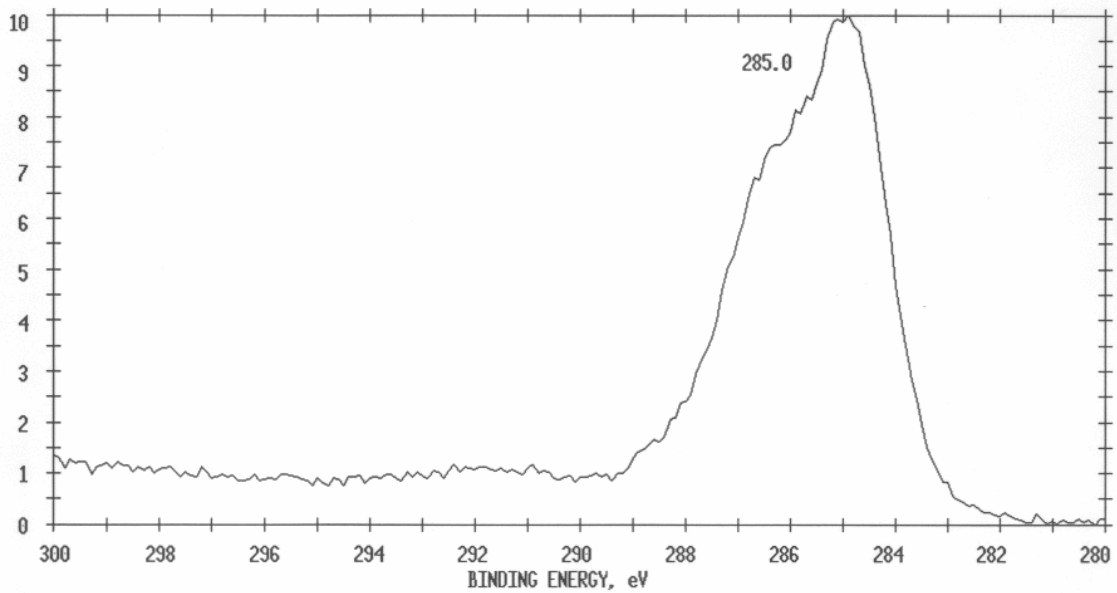


Figure 62: C 1s Spectrum of Metal-Side Failure Surface – Thermount-Copper

FILE: jd4 N2E FRESH FAILURE SURFACE - THERMAMOUNT SIDE
SCALE FACTOR= 0.744 k c/s, OFFSET= 0.799 k c/s PASS ENERGY= 17.900 eV Mg 300 W

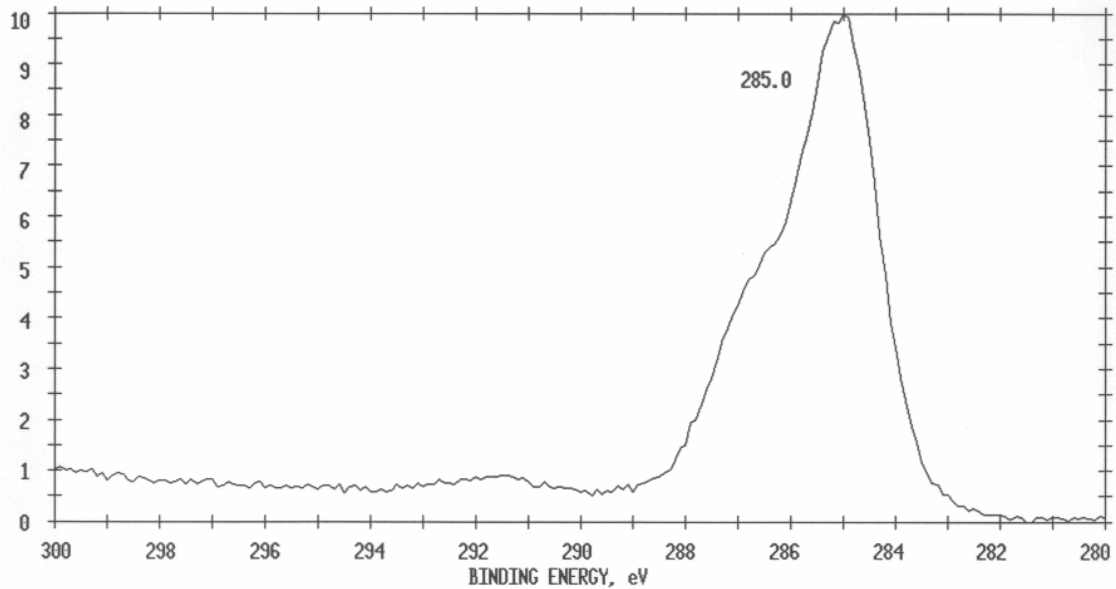


Figure 63: C 1s Spectrum of Polymer-Side Failure Surface – Thermount-Copper

SEM/EDX measurements results are presented in the SEM/EDX photographs in Figure 64 - Figure 67. In these figures the upper figure is the SEM of a particular failure surface and below is the EDX elemental map. For the metal failure surfaces the elements copper, zinc, bromine, and oxygen (clockwise in the photos) were mapped. The elements copper, carbon, bromine and oxygen (clockwise in the photos) were mapped for the polymer failure surfaces. Interestingly, the SEM photomicrographs indicate similar topographies, respectively, for the metal and for the polymer surfaces.

The topography of the metal-side failure surfaces shows particulate-like or nodule-like features suspended on a background of smooth material (Figure 64 and Figure 66). It seems that the smooth material arises in part as a result of tearing in the failure process. The EDX results for the metal failure surfaces indicate a “dotted” pattern for copper, zinc, and oxygen. It is reasonable

that the “dots” correspond to the location of the particles of copper and zinc or their metal oxides – although the XPS results indicate that copper is present in the elemental form.

The polymer-side failure surfaces shown in Figure 65 and Figure 67, exhibit wave-like features with particulate matter embedded in what appears to be an elastic or viscoelastic material. The EDX maps show well-defined regions (dots) for copper and more dispersed regions for zinc and oxygen. Upon comparison of the particle pattern from the SEM with the EDX maps, the particle locations in the SEMs appear to coincide with the copper locations in the EDX maps. It is noteworthy that the copper EDX pattern is well defined and suggests that large particles of copper are removed in the failure processes. The EDX maps for bromine show regions of high bromine concentration. It is perhaps noteworthy that bromine appears to be more highly concentrated on the polymer-side failure surfaces compared to the metal-side failures – although the XPS results indicate near equivalence in bromine concentrations on the respective metal-polymer failure surfaces. An explanation for this apparent discrepancy may lie in the difference in surface sensitivity noted above.

The SEM/EDX findings suggest tearing of material in a kind of “cohesive” process in these debonding processes. The process also results in the formation of copper clusters on the polymer surfaces. It is also possible that the copper clusters could arise in the tearing process. Thus the failure does not proceed via a homogeneous debonding of the material even though the XPS results suggest equivalent failure surfaces among the fiberglass and Thermount specimens, respectively.

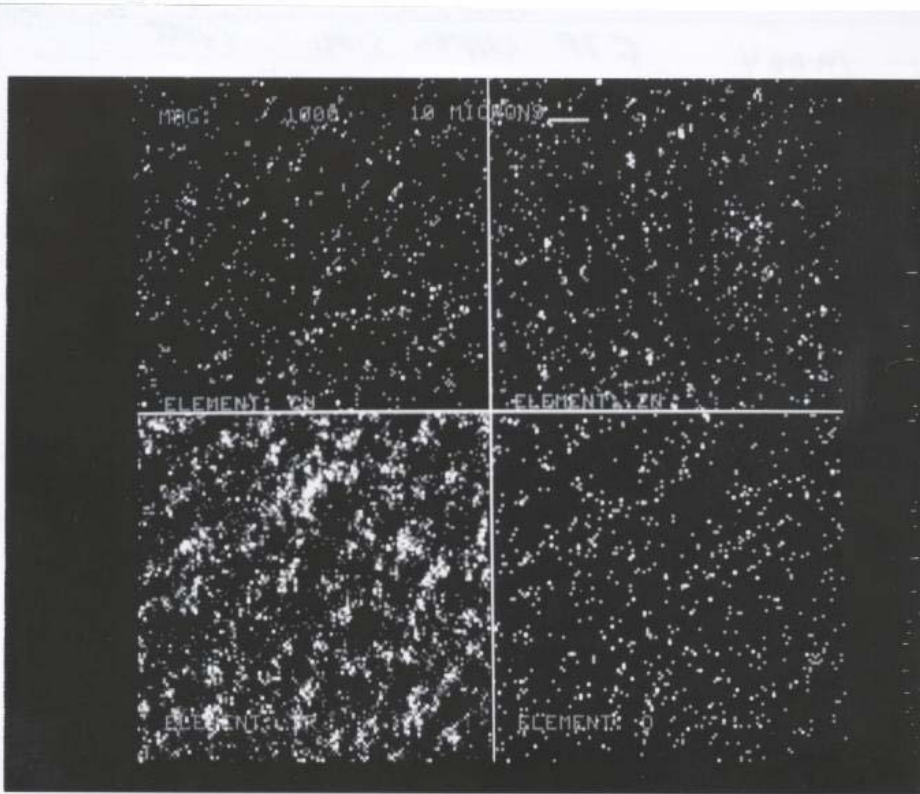
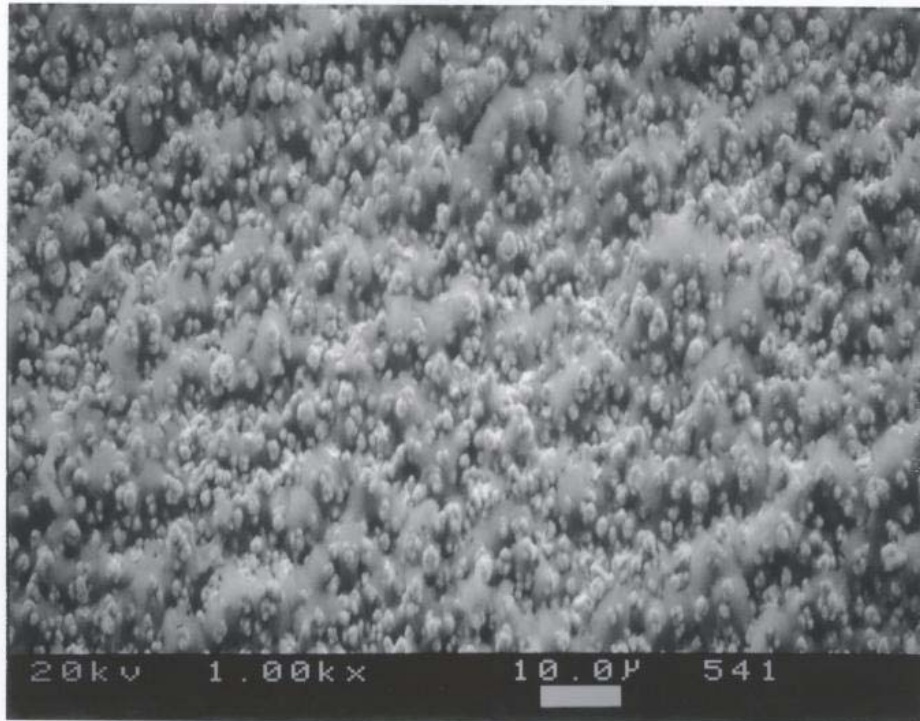


Figure 64: SEM/EDX: Fiberglass-Metal-Side

EDX:

Cu Zn
Br O

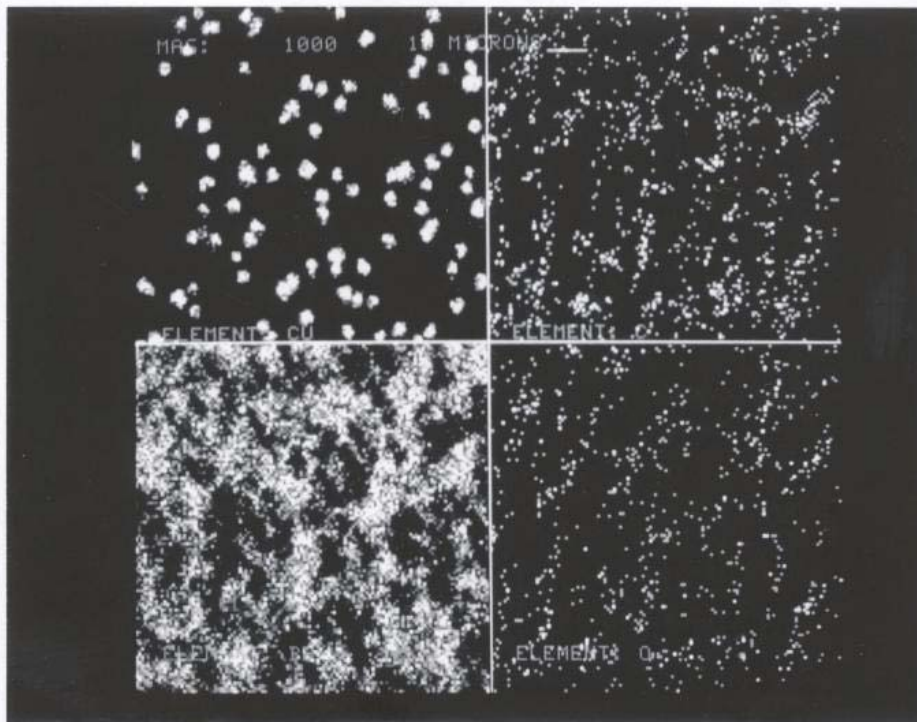
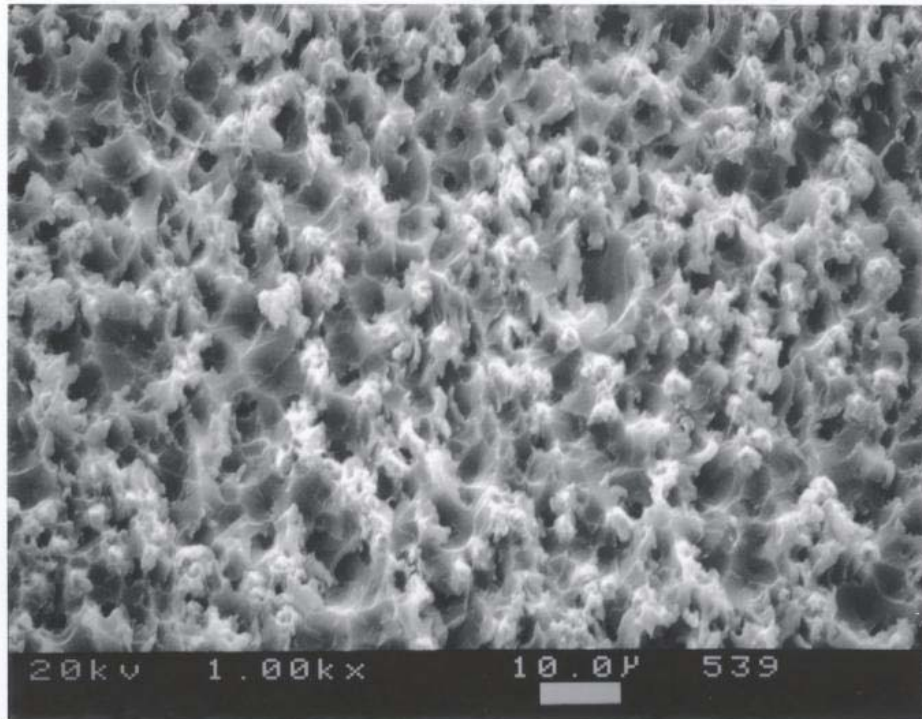


Figure 65: SEM/EDX: Fiberglass-Polymer-Side EDX: **Cu** **C**
Br **O**

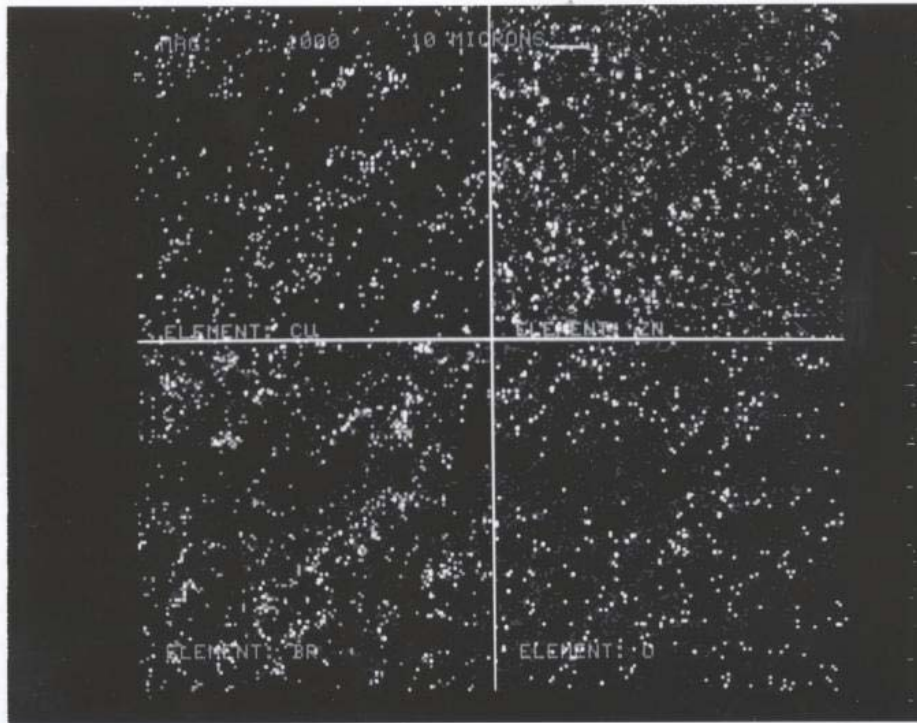
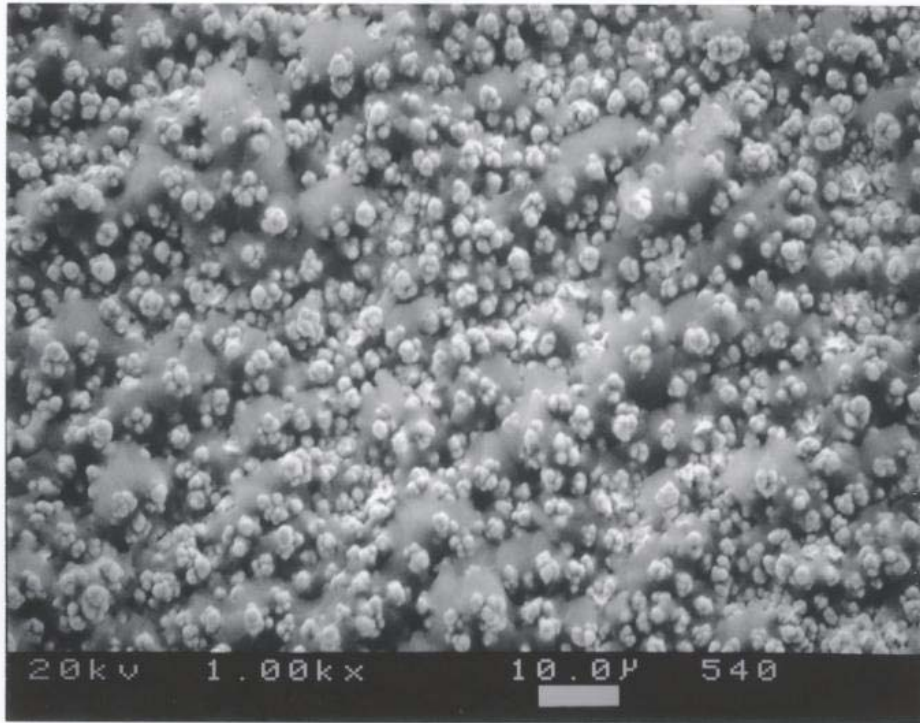


Figure 66: SEM/EDX: Thermont-Metal-Side EDX: **Cu Zn**
Br O

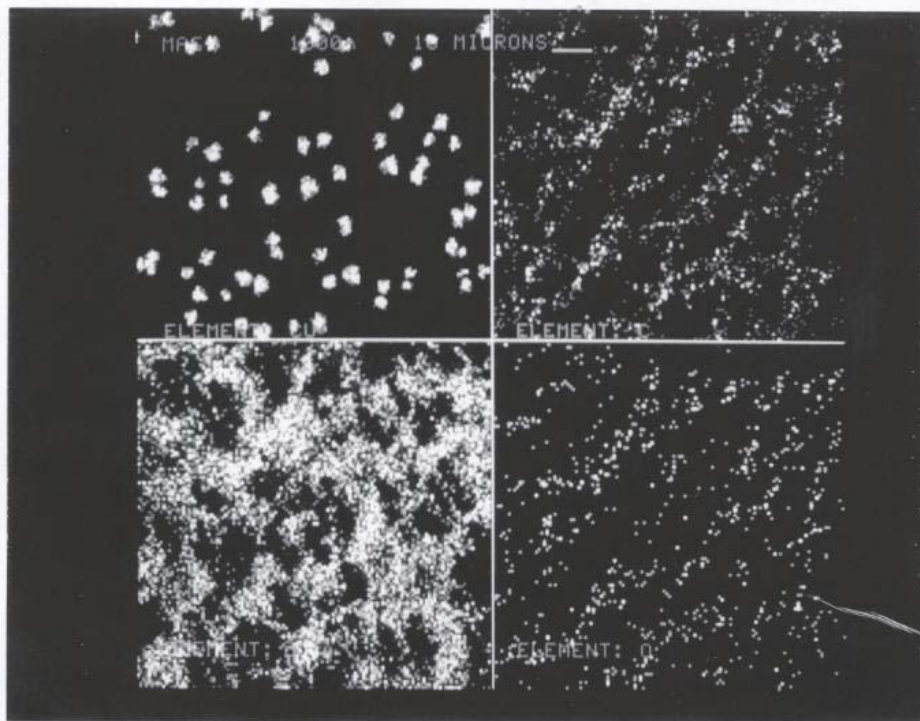
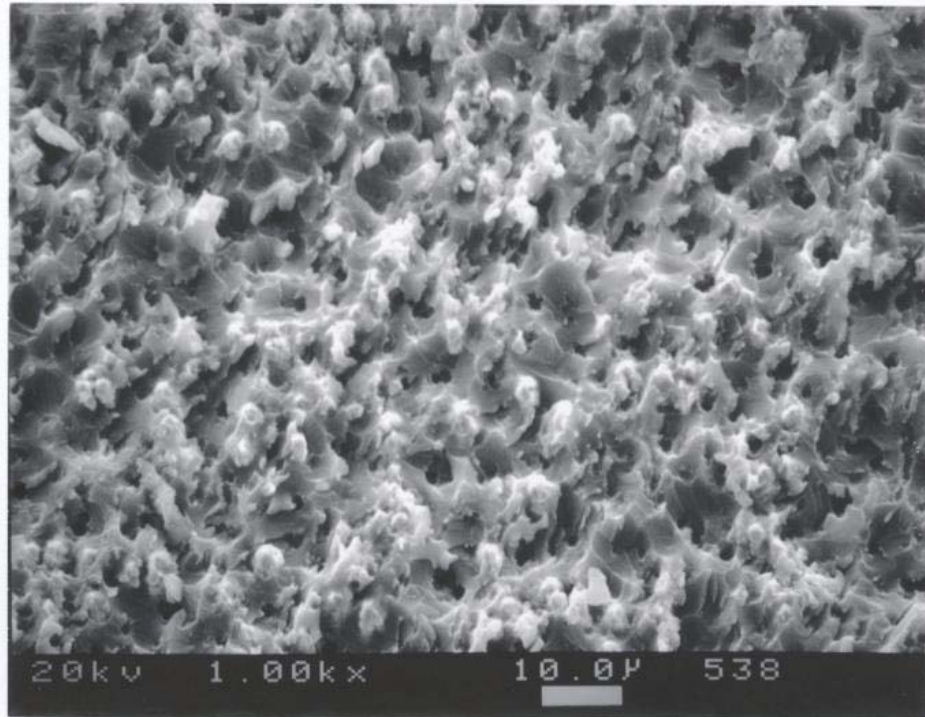


Figure 67: SEM/EDX: Thermonat-Polymer-Side EDX: $\begin{matrix} \text{Cu} & \text{C} \\ \text{Br} & \text{O} \end{matrix}$

E.2.4 Summary

Surface characterization measurements using XPS, SEM, and EDX have been carried out following the debonding of two different copper-coated composite materials. The materials tested were a fiberglass and Thermount. The results indicate a heterogeneous failure process where copper clustering is noted on the polymer-side failure surfaces, and tearing appears to occur at the substrate copper interface.

E.3 Report 3

E.3.1 Introduction

Studies have been initiated on the kinetics and chemical aspects of the degradation, debonding of copper-coated fiberglass and Thermount specimens upon exposure to 100% RH at 70°C. The conditions were selected in the attempt to “accelerate” the aging process. Specimens were removed from exposure conditions and characterized via XPS. The points of interest in these studies include 1) determining the changes in copper and polymer chemistry as a function of exposure and time, 2) establishing the manner of debonding under these environmental exposure conditions, 3) measuring the rate at which debonding-delamination takes place, and 4) determining the failure mode for the debonding processes. These debonding results are to be compared with the findings for “dry” delamination events – pulling the copper film from the composite substrates at room temperature. In the current experiments, copper-coated specimens, under no stress, are suspended in water vapor (100% RH) at 70°C, and the delamination process is followed. The initial results are reported herein.

E.3.2 Experimental Approach

DuPont provided copper-coated fiberglass- and Thermount-based circuit panel. The panels were cut into strips (1" X 5") such that one wide (~1/4") and one thin (~1/32") strip of copper were present on the panels. The specific samples studied were fiberglass (specimen number F3F) and Thermount (specimen number N2E). After about 75 hrs of exposure, samples were removed from the water vapor environment and the surfaces were characterized using x-ray photoelectron spectroscopy (XPS), as describe in previous reports. The copper and the polymeric regions of the specimens were characterized.

E.3.3 Results and Discussion

Following exposure of the circuit specimens to 100%RH at 70°C for only about 75 hours, no delamination of copper from the substrate (composite) material was noted. However, the surface appearance of copper has changed. The appearance of the composite surfaces has not visually changed, and no delamination in either of the composite substrates has been observed. The surface analysis results provided further understanding of the changes in surface chemistry, particularly for copper, in these tests. Two regions of each specimen were analyzed – the copper and the polymer regions for each material.

The wide-scan spectra of the copper regions for the Cu-F (copper- fiberglass) and for the Cu-T (copper-Thermount) samples indicate that the surfaces contain carbon, oxygen, and copper. A low intensity peak for nitrogen is also noted. Tin and cadmium are identified by the XPS computer system in these figures, but the peaks are due to Auger processes involving copper. The detailed surface composition results are presented in Table 5. The principal result is that exposure to the 100%RH/70°C conditions does not change the carbon or oxygen content

significantly – with the exception that carbon increases and oxygen decreases for the polymer region of the fiberglass sample. This difference is probably due to the removal of chromium from this surface in the exposure experiments. Examination of the C 1s spectra for the polymer region for each of the composite specimens before and after exposure indicates that the chemical nature of carbon is unchanged as a result of the 100%RH/70°C exposure. The nitrogen content changes in an irregular manner, but the determination of nitrogen is complicated by the fact that the N 1s peak that is used to calculate the percentage, overlaps to some extent with the copper Auger peak. So the changes in nitrogen content are not viewed with importance. The principal chemical changes occurred for copper – it is interesting to note that the copper concentration increases for the fiberglass sample and decreases (modestly) for the Thermount sample, following exposure to the 100%RH/70°C conditions.

Table 5: XPS Surface Analysis Characterization of Specimens Surfaces: Following Exposure to 100% RH at 70°C 75 hrs: (first line); and for as received samples: (second line – from 1st quarterly report) results in atomic %

Samp./ele.	C	O	N	Cu	Si	Br
Cu region	61.4	26.5	4.1	5.9	2.1	<0.2
Thermount	65.0	25.7	1.7	7.6	<0.2	<0.2
Polymer region	73.7	21.7	1.6	<0.2	3.0	<0.2
Thermount*	71.3	23.4	0.6	<0.2	2.9	1.0
Cu region	67.8	24.0	<0.5	8.2	<0.2	<0.2
Fiberglass	65.0	27.6	2.0	5.3	<0.2	<0.2
Polymer region	72.6	20.6	1.3	<0.2	4.2	<0.2
Fiberglass**	63.0	27.9	2.0	<0.2	4.9	<0.2

*chromium also present at ~ 0.8% and ** at ~ 1.3%.

Of more interest is the fact that the chemical nature of copper changes. These alterations are illustrated in Figure 68 - Figure 71 where the Cu 2p spectra for copper on the methanol cleaned as received surfaces (Figure 68 and Figure 70), are compared with those for copper after

environmental exposure (Figure 69 and Figure71). The significant result is that copper (Cu^0) is converted to oxidized copper (Cu^{2+}). That Cu^{2+} is produced rather than Cu^+ is supported by the presence of the small, broader peaks on the high binding energy side of the two main Cu 2p peaks. These broad features are shake-up satellite peaks and are prominent in paramagnetic metal ions. In this case, Cu^{2+} is a paramagnetic d9 metal ion whereas Cu^+ is a d10 diamagnetic ion. For copper on Thermount (Figure 69), the sharp feature on lower binding energy side of the Cu $2p^{3/2}$ peak is due to Cu^0 (elemental copper) or Cu^+ (oxidized copper). It is not possible to distinguish Cu^0 from Cu^+ from the position of the peaks, i.e., from the binding energies alone. The Cu 2p spectra for the Cu-fiberglass region (Fig. 4) suggest that only oxidized metal is present. An explanation of the differences in the extent of oxidation is not suggested at this time. Analysis of additional samples and for samples maintained at longer exposure times may provide information that will aid in formulating an explanation for this observation.

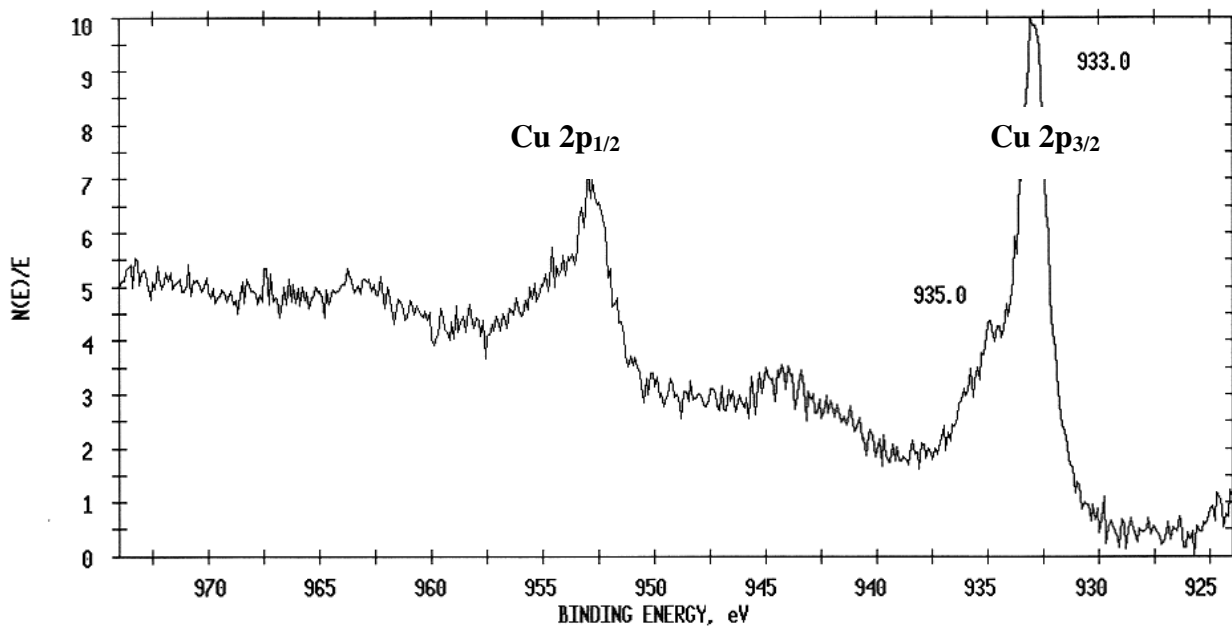


Figure 68: Thermount Cu Region MeOH Cleaned (as received) – Cu 2p

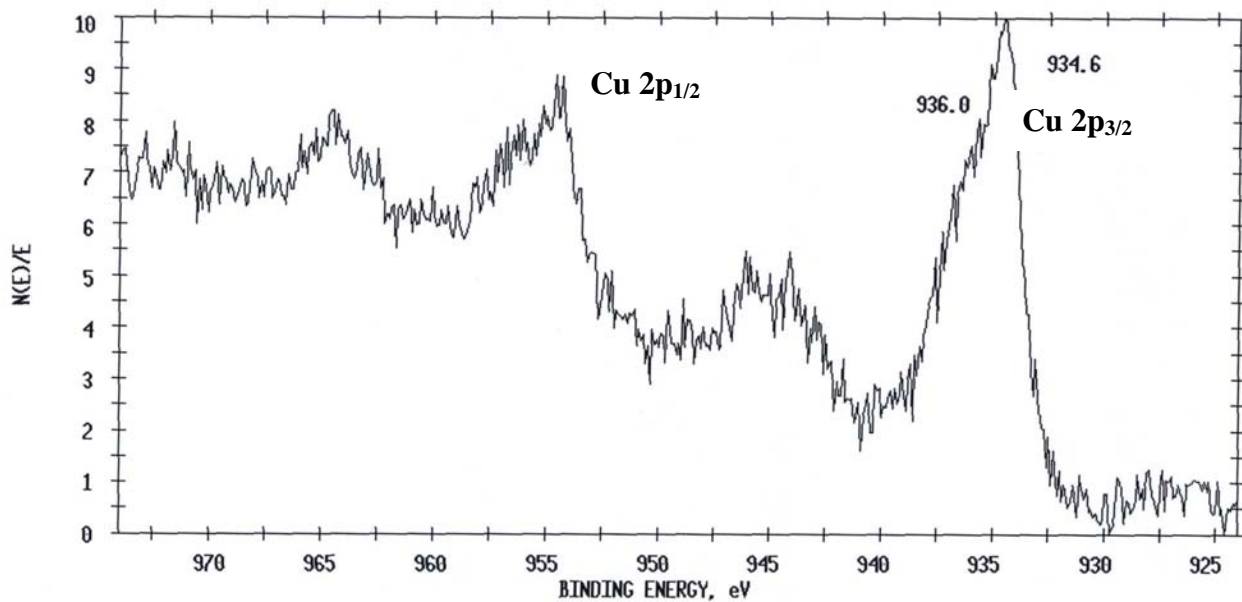


Figure 69: Thermount Cu Region 100RH & 70°C – Cu 2p

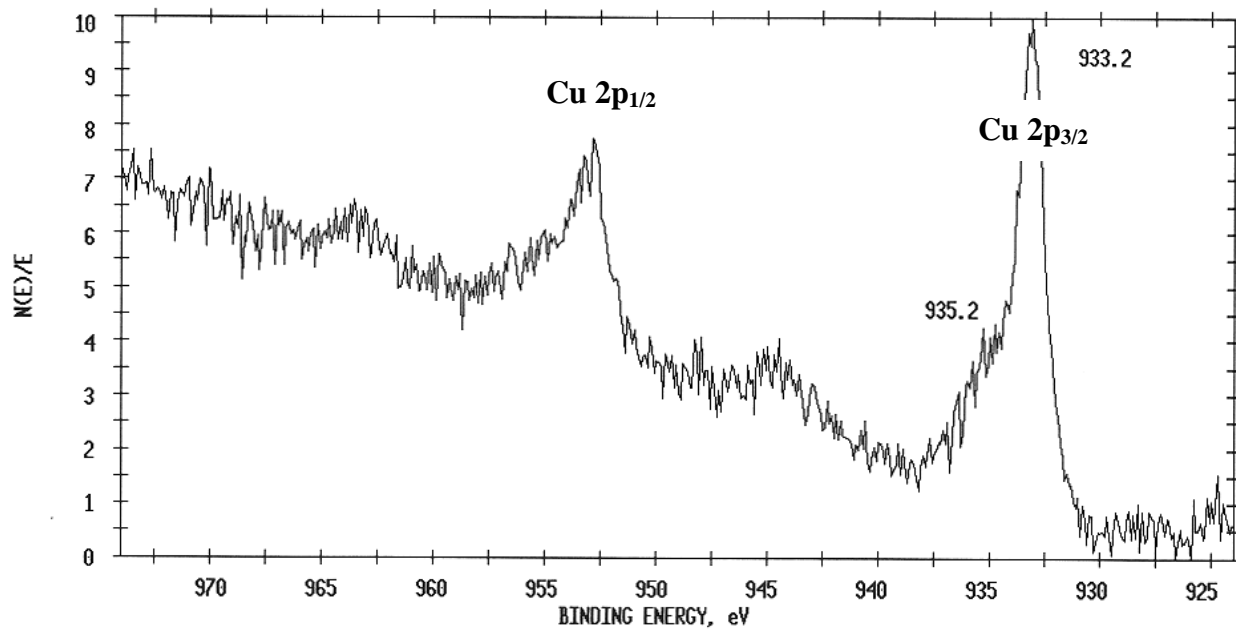


Figure 70: Fiberglass Cu Region MeOH Cleaned (as received) – Cu 2p

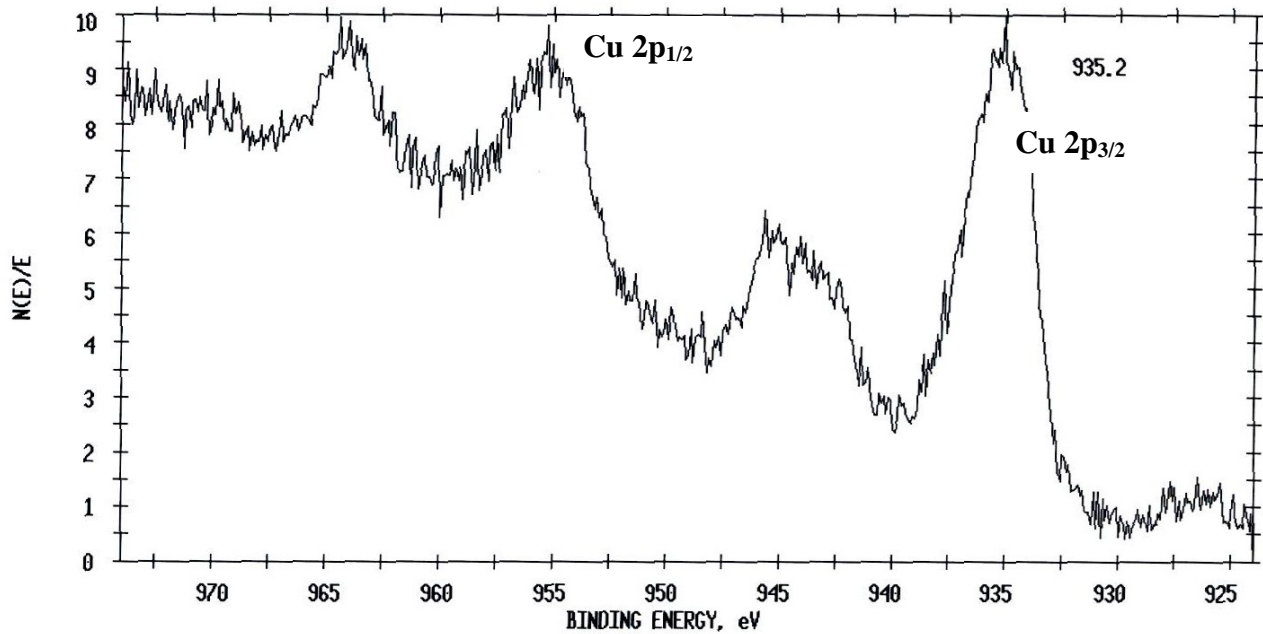


Figure71: Fiberglass Cu Region 100RH & 70°C – Cu 2p

E.4 Quasi-Static Peel Test Results

E.4.1 Introduction

XPS analyses were conducted for quasi-static peel test specimens. A summary of the results (% atomic composition) follows this overview.

Generally, spectra were measured for two different portions of each failure surface. These are designated as cut #1 or cut #2 in the tables. Also two different specimens from the peel tests were measured in some cases, as specified in the following tables. Samples were labeled according to previous peel test sample numbering.

Although zinc is not specifically discussed in the comments following, note that zinc was detected on the Cu failure surfaces, but usually not on the polymer failure surfaces, particularly for the FR4 and Thermount E samples. Zinc was not detected on any of the failed Thermount ST samples.

E.4.2 Results and Discussion

E.4.2.1 FR4 Samples

The following evidence suggests that failure occurs within the composite layer:

- a) No copper is detected on either the copper or the composite failure surface; also the percent compositions for the Cu and polymer failure surfaces are essentially equivalent but are different from the % composition for the non-bonded composite surface.
- b) In accord with the % composition results, the carbon 1s spectra and the O 1s spectra for the Cu and polymer failure surfaces have approximately the same shapes, respectively, and the shapes are unlike the respective shapes of the non-bonded composite surface.
- c) Further, considering the % compositions in the tables, the following trends are seen; relative to the non-bonded composite, the compositions for the Cu and polymer failure surfaces exhibit the following trends; higher carbon, lower oxygen, approximately the same nitrogen, generally higher bromine.
- d) The failure seems to be the same whether the samples were tested at 90, 30 or -15C.

A spectrum for an abraded composite was not measured but should have the composition equivalent to that for the Cu and poly failure surfaces - since failure appears to take place near the surface of the composite layer. An abraded sample should have the composition of the failure surfaces.

E.4.2.2 Thermount ST Samples

The following evidence suggests that failure occurs within the composite layer (similar to the failure process noted for FR4 above):

- a) No copper is detected on either the copper or the composite failure surface; also the percent compositions for the Cu and polymer failure surfaces are pretty much equivalent but are different from the % composition for the non-bonded composite surface.

- b) In accord with the % composition results, the carbon 1s spectra and the O 1s spectra for the Cu and polymer failure surfaces have approximately the same shapes, respectively, and the shapes are unlike the respective shapes of the non-bonded composite surface.

- c) The following trends are evident from the % compositions in the tables; relative to the non-bonded composite, the compositions for the Cu and polymer failure surfaces exhibit the following trends; higher carbon, lower oxygen, higher nitrogen, generally about the same bromine content. Also the nitrogen content is generally higher on the polymer failure surfaces relative to the Cu failure surfaces, whereas the reverse is true for the oxygen content - oxygen higher (generally) on the Cu failure surfaces.

d) There is evidence in the C 1s and O 1s spectra for clearly resolved C-O and C=O contributions to the respective spectra.

e) The failure seems to be the same whether the samples were tested at 90, 30 or -15C.

E.4.2.3 Thermount E Samples

The following evidence suggests that failure occurs within the composite layer:

a) No copper is detected on either the copper or the composite failure surface; also the percent compositions for the Cu and polymer failure surfaces are pretty much equivalent but are different from the % composition for the non-bonded composite surface.

b) In accord with the % composition results, the carbon 1s spectra and the O 1s spectra for the Cu and polymer failure surfaces have approximately the same shapes, respectively, and the shapes are unlike the respective shapes of the non-bonded composite surface.

c) Further, considering the % compositions in the tables, the following trends are evident; relative to the non-bonded composite, the compositions for the Cu and polymer failure surfaces exhibit the following trends; higher carbon, lower oxygen, higher nitrogen, generally equivalent bromine.

d) There is some evidence in the C 1s and O 1s spectra for C-O and C=O contributions to the respective spectra - but the features for these Thermount E samples are not as prominent as in the spectra for the failures for the Thermount ST samples.

e) Silicon was detected on the non-bonded composite but was not detected on either of the failure surfaces (further evidence for failure within the composite).

f) The failure seems to be the same whether the samples were tested at 90, 30 or -15C.

E.4.3 Summary of XPS results for the analysis of Cu-FR4 composite failure surfaces: Peel testing at 90°C, 30°C, and -15°C.

Table 6: XPS results for samples tested at 90°C.

Element/sample	Cu fail #1, cut 1	polymer fail #1, cut 1	non-bond poly surf 1
C	77.1	69.3	69.9
O	16.4	21.4	21.3
N	3.3	3.3	3.4
Cu	<0.2	<0.2	<0.2
Br	3.3	1.2	1.1
Zn	nm	nm	nm
Si	nm	3.0	2.6
Cl	nm	1.8	1.7
Element/sample	Cu fail #1, cut 2	polymer fail #1, cut 2	non-bond poly surf 1'
C	74.1	75.7	68.8
O	19.1	17.4	23.1
N	3.7	3.6	3.7
Cu	<0.2	<0.2	<0.2
Br	3.1	3.3	1.0
Zn	~2 (nm)	nm	nm
Si	nm	<0.2	1.9
Cl	nm	nm	1.4
Element/sample	Cu fail #2, cut 1	polymer fail #2, cut 1	non-bond poly surf 2
C	71.5	75.6	68.2
O	19.8	17.3	22.8
N	4.2	3.8	3.4
Cu	<0.2	<0.2	<0.2
Br	3.1	3.3	1.2
Zn	1.5	nm	nm
Si	nm	nm	3.1
Cl	nm	nm	1.3
Element/sample	Cu fail #2, cut 2	polymer fail #2, cut 2	
C	74.5	77.3	
O	18.0	16.2	
N	3.4	3.4	
Cu	<0.2	<0.2	
Br	2.6	3.1	
Zn	1.5	nm	
Si	nm	nm	
Cl	nm	nm	

Table 7: XPS results for samples tested at 30°C.

Element/sample	Cu fail #3, cut 1	polymer fail #3, cut 1
C	75.1	76.8
O	17.8	15.8
N	3.4	4.2
Cu	<0.2	<0.2
Br	3.1	3.1
Zn	0.6	0.2
Si	nm	nm
Cl	nm	nm

Table 8: XPS results for samples tested at -15°C.

Element/sample	Cu fail #1, cut 1		polymer fail #1, cut 1
	sp1	sp2	
C	76.3	77.7	75.8
O	17.1	15.8	16.4
N	3.2	3.1	3.6
Cu	<0.2	<0.2	<0.2
Br	3.0	3.0	3.1
Zn	0.3	0.4	nm
Si	nm	nm	1.1
Cl	nm	nm	nm
Element/sample	Cu fail #1, cut 2		polymer fail #1, cut 2
C	75.9		76.5
O	17.0		16.6
N	3.4		3.7
Cu	<0.2		<0.2
Br	3.3		3.1
Zn	0.5		0.2
Si	nm		nm
Cl	nm		nm

E.4.4 Summary of XPS results for the analysis of Cu-Thermount ST composite failure surfaces: Peel testing at 90°C, 30°C, and -15°C.

Table 9: XPS results for samples tested at 90°C. Sample #1

Element/sample	Cu fail #1, cut 1	polymer fail #1, cut 1	non-bond poly surf 1
C	76.6	76.7	73.6
O	15.0	14.2	18.7
N	6.7	7.3	3.3
Cu	<0.2	<0.2	<0.2
Br	1.8	1.8	1.4
Zn	<0.2	<0.2	<0.2
Si	nm	nm	1.8
Cl	nm	nm	0.8
Element/sample	Cu fail #1, cut 2	polymer fail #1, cut 2	
C	77.6	78.9	
O	15.8	12.6	
N	4.8	6.7	
Cu	<0.2	<0.2	
Br	1.8	1.8	
Zn	<0.2	<0.2	
Si	nm	nm	
Cl	nm	nm	

Table 10: XPS results for samples tested at 30°C. Sample #1

Element/sample	Cu fail #1, cut 1	polymer fail #1, cut 1	non-bond poly surf 1
C	78.1	76.8	74.2
O	14.8	14.2	19.1
N	4.9	7.2	2.9
Cu	<0.2	<0.2	<0.2
Br	2.2	1.8	1.1
Zn	<0.2	<0.2	0.3
Si	nm	nm	1.3
Cl	nm	nm	1.2
Element/sample	Cu fail #1, cut 2	polymer fail #1, cut 2	
C	77.6	78.9	
O	15.8	12.6	
N	4.8	6.7	
Cu	<0.2	<0.2	
Br	1.8	1.8	
Zn	<0.2	<0.2	
Si	nm	nm	
Cl	nm	nm	

Table 11: XPS results for samples tested at -15°C. Sample #1

Element/sample	Cu fail #1, cut 1	polymer fail #1, cut 1	non-bond poly surf 1
C	77.8	77.2	74.8
O	15.9	15.2	18.0
N	4.2	5.4	3.4
Cu	<0.2	<0.2	0.4
Br	2.1	2.3	1.4
Zn	<0.2	<0.2	0.3
Si	nm	nm	0.6
Cl	nm	nm	1.1

E.4.5 Summary of XPS results for the analysis of Cu-Thermount E composite failure surfaces: Peel testing at 90°C, 30°C, and -15°C.

Table 12: XPS results for samples tested at 90°C. Sample #1

Element/sample	Cu fail #1, cut 1	polymer fail #1, cut 1	non-bond poly surf 1
C	75.5	79.1	71.7
O	18.9	15.0	23.4
N	2.7	4.7	0.7
Cu	<0.2	<0.2	0.2
Br	1.3	1.3	1.3
Zn	1.6	<0.2	<0.2
Si	nm	nm	2.3
Cl	nm	nm	0.4
Element/sample	Cu fail #1, cut 2	polymer fail #1, cut 2	
C	74.9	80.6	
O	19.5	16.2	
N	2.2	1.0	
Cu	<0.2	<0.2	
Br	1.4	2.1	
Zn	2.0	<0.2	
Si	nm	nm	
Cl	nm	nm	

Table 13: XPS results for samples tested at 30°C. Sample #1

Element/sample	Cu fail #1, cut 1	polymer fail #1, cut 1	non-bond poly surf 1
C	78.0	81.5	76.0
O	18.2	14.8	20.0
N	1.6	2.3	<0.2
Cu	<0.2	<0.2	<0.2
Br	1.4	1.4	0.9
Zn	0.8	<0.2	<0.2
Si	nm	nm	2.9
Cl	nm	nm	0.2
Element/sample	Cu fail #1, cut 2	polymer fail #1, cut 2	
C	77.6	78.9	
O	15.8	12.6	
N	4.8	6.7	
Cu	<0.2	<0.2	
Br	1.8	1.8	
Zn	<0.2	<0.2	
Si	nm	nm	
Cl	nm	nm	

Table 14: XPS results for samples tested at -15°C. Sample #1

Element/sample	Cu fail #1, cut 1	polymer fail #1, cut 1	non-bond poly surf 1
C	79.1	79.6	71.4
O	14.9	14.1	23.0
N	4.7	5.4	<0.2
Cu	<0.2	<0.2	0.5
Br	1.1	1.0	1.3
Zn	0.2	<0.2	<0.2
Si	nm	nm	3.8
Cl	nm	nm	<0.2

Table 15: XPS results for non-bonded Cu surface: sample tested at 90°C. Sample #1

Thermount E (Top side of Cu strip from sample #1 of TM-E tested at 90oC).

Element/sample	Cu fail #1, cut 1
C	50.8
O	35.0
N	<0.2
Cu	14.2
Br	<0.2
Zn	<0.2
Si	nm
Cl	nm

E.5 Loop Peel Test Results

XPS analyses for Cu-composite loop peel test samples have been completed. The data summary - atomic % composition for each failure surface is tabulated below. Only one analysis was carried out for each surface and only one specimen (from among several) was analyzed. This should not be a concern since the previous analyses (of quasi-static peel samples) indicated no significant variation for repetitive analyses on the same or on different specimens from the same test and for equivalent failure surfaces.

General comments:

The % compositions are in the ranges:

	FR4	N	E
Carbon	78-80	78-80	78-82
Oxygen	14-15	13-15	14-17
Nitrogen	3-5	3-5	0.5-3
Bromine	2-3	1-3	1-3

Cu not detected at any level above the detection limit ~ 0.2-0.3%

There does seem to be less nitrogen on the E samples compared to FR4 and N, and the amount of bromine on the N and E samples is less than that on FR4.

The carbon and oxygen spectra indicate contributions from C-O and C=O (carbon singly and doubly bonded to oxygen). Generally the spectra for all of the samples - whether for the Cu or

the composite side - are VERY similar. That all are so similar indicates that the failure is the same for all samples - that is failure within the composite material - but leaving a layer of composite on the Cu substrate. Whether the differences in N and Br among the samples is significant, would require measuring/characterizing additional sample failure surfaces.

E.5.1 FR4 Samples

1. No Cu was detected on either the Cu or composite failure surface - findings that indicate failure within the composite. This result is similar to what was found in the analysis for the quasi-static peel test samples. There are some modest differences in the peak shapes for different test conditions, but no inferences are being made in that regard.
2. The spectra and the % compositions for each complementary failure sides are similar and this finding also indicates failure within the composite.

E.5.2 Thermount N and E Series Samples

The results here are similar as for the FR4 specimens.

1. No Cu detected above the detection level.
2. Carbon and oxygen spectra indicate C-O and C=O functionality.

Although SEMs of these failure surfaces were not obtained, they should show evidence of fibers on the Cu AND composite failure surfaces based on the XPS findings. It is surprising that, in general, no silicon was detected, since these composites appear to contain glass fibers. This could indicate that the sizing and polymer adhesion to the fiber is so good that failure at the

fiber-resin interface does not occur. It is true that some Si was detected, but it was not detected consistently nor at a very high concentration.

E.5.3 Summary of XPS results for the analysis of Cu-FR4 composite failure surfaces: Loop testing at 125°C, 25°C, and -30°C.

Table 16: XPS results for samples tested at 125°C, sample #3.

Element/sample	Cu fail	composite fail
C	79.0	78.4
O	14.1	15.1
N	5.3	4.2
Cu	<0.2	<0.2
Br	1.6	2.3

Table 17: XPS results for samples tested at 25°C, sample no number.

Element/sample	Cu fail	composite fail
C	79.5	77.6
O	15.2	15.4
N	2.7	3.2
Cu	<0.2	<0.2
Br	2.6	2.9
Si	<0.2	0.9

Table 18: XPS results for samples tested at -30°C, sample #4.

Element/sample	Cu fail	composite fail
C	78.9	78.5
O	13.9	14.5
N	4.8	4.4
Cu	<0.2	<0.2
Br	2.4	2.6

E.5.4 Summary of XPS results for the analysis of Cu-Thermount N composite failure surfaces: Loop testing at 125°C, 25°C, and -85°C.

Table 19: XPS results for samples tested at 125°C, Sample #4.

Element/sample	Cu fail	composite fail
C	80.2	78.5
O	13.1	14.7
N	4.6	4.8
Cu	<0.2	<0.2
Br	2.1	2.0

Table 20: XPS results for samples tested at 25°C, Sample #1.

Element/sample	Cu fail	composite fail
C	78.9	78.1
O	14.6	14.9
N	3.9	4.4
Cu	<0.2	<0.2
Br	2.6	2.6

Table 21: XPS results for samples tested at - 85°C, Sample #2.

Element/sample	Cu fail	polymer fail
C	77.9	82.2
O	15.8	12.8
N	3.8	3.7
Cu	<0.2	<0.2
Br	2.5	1.3

E.5.5 Summary of XPS results for the analysis of Cu-Thermount E composite failure surfaces: Loop testing at 125°C, 25°C, and -85°C.

Table 22: XPS results for samples tested at 125°C, Sample #3.

Element/sample	Cu fail	composite fail
C	81.2	78.4
O	16.1	16.9
N	0.7	0.9
Cu	<0.2	<0.2
Br	1.6	1.5
Si	0.4	2.3

Table 23: XPS results for samples tested at 25°C, Sample #4.

Element/sample	Cu fail	composite fail
C	81.4	82.4
O	16.3	14.5
N	0.5	1.2
Cu	<0.2	<0.2
Br	1.8	1.9

Table 24: XPS results for samples tested at -85°C, Sample #2.

Element/sample	Cu fail	composite fail
C	81.4	81.1
O	14.6	14.3
N	2.6	3.3
Cu	<0.2	<0.2
Br	1.4	1.3

Author's Vita

Stephen W. Brown received a B.S. degree in Mechanical Engineering from Virginia Tech in 1999. He then worked for Gala Industries, Inc. as a mechanical engineer in the design and manufacture of equipment used to process thermoplastics. Returning to Virginia Tech, he received an M.S. degree from the Department of Engineering Science and Mechanics, with an area of concentration in the mechanics of adhesive bonds and interfaces in 2005. In addition to his research responsibilities during his graduate studies at Tech, Mr. Brown also served as an instructor of undergraduate mechanics. He is a member of the Adhesion Society, the Forest Products Society, and the American Society of Mechanical Engineers, for which he currently serves as Chairman of the Central Pennsylvania Section.